An Analysis of 2D Motional Stark Effect Imaging and Prospects for Determining the Structure of the Magnetic Field Inside a Tokamak.

Mathew J. Creese

**A thesis submitted for the degree of
Bachelor of Science with Honours in Physics of
The Australian National University**

October, 2009

Declaration

This thesis is an account of research undertaken between February 2009 and October 2009 at The Department of Physics, Faculty of Science, The Australian National University, Canberra, Australia.

Except where acknowledged in the customary manner, the material presented in this thesis is, to the best of my knowledge, original and has not been submitted in whole or part for a degree in any university.

Mathew J. Creese
October, 2009

Acknowledgements

I would like to express my gratitude to my supervisor Prof. John Howard for his never wavering help and support throughout this year, but also for giving me the opportunity to travel to the USA and help implement the new imaging diagnostics on the DIII-D tokamak in San Diego. I also wish to extend this thanks to Dr. Ahmed Diallo, for the constant help and useful discussions throughout this thesis.

To the team at DIII-D, thankyou for making the trip possible and so enjoyable. Also to Dr. Boyd Blackwell for providing some of the funding.

I would also like to thank Dr. Matthew Hole for the discussions on the metrics and all others who have in someway contributed to the work presented here.

Finally I would like to acknowledge my fellow Honours students Bill Noble, Rob Evans and Sam Dixon, for the support throughout the year and making the move to the ANU so memorable.

Abstract

A new 2D motional Stark effect imaging system has recently been developed here at the ANU. This instrument has the unique and unprecedented capability to measure the internal magnetic field structure of tokamak and stellarator fusion devices. The key instrumental advance was to devise a means to image the nett polarization state of the complex spectral scene produced by collisionally excited hydrogen isotopes associated with injected high-energy neutral particle heating beams. The major outcome will be a more accurate determination of the structure of plasma embedded magnetic fields and a new capability to address previously inaccessible and outstanding questions relating to tokamak physics, such as magnetic reconnection and current diffusion processes. This thesis explores the extent of these new capabilities which could potentially make a significant contribution on the path to the achievement of controlled fusion and the delivery of an almost inexhaustible "clean" energy source.

As this is a new diagnostic technique, the capabilities of the system are still not well understood. The analysis of the 2D imaging system presented in this thesis is underpinned by the formulation of the key equation linking the quantity measured, the polarization angle of the emission produced by neutral atoms injected into the plasma, to the properties of the plasma magnetic field. This equation enables a determination of the optimum instrument viewing geometry and an assessment of the information that can be reliably extracted. To investigate these issues, a physically meaningful model of the internal magnetic field has been developed which requires a non-orthogonal curvilinear coordinate system representation based on the so-called Miller equilibrium flux surface model. In developing this, it was found that incorrect metric coefficients for this representation have been repeatedly reported in the literature. To analyse the utility of the instrument for the study of plasma magnetic instabilities using synchronous imaging techniques, a perturbation analysis has been undertaken. The results (confirmed by modelling), indicate that it is possible to extract an image of the perturbed vertical poloidal magnetic field component B_Z, which may arise due to internal plasma instabilities. As background to the work, I provide a description of the 2D imaging system and discuss proof-of-principle experimental work which was undertaken at the DIII-D tokamak in San Diego USA.

Contents

Declaration iii

Acknowledgements v

Abstract vii

1 Introduction 1
- 1.1 Fusion and the tokamak . . . 1
  - 1.1.1 Equilibrium . . . 3
  - 1.1.2 Plasma instabilities . . . 5
- 1.2 Motional Stark Effect polarimetry . . . 5
  - 1.2.1 The Standard MSE diagnostic system . . . 7
  - 1.2.2 2D Imaging MSE . . . 9
  - 1.2.3 Why 2D MSE? . . . 9
- 1.3 Contents of this work . . . 9
- 1.4 Context of this work . . . 10

2 2D MSE Imaging Instrument 11
- 2.1 Michelson interferometer . . . 11
- 2.2 Polarization interferometer . . . 13
- 2.3 Savart shearing plate . . . 16
- 2.4 Spectro-polarimeters . . . 18
  - 2.4.1 Double spatial heterodyne spectro-polarimeter . . . 18
  - 2.4.2 Switching spatial heterodyne spectro-polarimeter . . . 19

3 Principles of a 2D MSE System 23
- 3.1 Co-ordinate system used to describe viewing geometry . . . 23
- 3.2 Description of the neutral heating beam . . . 26
- 3.3 Equation describing magnetic pitch angle . . . 27
  - 3.3.1 1D simplification . . . 30
- 3.4 Simplified 2D pitch angle equation . . . 31
  - 3.4.1 Effect of neutral beam divergence . . . 31
  - 3.4.2 Optimum viewing . . . 32
  - 3.4.3 Additional information captured? . . . 34
- 3.5 Magnetic field structure and perturbation analysis . . . 35

4 Miller Flux Surface Representation 37
- 4.1 Curvilinear coordinate transformation . . . 37
  - 4.1.1 Derivatives of the transformation equations . . . 40
- 4.2 Basis vectors . . . 41
  - 4.2.1 Tangent-basis vector . . . 41
  - 4.2.2 Reciprocal-basis vector . . . 43

4.3 Vector representation in a curvilinear coordinate system . . . 43
4.4 The metric coefficients g_{ij} and g^{ij} . . . 44
4.4.1 Metric tensors for the Miller representation . . . 45
4.5 Incorrect metrics reported in literature . . . 46
4.6 Vector relations and differentials . . . 49
4.6.1 The dot and cross-product . . . 49
4.6.2 Differential elements . . . 49
4.6.3 Operations involving ∇ . . . 49

5 Modelling of MSE polarization images 51
5.1 A representation for the poloidal magnetic field . . . 51
5.1.1 Model for the poloidal flux function ψ . . . 53
5.1.2 Equilibrium and Shafranov shift . . . 54
5.1.3 TEXTOR model poloidal magnetic fields . . . 56
5.2 Model MSE polarization pitch angle map . . . 59
5.3 Line of sight integration effects . . . 60
5.4 Modelling MSE images with MHD instability . . . 64
5.4.1 Technical feasibility of determining the perturbed magnetic field . . 70
5.4.2 Linking $\tilde{B}_Z$ to $\tilde{\psi}$ . . . 72

6 Experimental Data 75
6.1 DIII-D (USA) . . . 75
6.1.1 Double heterodyne system . . . 77
6.1.2 Switching heterodyne system . . . 79

7 Outcomes and Recommendations 85

8 Appendices 87
Appendix A: Relationship between the poloidal flux function ψ and the vector potential A in the Miller representation . . . 87
Appendix B: Determining B_R and B_Z from Miller magnetic field components B^r and B^θ . . . 89
Appendix C: Form of ψ for large aspect ratio plasma with parabolic current density 90
Appendix D: Toroidal current density . . . 91

List of Figures

1.1 Schematic of a tokamak illustrating the major components. 2
1.2 Poloidal cross section of the DIII-D showing the nested magnetic surfaces, overlaid is an experimental image of the emission from the 30L neutral beam 4
1.3 Doppler Stark shifted spectrum 6
1.4 Setup of the MSE diagnostics on the DIII-D tokamak. 8

2.1 Schematic of a Michelson interferometer 12
2.2 A model interferogram produced by a Michelson interferometer. 13
2.3 Schematic of a polarization interferometer. 14
2.4 Ideal MSE component and the interferometric contrast of the total and individual components 15
2.5 A ray diagram showing the paths of an extra-ordinary (E) and ordinary (O) ray through a Savart shearing plate. 16
2.6 Schematic of the polarization interferometer with a Savart shearing plate inserted between the wave-plate and polarizer which is illuminated by linearly polarized light. 17
2.7 Optical arrangement of the double spatial heterodyne spectro-polarimeter. . 19
2.8 Images of a magnetized zinc lamp at 468 nm with the double spatial heterodyne spectro-polarimeter illustrating the resultant 2D fringe pattern. . . 20
2.9 Optical arrangement of the switching spatial heterodyne spectro-polarimeter. 20
2.10 Two calibration images for the switching spatial heterodyne spectro-polarimeter, illustrating the change in the observed fringe pattern between the two states of the FLC. 21

3.1 Schematic of a section of a tokamak which illustrates the natural cylindrical coordinate system used to describe a position within the tokamak. 24
3.2 Schematic of the general viewing geometry of an MSE system and neutral heating beam within a tokamak. 25
3.3 Figure illustrating the decomposition of the velocity vector of a divergent beam. 28
3.4 3D schematic of a neutral beam sheet and a sightline of the imaging system. 29
3.5 Schematics of the viewing geometries which reduce the form of the pitch angle equation. 32
3.6 Schematics of the viewing geometries which minimises the effect of the toroidal magnetic field B_ϕ on the pitch angle equation. 34

4.1 Representation of a "D" shaped magnetic flux surface of a tokamak. 38
4.2 Poloidal cross section plots illustrating the effect of the Miller shape parameters; elongation κ, triangularity δ and Shafranov shift $R_0(r)$ on the shape of poloidal magnetic flux surfaces. 39

4.3 Coordinate curves for r and θ for an equilibrium with $\kappa = 1.4$, $\delta = 0.4$, no Shafranov shift and with no variation of the flux surface parameters between surfaces. 40
4.4 An enlarged section of Fig. 4.3 (indicated by the dotted box) which shows the basis vectors at two point of intersection for the Miller curvilinear coordinate system. 42
4.5 Comparisons of the metric coefficients h_r as stated by Stacey (red), given by $1/|\nabla r|$, and that as calculated from first principles (blue), $\sqrt{g_{rr}}$, as a function of θ. 47
4.6 Comparison of the metric coefficient h_θ as stated by Stacey (red), Eq. 4.44, and that as calculated from first principles (blue), $\sqrt{g_{rr}}$, as a function of θ. 48

5.1 Plots of ψ and calculated j^ϕ showing the effect of the Shafranov shift. . . . 55
5.2 Poloidal cross sections of the poloidal flux function ψ with parameters ($\alpha = 2, c = 2.16, s = 0.038$), B_R and B_Z as well as the calculated current density j^ϕ. 57
5.3 Poloidal cross sections of the poloidal flux function ψ with parameters ($\alpha = 3, c = 1.8, s = 0.037$), B_R and B_Z as well as the calculated current density j^ϕ. 58
5.4 Flowchart of method used to determine the pitch angle map 59
5.5 Calculated pitch angle map for the centre sheet of the neutral beam on TEXTOR. 60
5.6 Calculated pitch angle map for the centre sheet of the neutral beam on TEXTOR for an ideal non-divergent neutral beam ($\xi = 0$). 61
5.7 Schematic of the viewing geometry of TEXTOR, showing the pitch angle maps for the neutral beam split into 4 equally spaced sheets. 62
5.8 Model pitch angle map with line of sight integration effects accounted for and the difference with the ideal central sheet pitch angle map. 63
5.9 Pitch angle maps showing that for the view at TEXTOR the approximate pitch angle equation is valid. 64
5.10 Plot of the influence function $f(r)$ used for the perturbation of ψ, also overlaid is the safety-factor used to find $f(r)$. 66
5.11 Figure showing the perturbed poloidal flux function ψ and the perturbed poloidal magnetic field components calculated from ψ. 67
5.12 Pitch angle map for the centre neutral beam sheet calculated from a perturbed poloidal flux function. 68
5.13 Difference between the pitch angle maps for the perturbed poloidal flux function as calculated with the full and approximate pitch angle equation. . 69
5.14 Extracted perturbed vertical magnetic field component $\tilde{B}_Z$. 70
5.15 Extracted perturbed vertical magnetic field component $\tilde{B}_Z$ calculated with line integrations effects. 71

6.1 Geometry of the neutral heating beam injection system for DIID-D 76
6.2 Pictures of the double spatial heterodyne system deployed on the DIII-D tokamak. 76
6.3 Modelled spectrum and nett fringe contrast of the complete Stark multiplets of the 30L neutral beam as viewed from the 90^o port. 78
6.4 Raw calibration images for the double spatial heterodyne spectro-polarimeter illuminated by a polarized source. 78

6.5 Raw images of shot 138353 captured with the double spatial heterodyne spectro-polarimeter illustrating the heating grill in the background of the view from the 90^o port on DIII-D. 79
6.6 Modelled spectrum and nett fringe contrast of the complete Stark multiplets of the 30L neutral beam as viewed from the 120^o port. 80
6.7 Raw images and line segment illustrating the difference in fringe visibility between the calibration images and plasma shots on DIII-D. 81
6.8 A raw calibration image for the switching system, an image of the demodulated phase difference between successive frames and a calibration curve is shown. 82

Chapter 1

Introduction

Motional Stark effect (MSE) polarimetry currently provides the only reliable and routine measurement of the internal magnetic field in a tokamak. This is vital internal information needed for the reconstruction of the underlying magnetic flux function which describes the equilibrium and stability properties of the confined plasma. However, due to technical limitations, MSE polarimetry is restricted to measurements in the range of 10's of discrete observing positions within the tokamak. Recent important developments in advanced spectroscopic techniques, pioneered at the ANU, will allow for the first time, 2D imaging of the internal magnetic field of tokamak fusion devices [1]. The extension to 2D has the natural capability to directly image internal magnetic structures within a tokamak, which, if successful, will provide much needed information on magnetohydrodynamic (MHD) instabilities which can potentially inhibit production of nett power from fusion devices.

Given these new capabilities the key focus of this thesis is to explore the nature of the information that can be obtained from such 2D internal magnetic measurements. Is this an important innovation and if so, to what extent can the results be depended upon to deliver new physics?

1.1 Fusion and the tokamak

One of the defining problems that the world faces is how our ever increasing energy demand will be met in the future in a responsible and practical manner. Energy produced through nuclear fusion reactions is one potential solution. In the fusion process, nuclei of light elements, such as isotopes of hydrogen, combine and release energy due to the lower rest mass of the resultant nucleus.

There are a number of possible fusion reactions, but due to the relatively low fusion cross section and high energy yield the most promising for a terrestrial reactor is the deuterium-tritium reaction:

$$^2_1\mathrm{D} + {}^3_1\mathrm{T} \rightarrow {}^4_2\mathrm{He} + {}^1_0\mathrm{n} + 17.6\ \mathrm{MeV}.$$

The 17.6 MeV of kinetic energy released in this reaction is shared between the helium nucleus (3.5 MeV) and the neutron (14.1 MeV), where the energy of the neutron can be harvested.

In order for these two species to fuse they must overcome the Coulomb force which repels the two positively charged nuclei as they approach one another. The most convenient way for the reaction to be induced is through heating the fuel such that for a significant fraction of the populations the thermal energies are enough to overcome the Coulomb potential barrier. A fusion reaction will ignite for deuterium and tritium at temperatures of the order 10 keV [2]. As the species possess Maxwellian velocity distributions, this

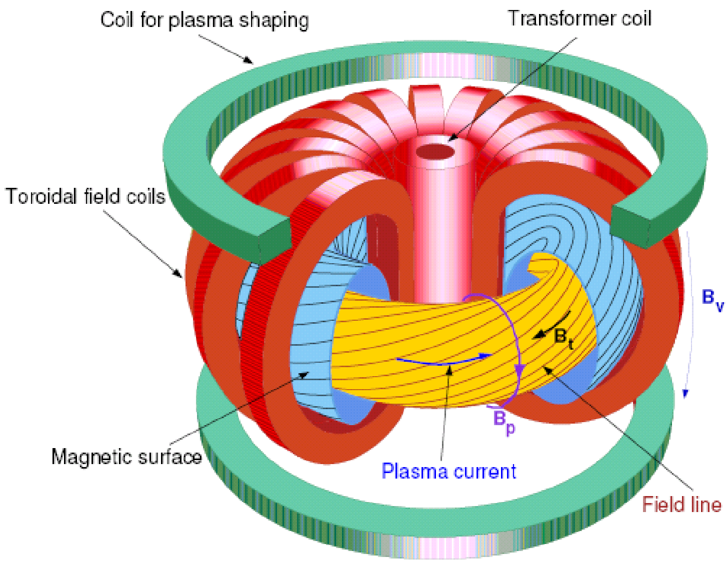

Figure 1.1: Schematic of a tokamak illustrating the major components *(Image taken from http://www.bmbf.de/en/2270.php)*.

energy does not correspond to the maximum of the reaction cross section at 100 keV, as the reaction can be sustained by the species in the high energy tails of the distributions.

At the high energies required for fusion, the fuel is completely ionized to form a plasma. In the presence of a magnetic field the electrons and ions gyrate in helical paths around the magnetic field lines through the Lorentz force, $\mathbf{F} = q\mathbf{v} \times \mathbf{B}$. This is the basis of magnetic confinement devices, where an appropriate configuration of the field lines produce a *magnetic bottle* which confines the high energy particles in a manner that is conducive to the production of fusion reactions. The leading magnetic fusion device is the tokamak, which is a toroidal magnetic confinement device first invented in the Soviet Union in the 1950's. A comprehensive description can be found in Wesson [2].

The principal magnetic field of the tokamak is the toroidal field component, produced by current carrying toroidal field coils which are arranged in a manner that resembles a solenoid closed upon itself (a torus). The geometry of the tokamak is best described in a cylindrical coordinate system (R, Z, ϕ), where the central axis of the torus is aligned with Z and the toroidal direction is given by $\hat{\phi}$.

This toroidal magnetic field alone is not sufficient to confine a plasma, as it has a 1/R dependence due to its topology. This inhomogeneity causes a vertical separation of the ions and electrons of the plasma which then causes both species to drift outwards, destroying confinement. However, when the magnetic field lines have a helical nature, this outward drift is effectively short circuited, restoring confinement. Since for each rotation of the field lines, the species spend part of their time drifting away from the plasma centre and part drifting towards the centre.

A large toroidal plasma current is induced in the plasma, by transformer action with a central transformer coil, to produce the poloidal magnetic field necessary for overall helical magnetic field lines. This toroidal plasma current characterises the tokamak from other toroidal magnetic fusion devices, such as the stellerator where the helical field lines are produced completely by external current carrying coils. Due to the toroidal symmetry of the tokamak, these helical magnetic field lines produce an infinite set of nested magnetic surfaces. In general these nested magnetic surfaces are characterized and can be labelled by their enclosed poloidal magnetic flux ψ [3]. In order to control the position and shape of the magnetic flux surfaces of the plasma, shaping coils are used. Figure 1.1 is a schematic of this general setup for a tokamak, illustrating all these main features.

Each magnetic surface has a winding number q which describes the average helicity of the magnetic fields on that surface. This value q is defined as the number of toroidal rotations (n) needed for the field line to complete one poloidal circuit (m=1). This value can be either rational or irrational, where for an irrational value the magnetic field line never closes upon itself but traverses every point of the surface. As the general motion of the plasma particles will be constrained to these flux surfaces, MHD instabilities can form and grow only on surfaces with rational winding number ($q = m/n$), with lower values tending to be least stable. The risk of a plasma instability reduces with increasing values of q which is why this winding number is called the safety-factor. For conventional tokamak scenarios, $q \approx 1$ in the core and usually rises monotonically to values of 2-6 at the edge. The profile of the safety factor is also important for stability, as it high magnetic shear between surfaces for certain configurations can suppress fluctuations and dramatically improve confinement [4]. The safety factor and its profile are determined by the plasma current density profile and flux surface geometry.

An important by-product of the induced toroidal current is that the plasma is also resistively heated. The ohmic heating is produced by electron-electron collisions. However, at higher particle velocities, Coulomb collisions effectively scatter the particles and the resistivity of the plasma decreases with increasing electron temperature ($R \propto T_e^{-3/2}$) [5], allowing the plasma to be heated only to temperatures < 1 keV. For fusion temperatures to be reached, the plasma must be further heated through two additional processes. The first is achieved by launching electromagnetic waves into the plasma which resonate with the natural frequencies of the plasma particles, allowing the energy of the waves to be absorbed by the particles. The second is through neutral beam injection (NBI), where high energy neutral atoms are injected toroidally into the plasma. Collisions between these high energy atoms and the plasma particles ionize the neutral beam, thereby imparting momentum and energy to the plasma. An important fringe benefit of this heating technique is that the neutral beam emits optical radiation that can be used for important internal diagnostic measurements. One of the primary diagnostics which exploits this emission is motional Stark effect polarimetry, which is the primary topic of this thesis and an in-depth introduction will be given in section 1.2.

Typical toroidal currents that are produced in the leading tokamak designs are in the order of millions of amps. This is an enormous reservoir of free energy and if not controlled properly can drive the MHD instabilities resulting in reduced plasma confinement and in worst case scenarios loss of confinement, which can potentially cause damage to the machine. Accurate control of the plasma current density is thus crucial to the realisation of controlled nuclear fusion. Notwithstanding this, the current density inside a tokamak is still relatively poorly diagnosed and its control is the subject of intense research activity.

1.1.1 Equilibrium

The magnetic field configuration chosen for confinement must be in equilibrium with the plasma it contains[3]. The plasma pressure, the product of the particle density and temperature, exerts an outward force and the poloidal magnetic field exerts an inward force, with the imbalance taken up by the magnetic pressure of the toroidal magnetic field [5]. Equilibrium is reached when the Lorrentz force of the magnetic field is balanced by the plasma pressure gradient force everywhere:

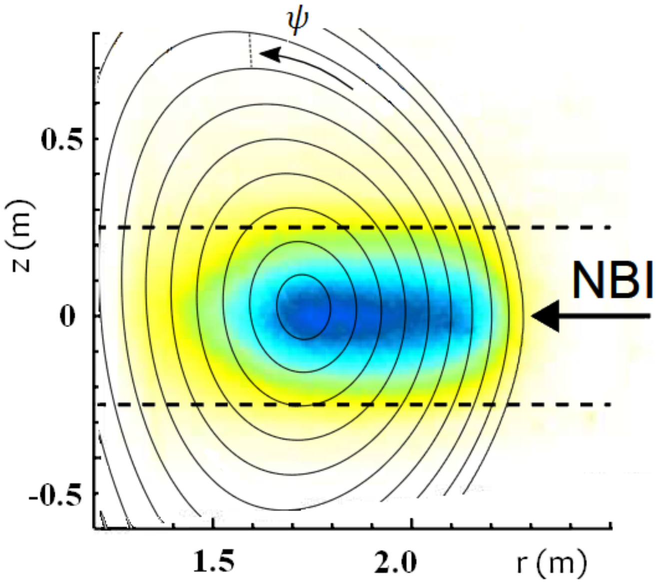

Figure 1.2: Image showing unprocessed H_α emission of the 30L neutral beam on he DIII-D tokamak into a plasma with an electron density of 1.1 x 10^19 m^{-3} as viewed from the 120^o port (not shown in Fig. 1.4), where dark blue indicates highest intensity of emission. The estimated contours of the poloidal flux function have been overlaid *(Courtesy of M. van Zeeland)*.

$$\nabla p = \mathbf{j} \times \mathbf{B}, \tag{1.1}$$

It is seen from this equation that $\mathbf{B} \cdot \nabla p = 0$, so that the magnetic surfaces are isobaric. Furthermore, $\mathbf{j} \cdot \nabla p = 0$ and consequently the current lines also lie on the magnetic surfaces.

The equilibrium equation, Eq. 1.1, for a toroidally symmetric plasma within a tokamak can be written as a scalar differential equation (called the Grad-Shafranov equation) in terms of the poloidal flux function ψ:

$$R\frac{\partial}{\partial R}\frac{1}{R}\frac{\partial \psi}{\partial R} + \frac{\partial^2 \psi}{\partial Z^2} = -\mu_0 R^2 p'(\psi) - \mu_0^2 f(\psi) f'(\psi), \tag{1.2}$$

where R, Z are cylindrical coordinates, $p(\psi)$ is the plasma pressure, $f(\psi)$ is the toroidal magnetic flux function and the primes represent the derivatives with respect to ψ. This non-linear partial differential equation governs the spatial distribution of the poloidal flux function ψ, which determines, and is determined by, the poloidal magnetic field, current and pressure profiles.

Today the Grad-Shafranov equation is routinely solved numerically to provide an estimate of the spatial distribution of the poloidal magnetic flux function for plasma discharges in a tokamak [6]. This so-called equilibrium reconstruction, involves prescribing physically reasonable functions $p(\psi)$ and $f(\psi)$ then iteratively solving Eq. 1.2 subject to appropriate boundary conditions, provided by external magnetic flux loop and pickup coil measurements, and internal magnetic constraints, provided by MSE polarimetry. As external magnetic measurements are not sufficient to accurately reconstruct the equilibrium [7], internal magnetic measurements are crucial, but are currently limited to only providing a tens of data points.

Figure1.2 shows a portion of a poloidal cross section of the DIII-D tokamak with the experimentally determined nested magnetic surfaces, upon which is superimposed an experimental image of the radiation emitted from a neutral heating beam.

1.1.2 Plasma instabilities

Because of the long range nature of the Coulomb force tokamak plasmas are predicted and observed to suffer from a wide variety of instabilities. Low frequency instabilities can be described by the single-fluid magneto-hydro-dynamic (MHD) model of plasmas. The global stability limits for MHD instabilities are well known and constrain the normal operating regimes of a tokamak. These large scale instabilities can result in a complete loss of plasma confinement. Even when plasmas are produced which are safely within the global MHD stability limits, a number of macroscopic MHD instability are commonly observed, which can degrade the performance of a tokamak.

A prominent macroscopic instability in all tokamaks is the so called sawtooth collapse. This instability manifests itself as a regular periodic reorginisation of the plasma core and does not result in a catastrophic loss of confinement. The core plasma quickly recovers and the instability repeatedly occurs in a regular manner [8].

A defining feature of a sawtooth cycle is a precursor phase in which an MHD internal kink instability grows [8]. This kink mode perturbs the core magnetic surfaces with a poloidal mode number $m = 1$ and toroidal mode number of $n = 1$, resulting in a helical displacement of the plasma core. Following this precursor phase a trigger, which is still not understood, causes a rapid reorganisation of the internal magnetic flux (i.e. the current distribution) leading to cooling and particle loss within the core plasma.

A number of mechanisms explaining the sawtooth instabilities have been proposed over the years [9][10][11]. A unified theory has yet to be established which accounts for all the experimental observations of the sawtooth instability. Much of this can be attributed to the fact that no direct measurement of the internal structure of the perturbed magnetic field has been available throughout or at different stages of the sawtooth cycle.

In this thesis, I will consider the capabilities of the new 2D imaging diagnostic to provide useful direct measurements of the perturbed magnetic field structure through the evolution of the sawtooth cycle.

1.2 Motional Stark Effect polarimetry

Motional Stark effect (MSE) polarimetry of Stark split emission from injected neutral heating beams has become the standard technique for measuring the internal magnetic field pitch angle used for constraining equilibrium reconstruction[12].

The principle of the measurement relies on the Stark effect[13] splitting of the atomic energy levels of injected neutral hydrogen and deuterium atoms in the plasma. This arises as the high velocity of the atoms across the magnetic field of the plasma induces a strong Lorentz electric field in the rest frame of the atom, $\mathbf{E} = \mathbf{v} \times \mathbf{B}$. As these injected atoms traverse the plasma, spectral line emission will occur due to collisional excitations with background plasma ions and electrons. A typical Stark split Balmer-α emission spectrum is shown in Fig. 1.2. The induced electric field causes splitting of the spectral lines of the atom, giving rise to linearly polarized emission. For complex atoms, when a weak field is applied the splitting is quadratic in the magnetic field strength, becoming linear for strong fields. However for hydrogen like atoms the splitting is linear for weak fields due to the degeneracy of states with different angular momentum quantum numbers l with fixed n.

When the emission is viewed perpendicular to the electric field the $\Delta m = 0$ transitions, π components, are linearly polarized parallel to the electric field and the $\Delta m = \pm 1$ transitions, σ components, are linearly polarized perpendicular to the electric field, or, in our case, parallel to the magnetic field. When viewed parallel to the electric field the

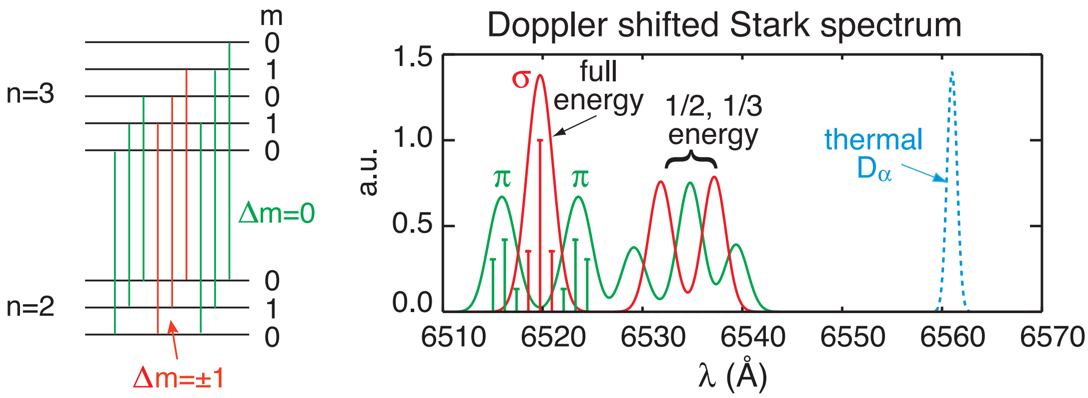

Figure 1.3: A typical doppler shifted Stark spectrum for an injected deuterium atom. The Balmer$-\alpha$ transitions are shown and the relative intensities of the individual components. The overall line shape for the σ and π components are shown, with the three populations present within the neutral beam indicated; the main full energy and the minor half and third energy components. To illustrate the extent of the Doppler shift for a typical view, the thermal background radiation is shown. (*Courtesy of the DIII-D program and General Atomics.*)

π components have no brightness and the σ components become unpolarized. Figure 1.3 shows the splitting of the energy levels for the Balmer-α transition and the relative brightness of the individual σ and π components. By measuring the polarization of the components of the Stark multiplet the orientation of the internal magnetic field, which is dependent on the strengths of the internal magnetic components, can be found.

Typical neutral heating beams toroidally inject hydrogen or deuterium at energies of 50 to 80 keV, These energies are sufficient to produce a significant Stark shift which dominates over the Zeeman effect. Due to charge exchange, electron impact and ion impact ionization the neutral beam is attenuated, see Fig. 1.2. This attenuation is dependent on the density of the plasma and the beam energy but for typical operating parameters the attenuation length is in the order of 1 m.

The spectral line which is generally utilized is the Balmer-alpha (H_α) transition (n=3 $\rightarrow$ n=2) at 656.3 nm. For this transition the separation of adjacent components of the multiplet vary as $\Delta\lambda_S = 2.7574 \text{ x } 10^{-8}$ E nm where E = $|\ \mathbf{v} \times \mathbf{B}\ |$. Due to the large velocity of the beam (v $\approx$ c/100) the multiplet is conveniently Doppler shifted from background radiation. The amount is dependent on the angle between the sight line and the beam and for typical viewing geometries the shift of the full energy component is approximately 4 nm towards the red, as can be seen in Fig. 1.3.

Within the neutral beam housing an ion source produces predominately H^+ or D^+ ions but there are also significant proportions of H_2^+, D_2^+ and H_3^+, D_3^+. These ions are then accelerated an by electrostatic particle accelerator before being neutralized prior to entering the plasma. As the mass of these other components is double and triple that of H or D, the velocity of each will be reduced by a factor of $\sqrt{2}$ and $\sqrt{3}$ respectively. The Doppler shifted emission of these components will be observed at 1/2 and 1/3 of the nominal beam energy, which gives rise to the name of the emission produced by these populations: the half and third energy components. Also due to the lower velocities of these components a smaller Stark shift is observed, with less separation of the σ and π components, blurring the overall MSE multiplet. The half and third energy components of the emission from the neutral beam are illustrated in Fig. 1.3. Because of the blurring, these components are usually avoided in standard MSE systems.

1.2.1 The Standard MSE diagnostic system

MSE polarimetry was first developed and implemented on a toroidal fusion device in 1989 by Levinton *et al* [14]. The purpose of this system was to obtain a radial profile of the magnetic field pitch angle to determine the safety factor at the magnetic axis $q(0)$.

The instrument determines the magnetic field pitch angle by isolating the central σ component of the multiplet and measuring the polarization direction. The observation is made at points along the mid plane of the tokamak and only gives a single point measurement where the sight line of the instrument intersects the neutral heating beam. In the first measurements a radial profile of the magnetic field pitch angle was created by a shot-to-shot scan where the injection angle of the neutral beam was altered to change to radial intersection of the sightline and the beam. The safety factor q at the magnetic axis is then able to be estimated from the radial profile of the magnetic pitch angle.

The instrument uses a tunable narrow band interference filter, typically having a spectral width of 0.4 nm, centred on the central σ component of the multiplet. Once isolated, the polarization angle of the component is then obtained by a modulated polarimeter which consists of two photoelastic modulators (PEM) mutually oriented at 22.5^o and followed by a linear polarizer.

The PEMs act as waveplates with the delay oscillating between approximately $-\lambda_0/2$ and $\lambda_0/2$, where λ_0 is the central wavelength. The modulating delay is produced by resonant piezo-activated birefringence of a quartz plate. Driving the PEMs at two different frequencies causes the direction of the linearly polarized input wave to be modulated at frequencies ω_1 and ω_2. The magnitude of this modulation is dependent on the direction of the input polarization with respect to the waveplate axis. The linear polarizer then converts this polarization modulation into an amplitude modulation, with the ratio of the signal amplitudes at the two PEM frequencies delivering the tangent of twice the magnetic pitch angle [14].

Due to the high polarization fraction needed for this measurement and the fact that the Stark multiplet is nett unpolarized when there is no spectral discrimination, the instrument can only be installed on high field plasma devices with toroidal fields at the magnetic axis > 1 T. For lower magnetic fields the separation of the σ and π components becomes comparable to the line widths of the components and the multiplet is poorly resolved.

Due to the good spatial resolution and low statistical uncertainty in the pitch angle obtained with this instrument[15] it has become the standard method for determining the field strength of the poloidal magnetic field within toroidal fusion devices. Since its first conception and implementation, the basic MSE polarimetry module has changed very little.

The next stage in the evolution of MSE polarimetry was to implement multiple fixed spatial channels in order to produce simultaneous radial profile determination of the magnetic pitch angle. To illustrate, a description of the evolution of the MSE systems for the DIII-D tokamak, located at General Atomics in San Diego, USA, is given.

In 1992 8 spatial channels were implemented [16], followed up two years later when a second array was brought online, bringing the total number of channels from 8 to 16 [17]. This second array adopted a different viewing geometry, resulting in increased spatial resolution near the outer region of the plasma. The latest upgrade on DIII-D was completed in 2007. There are now 5 different arrays, 3 viewing the core and 2 radial arrays, with a combined total of 64 individual MSE polarimetry channels [18]. The setup of 3 of these arrays viewing the 30L neutral beam on DIII-D is shown in Fig. 1.4. The other 2 arrays are now shown here as they view the 210R neutral beam. With such arrays of instru-

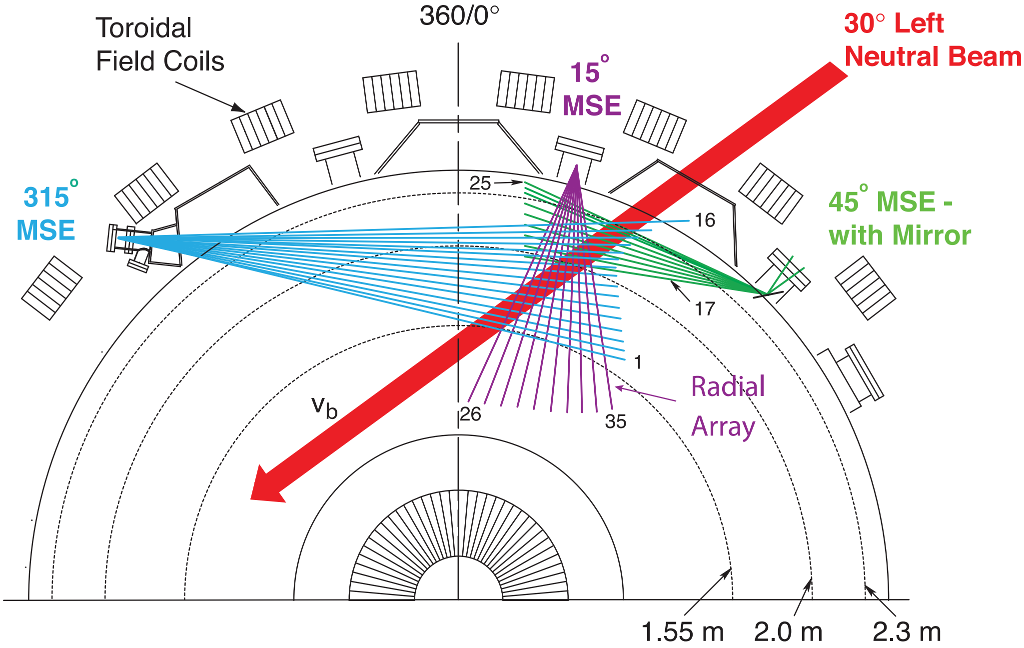

Figure 1.4: Setup of the MSE diagnostics on the DIII-D tokamak. The 30L neutral heating beam is shown with 3 of the MSE arrays. Each array has the sightlines of individual instruments shown, 36 spatial channels in total (*Courtesy of the DIII-D program and General Atomics.*)

ments, allowing direct measurements of the internal magnetic fields, MSE has become a vital diagnostic technique for the use in constraining the equilibrium reconstruction.

This standard MSE technique suffers from the following limitations:

(i) Due to the variation of Doppler shift with viewing angle, the spectral shift of the central σ component of the Stark multiplet varies across the spatial channels. This has precluded the use of imaging techniques as dedicated narrow band filters are required to isolate the central σ component at each channel. Meaning many expensive narrow band filters each of which must each be optimized for their respective viewing positions. This restriction also means that the beam energies cannot be changed and requires tuning in order to match the filter passbands.

(ii) A complicated calibration procedure is necessary to insure meaningful interpretation of the data captured [16].

(iii) Each spatial channel is a unique 1D instrument. So the cost of an array of channels is high and so only a coarse sampling of the radial profile of the internal magnetic field is obtained.

(v) It is difficult to observe instabilities due to instrumental limitations.

Currently under development by E. Foley [19] is a new technique that extends the capabilities of the conventional MSE diagnostics, enabling the magnetic pitch angle to be determined in low field toroidal devices (> 1 T). This technique uses laser induced fluorescence (LIF) which will allow both magnetic field orientation plus field strength to be determined along the intersection of the laser and neutral diagnostic beam.

An alternative to polarimetry to determine the pitch angle is to use the ratio of the intensities of orthogonal Stark split components. Such a system, named B-Stark, has been implemented on DIII-D as well as on other devices,including TEXTOR [20]. This approach has the advantage that it is not sensitive to the polarization of the emission as it relies on the relative intensities of the two components used.

1.2.2 2D Imaging MSE

A radical new spectro-polarimetric technique, developed here at the ANU, has enabled both the spectral and polarization information of the entire Stark multiplet to be encoded in a single snapshot of the Stark emission [1]. This is achieved using a spectro-polarimeter which encodes the spectral and polarization information of the Stark multiplet on orthogonal spatial interference fringe patterns. Processing the captured image then produces a 2D image of the magnetic field pitch angle with the spatial resolution fixed by the fringe pattern spatial frequency. The new system, which is equivalent to thousands of conventional MSE instruments, is constructed from simple polarization optics and an imaging camera resulting in a compact instrument well suited to the limited space often encountered on the complex tokamak machines. This new imaging system is discussed in detail in Chapter 3.

1.2.3 Why 2D MSE?

As stated previously, to accurately reconstruct the plasma equilibrium, internal magnetic measurements are crucial, as external measurements are not sufficient to accurately determine the internal magnetic structure [7]. If the poloidal magnetic field can be directly measured with higher resolution in the core region of the plasma, the accuracy of the numerical solution for ψ, and many other important properties dependent of ψ, could be greatly increased. Ultimately better knowledge of ψ will aid in the understanding of the underlying physics at play within tokamaks.

As an example, the understanding of instabilities, which can limit the performance of fusion devices, has improved greatly but nevertheless is still incomplete. The underlying structure of the perturbations to the internal magnetic field associated with instabilities, such as sawteeth, is still not known or understood, mainly due to the inadequacies of existing diagnostics. Information about the internal structure of the magnetic field is one of the key pieces of information which is needed in order to understand the physics of these instabilities and so allow development of appropriate suppression strategies. A successful 2D MSE imaging system will have the necessary capabilities to provide such measurements.

As the 2D MSE imaging system considered in this thesis has only recently been developed, its full capabilities and limitations are not well known. The work presented in this thesis analyses the capabilities of the new technique to capture information on the internal magnetic field structure and more importantly, assess usefulness of this information.

1.3 Contents of this work

In chapter 2 the basic principles of the new imaging instrument are given with the intent of understanding the fundamental components of the instrument, which are a simple polarization interferometer and Savart shearing plates. The two spectro-polarimeter instruments, each being variation of the other, are then briefly discussed.

In chapter 3 the geometry of a general 2D MSE system is described, with a derivation of the equation which describes the pitch angle for a general view of a neutral heating beam.

Properties of this basic equation are then explored, leading to a discussion on the optimum viewing position of the instrument to capture useful information of the poloidal magnetic field, leading to a consideration of the additional information a 2D system captures over the conventional discrete channel 1D MSE systems. With the understanding that a 2D system can inherently capture information on magnetic field structures within a tokamak, a method for extracting magnetic perturbations associated with instabilities using imaging techniques is given.

The Miller flux surface representation, a non-orthogonal curvilinear coordinate system, which is needed for modelling of the internal magnetic fields of a tokamak is then discussed in chapter 4. As a tensor analysis must be adopted for such a system an overview of non-orthogonal curvilinear coordinate systems is presented. This leads to a discussion on incorrect material on the the metric tensor coefficients for this coordinate system which has been discovered in the literature[1]. The required differential and vector operations needed for later modelling are then stated.

Modelling of 2D MSE pitch angle images, for static equilibrium but more importantly for an idealistic instability of the plasma is then undertaken in chapter 5. In order to achieve this much time has been spent on developing an accurate analytic model for the poloidal magnetic field within a tokamak, which conforms to the equilibrium condition as well as taking into account the toroidal bending of the underlying current density. With this method and the framework developed in chapter 4, the important line of sight integration effects are then modelled and discussed. A heuristic model for an idealistic perturbation which resembles the kink mode, the underlying magnetic perturbation of the observed sawtooth instability, is then developed and applied to assess the validity of the method to extract an image of the underlying magnetic perturbation. A discussion on the inferred image of the magnetic perturbation then follows.

As part of this thesis, experimental work was carried out in the form of helping implement the spectro-polarimeters on the DIII-D tokamak, located in San Diego USA. The experimental program and setup of the instrument is given in chapter 6, followed by a discussion on the data captured and the preliminary results. Previous data taken on the TEXTOR tokamak (Germany) is also discussed briefly with comparisons of the measured phase of the velocity profile of the neutral beam and the analytic predicted based on the model developed in chapter 3.

Finally the conclusion and future directions of this work is then given in chapter 7.

1.4 Context of this work

After encouraging first results obtained with the 2D MSE imaging system on the TEXTOR tokamak, the original intention of this work was to implement the 2D system on the DIII-D tokamak and analyse the captured data. However, due to the lack of successful data obtained at DIII-D, a readjustment of the focus of the work to be undertaken was made. This resulted in the aim of this thesis to better understand the imaging systems capabilities.

Although chapter 2 is not vital information needed for the main work presented here, which is contained in chapters 3 to 5, it has been retained. It is beneficial background material on the imaging instrument for the reader to better understand the discussion of the experimental data obtained in chapter 6.

[1]The author of this work has been contacted but a satisfactory reply has yet to be received

2D MSE Imaging Instrument

As the Stark multiplet is nett unpolarized, simultaneous measurements of the polarization of the σ and π components requires spectral discrimination. The 2D MSE imaging instrument discussed in this thesis, consists of a polarization interferometer, which provides the spectral discrimination, and a Savart shearing plate with one additional interferometric technique, to allow the determination of the polarization orientation of the MSE multiplet.

The overall instrument is very compact, as it is comprised of birefringent optical components and simple polarizers, which is well suited to the limited space often encountered when trying to access the viewing ports on todays tokamaks. There are other attractive advantages of such an imaging system, which include: high photon throughput, due to the fact that no narrow band filters are necessary to isolate one of the components of the multiplet, the possibility of synchronous imaging of the plasma as well as the fact it is a 2D imaging system.

In this chapter the basic operating principles of the novel new instrument, a spectro-polarimeter, will be discussed. As the two main components of the spectro-polarimeter are variations of a two beam interferometer, a general description of the properties of an interferometer is given through a brief overview of the most common configuration of an interferometer, the Michelson ineterferometer. The basis of a polarization interferometer is then discussed followed by a description of a Savart shearing plate, which is a key element in producing spatial interference fringe patterns on which the polarization information of the MSE multiplet is encoded. The two instruments that have been used to gather experimental data are then briefly discussed, these are called the double spatial heterodyne spectro-polarimeter and the switching spatial heterodyne spectro-polarimeter.

2.1 Michelson interferometer

The basis of a Michelson interferometer is that an incident coherent light source is split into two beams, of equal amplitude, which traverse different paths before being recombined at a detector. By altering the path length of one of the beams, using a movable mirror, a time delay τ between the waves is introduced which causes interference between the two wave components at the detector. A schematic of the general setup of a Michelson interferometer can be seen in Fig. 2.1.

The detector will effectively see two radiation sources, with the total radiation the sum of the two beams. For an incident electric field described by the complex amplitude u(t), the total electric field reaching the detector can be written

$$V(t) = \frac{u(t) + u(t+\tau)}{2}. \tag{2.1}$$

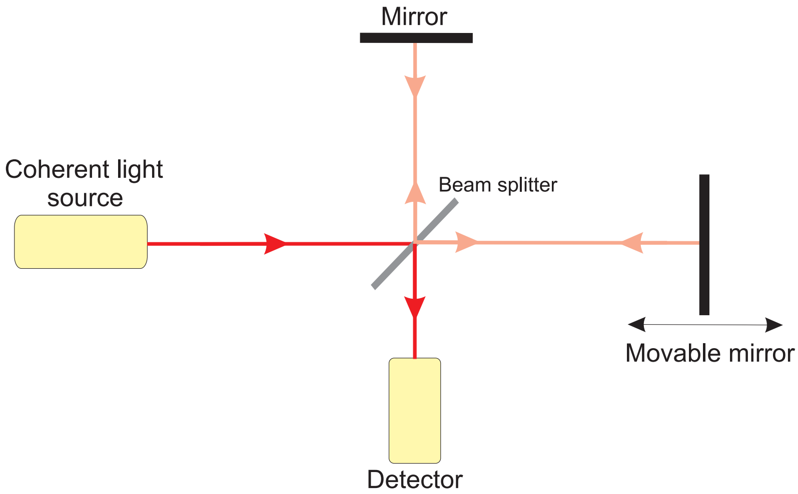

Figure 2.1: Schematic of a Michelson interferometer. A coherent light source is split into two beams, typically with a half-silvered mirror, where one path is fixed and the other can be altered, using a movable mirror, to produce a phase delay between the two beams. Once recombined the two beams interfere to generate an interference pattern (interferogram), whose intensity is varied by scanning the phase delay between the two beams.

The quantity that is measured at the detector is proportional to the time average of the square of the complex nett signal $V(t)$:

$$S = \langle V(t)V^*(t)\rangle, \tag{2.2}$$

which can also be written

$$S = \frac{I_0}{2}(1 + \mathcal{R}[\gamma(\tau)]), \tag{2.3}$$

where I_0 is the intensity of the incident radiation given by $\langle u(t)u^*(t)\rangle$, τ is the time delay introduced by the path length difference of the two split rays, $\mathcal{R}$ denotes the real part and $\gamma(\tau)$ is the complex coherence of the incident light source given by

$$\gamma(\tau) = \frac{1}{I_0}\langle u(t)u^*(t+\tau)\rangle. \tag{2.4}$$

From the Wiener-Khinchin theorem[21] this complex coherence γ is related to the Fourier transform of the spectral distribution $g(\nu)$ of the incident light source

$$\gamma(\phi) = \frac{1}{I_0}\int_0^\infty g(\nu)e^{2\pi i\nu\tau}d\nu. \tag{2.5}$$

If the interferometer is illuminated with quasi-monochromatic light with centre frequency ν_0, the intensity at the detector can be written in a simpler manner as

$$S = \frac{I_0}{2}[1 + \zeta\cos\phi], \tag{2.6}$$

where $\phi = 2\pi\nu_0\tau$ which is the phase delay between the two rays due to a time delay τ and $\zeta \equiv\mid \gamma \mid$ is the fringe visibility or contrast, dependent on the spectral line shape of the incident light through Eq.2.5.

This intensity interference pattern caused by the time delay τ between the two wave

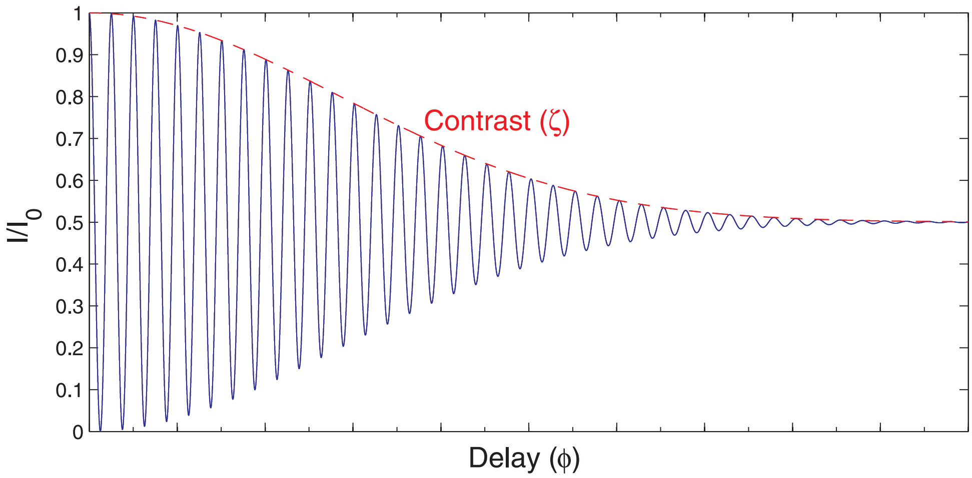

Figure 2.2: A model interferogram produced by a Michelson interferometer illuminated with a coherent light source with a gaussian spectral distribution (effective width $\Delta\nu/\nu \sim 1/12$). Overlaid is the contrast of the interferogram which is the fourier transform of the source's spectral line shape, in this case it is another gaussian.

components is called the interferogram. For ease of conceptualization Fig. 2.2 shows an ideal interferogram produced by a quasi-monochromatic source with a guassian spectral distribution of effective width $\Delta\nu/\nu \sim 1/12$.

2.2 Polarization interferometer

The simplest polarization interferometer for already linearly polarized light consists of a wave-plate and a polarizer. This is a static two beam interferometer as the incident polarized light will be split into two components with a fixed time delay τ between them introduced by the wave-plate. The two components are then combined at the analyzer to produce an interference pattern.

The splitting of the incident linearly polarized light arises as the wave-plate is a uniaxial birefringent material. It is constructed from a crystal that possesses a plane of symmetry, called the principal section, where light is only able to propagate if it is linearly polarized with its direction of vibration perpendicular to the principal section, such a ray is called an ordinary (O) ray, or if it is vibrating in the principal section, then it is called an extra-ordinary (E) ray [22]. The O ray passes through the crystal without deviation as the speed of propagation for this component is constant in all directions. However the speed of propagation for the E ray is equal to that of the O ray in one direction, this is defined as the optic axis [23], and reaches a maximum in the direction perpendicular to the optic axis. The direction of polarization for an O ray is thus termed the slow axis and the direction for an E ray the fast axis.

A wave-plate is a birefringent crystal which has its faces parallel to the optic axis, hence for propagation that is normal to the surface of the wave-plate the speed of propagation for the E ray is at a maximum. Thus for incident light which is resolved into an O and E ray, a time delay τ is introduced between the two polarized components that is dependent on the thickness of the wave-plate. This is equivalent to the rays traversing different path lengths in the Michelson interferometer.

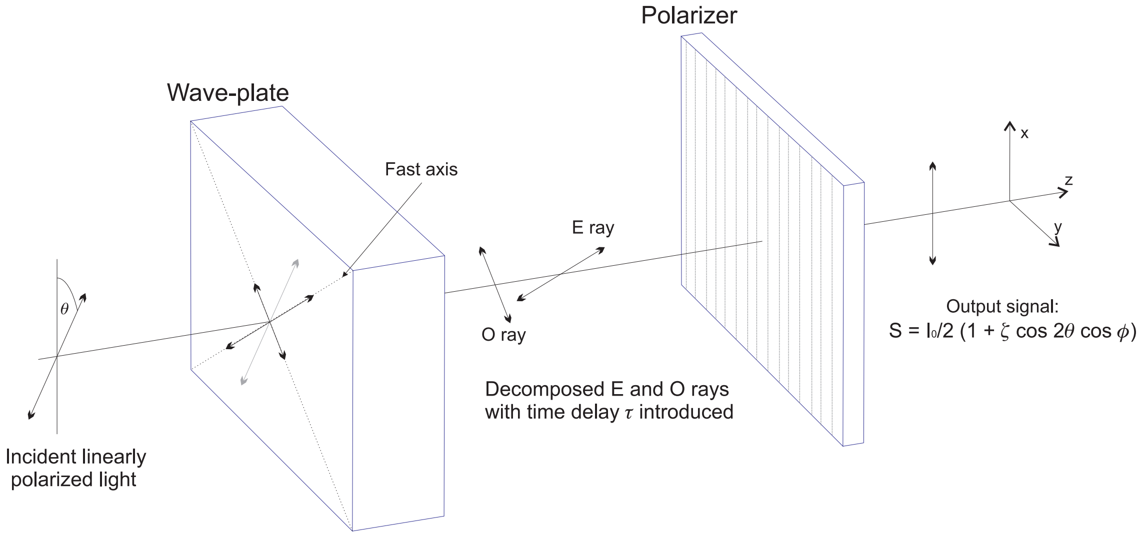

Figure 2.3: Schematic of a polarization interferometer comprised of a wave-plate and a polarizer, where the orientation of the wave-plate is such that it's fast axis is at 45^o to the axis of the polarizer. Incident linearly polarized light oriented at an angle θ from the axis of the polarizer is shown. Also, on the face of the wave-plate the two allowable orthogonally polarized components in which the light is resolved into are shown. As the speed of propagation of the component with polarization along the fast axis is greater than that of the other component, on exiting the two components will then have a time delay τ introduced. The two components are then caused to interfere by the final polarizer.

Throughout this thesis, the orientation of such an optical component will refer to the direction of the fast axis for a wave-plate and the polarization transmission axis for a polarizer. The convention used will be that the direction of propagation will be along the z-axis and the orientation of each component in the x-y plane will be given by the angle of the component from the x-axis.

For linearly polarized light incident on a wave-plate, whose fast axis is at 45^o, with polarization direction making an angle θ to that of the axis of the analyzer, which is at 0^o, the output intensity is given by [1]

$$S = \frac{I_0}{2}(1 + \zeta \cos 2\theta \cos \phi), \tag{2.7}$$

where I_0, ζ and $\cos\phi$ are the same as given above for the Michelson interferometer.

If the case where the incident polarization is co-aligned with either the fast or slow axis of the wave-plate ($\theta = \pm 45^o$) is considered, the output intensity of the instrument will be $I_0/2$ as expected, as the wave-plate will not decompose the incident ray. Thus the linearly polarized light will be incident on the polarizer with an angle of polarization $\pm 45^o$ to that of the axis of the polarizer.

If the incident rays are polarized with $\theta = 0^o$ then the intensity will be as given by Eq. 2.6. However, if the polarization is perpendicular to this ($\theta = 90^o$) then the interferogram is inverted as the $\cos 2\theta$ term goes to -1.

When the instrument is illuminated by the MSE multiplet the signal will be the sum of the signals for the orthogonally polarized σ and π components. Taking the orientation of the polarization of the σ component to be at an angle θ to the axis of the polarizer, the polarization of the π component is given by $\theta + 90^o$ and the intensity at the analyzer is thus

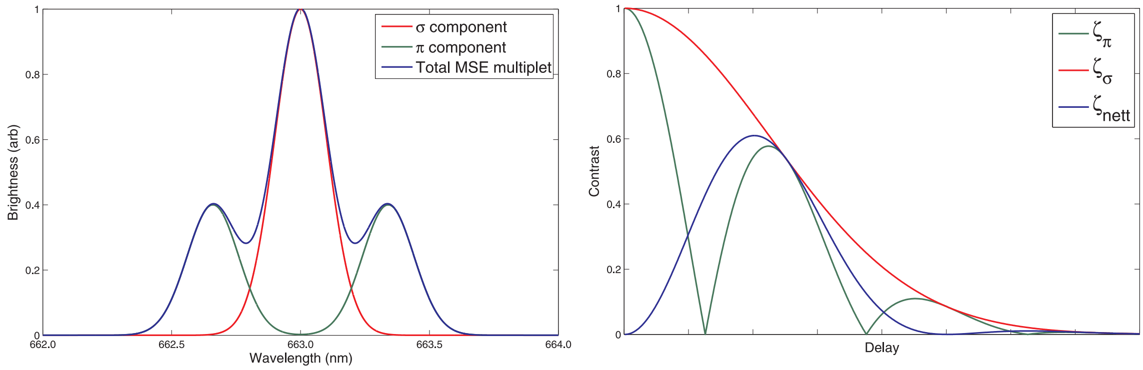

Figure 2.4: The figure on the left shows the line shape and relative brightness of the MSE multiplet which is comprised of a central σ component and two π components on either side. The right hand figure shows the the contrast ζ for an interferogram for the components σ and π analyzed independently as a function of delay. The nett contrast $\zeta_{nett} = (\zeta_\sigma - \zeta_\pi)/2$ is also shown which is produced when the entire MSE multiplet is analyzed simultaneously, it must be noted that the cusps of the π contrast are due to the phase of the interferogram changing which also produces the maximum of the nett contrast. It can be seen from this figure that a non-zero nett contrast can be produced by an appropriate choice for the optical delay.

$$S = \frac{I_\sigma}{2}(1 + \zeta_\sigma \cos 2\theta \cos \phi_\sigma) + \frac{I_\pi}{2}(1 - \zeta_\pi \cos 2\theta \cos \phi_\pi), \tag{2.8}$$

For simplicity, assuming that each component has equal irradiance $I_\sigma = I_\pi = I_0$ and identical centre-of-mass wavelengths ($\phi_\sigma = \phi_\pi$), equation 2.8 reduces to

$$S = \frac{I_0}{2}(1 + \zeta_{nett} \cos 2\theta \cos \phi), \tag{2.9}$$

where $\zeta_{nett} = (\zeta_\sigma - \zeta_\pi)/2$ is the nett contrast.

Due to the spectral shape of the multiplet (central σ component with two π wings, see Fig. 2.4) it is possible to produce a non-zero nett fringe contrast $\zeta_{nett}(\tau)$ by optimizing the thickness (optical delay) of the wave-plate. This is achieved by choosing the delay to be comparable to the temporal coherence of the multiplet. This non-zero nett fringe contrast provides the spectral discrimination needed in order to determine the polarization of the multiplet.

This simple polarization interferometer alone is unable to determine the polarization orientation of the MSE multiplet as it is a static interferometer, in the sense that the time delay τ is unable to be changed which means the interferogram of the MSE multiplet is unable to be determined. The output of this instrument is an intensity which is dependent on: the brightness of the MSE signal produced by the neutral heating beam as well as any other background source, the contrast which is sensitive to Doppler broadening of the line source, the polarization angle of the incident light and finally the phase which is dependent on the centre frequency of the MSE multiplet. However, through the addition of another birefringent optical components to this polarization interferometer a 2D MSE imaging system can be constructed which can determine just the polarization of the multiplet, the critical component which will deliver this is the Savart shearing plate.

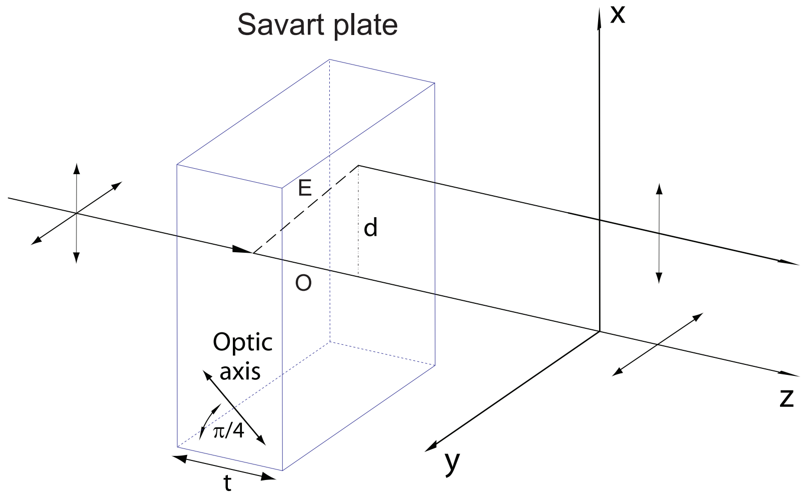

Figure 2.5: A ray diagram showing the paths of an extra-ordinary (E) and ordinary (O) ray through a Savart shearing plate. The principal section of the crystal is in the x-z plane and the optic axis is oriented at 45^o to the direction of propagation, which produces the spatial displacement (d) in the x-direction. An incident ray containing polarization components which correspond to the two allowable directions for propagation will exit the Savart plate parallel with a spatial separation d.

2.3 Savart shearing plate

A Savart shearing plate is a uniaxial birefringent optical plate that is cut such that the optic axis makes an angle of $\sim 45^o$ to the face of the plate (Fig. 2.5). As stated earlier, the O ray in such a crystal will pass through without deviation. However the E ray will propagate through the crystal at an angle which is determined by the direction of fastest propagation, the direction perpendicular to the optic axis. This causes an incident linearly polarized ray on the Savart plate to be resolved into orthogonally polarized components, for the same reason as the wave-plate, which is that the uniaxial crystal transmits vibrations in only two orthogonal directions. These rays emerge from the Savart plate parallel to each other and with a lateral displacement d, illustrated in Fig. 2.5. The formula for the displacement is [22]

$$d = \frac{n_o^2 - n_e^2}{n_o^2 + n_e^2} t, \tag{2.10}$$

where n_o and n_e are the refractive indices for the O and E ray respectively and t is the thickness of the plate.

As well as the spatial displacement of the two rays a Savart plate also introduces a path length difference between the E and O rays, which is given by [22]

$$\Delta = t \left(A + d \cos\omega \sin\theta_i + \cdots \sin^2\theta_i \cdots + \cdots \sin^4\theta_i + \cdots \right), \tag{2.11}$$

where

$$A = \left(\frac{2n_o^2 n_e^2}{n_o^2 + n_e^2} \right)^{\frac{1}{2}} - n_o, \tag{2.12}$$

θ_i is the angle of incidence and ω is the angle between the plane of incidence and the principal section of the crystal plate.

In our application, a Savart plate is inserted between the wave-plate and the polarizer,

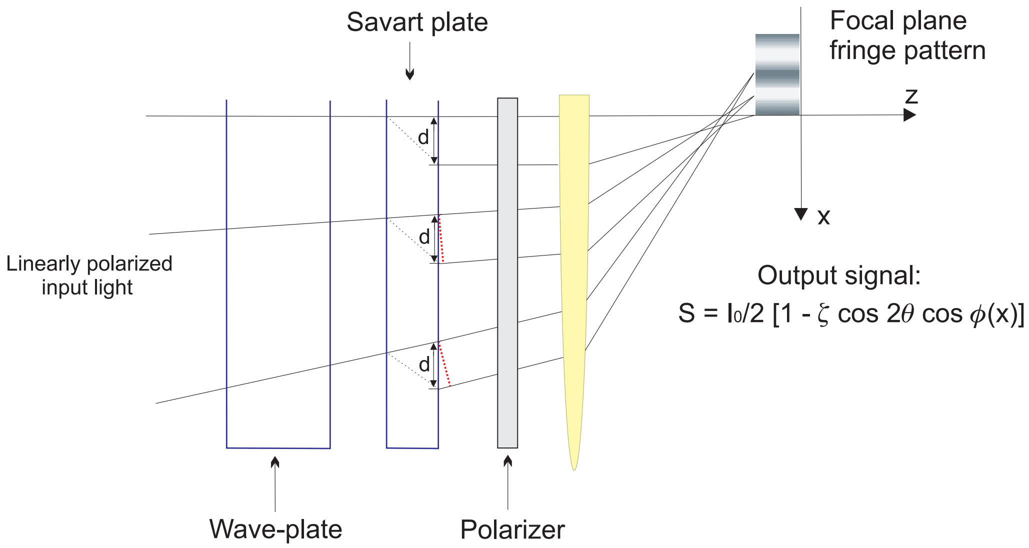

Figure 2.6: Schematic of the polarization interferometer with a Savart shearing plate inserted between the wave-plate and polarizer which is illuminated by linearly polarized light. Three rays shown represent three sightlines through the instrument. Once each ray has traversed the Savart plate, it is split into two rays of orthogonal polarization with a spatial separation d in the x-direction. As the angle of incidence increases with position from the centre of the image, an increasing path difference between the two beams is introduced, and hence a position dependent phase difference $\phi(x)$ is produced across the image. Once the rays are brought together interference occurs which produces a sinusoidal fringe pattern. This represents a segment or extract of the interferogram with wave-vector in the x-direction.

oriented such that the principal section is co-aligned with the principal section of the wave-plate. For this configuration the fast axis of both plates are aligned, both plates will be oriented at 45^o, which means that the orthogonally polarized components exiting the wave-plate will then continue to propagate through the Savart plate with the same polarization direction.

This path length difference between the two split rays is equivalent to introducing a phase delay ϕ which is dependent on the angle of incidence of a given ray. As the final 2D image subtends a range of angles through the Savart plate, this phase delay across the image will be position dependent. As the Savart plate and the wave-plate are co-aligned the phase delay introduced between the resolved rays is additive. Ignoring field of view effects, the wave-plate introduces a fixed offset phase delay and the Savart plate introduces a phase delay which is position dependent. Choosing to orient the instrument such that the separation d is in the x-direction, the total phase delay will be $\phi \equiv \phi(x)$. The output signal of this simple polarization interferometer with a Savart plate can then be written as

$$S = \frac{I_0}{2}[1 - \zeta_{nett} \cos 2\theta \cos \phi(x)]. \tag{2.13}$$

As the rays pass through the final polarizer and are focused onto the focal plane they interfere producing a segment of the interferogram across the image. The wave vector of the resulting sinusoidal fringe pattern is oriented in the x-direction. Figure 2.6 illustrates the setup for this instrument, with 3 rays of varying incidence shown to help illustrate the concepts of a Savart shearing plate and the fringe pattern produced.

Through the addition of the Savart plate to the instrument, a fringe pattern is now produced across the image ($\cos\phi(x)$ term in Eq. 2.6) with the fringe visibility not only dependent on the polarization orientation of the MSE multiplet but also the contrast ($\zeta_{nett}\cos 2\theta$ term). In order to discern changes in the fringe visibility due to changes in the the polarization orientation of the multiplet or from changes in the contrast, additional interferometric techniques must be utilised.

Also with the addition of the Savart plate, unpolarized background light entering the instrument will now only change the total intensity of the image. However if there is polarized background emission the overall interferogram will be changed.

2.4 Spectro-polarimeters

The two spectro-polarimeters which are used for imaging the MSE multiplet are comprised of the basic instrument (a wave-pate, Savart shearing plate and polarizer) as discussed in the previous sections and one additional interferometric technique.

The first of these is called the double spatial heterodyne spectro-polarimeter. This is constructed with a second Savart shearing plate oriented in such a manner to produce orthogonal interference fringes to that of the Savart plate in the basis instrument. This produces a 2D fringe pattern with the visibility of the orthogonal components proportional to $\cos 2\theta$ and $\sin 2\theta$, with the fringe contrast ζ common to both.

The second system is called the switching spatial heterodyne spectro-polarimeter. Through the addition of a quarter wave-plate to the basis instrument, this system shifts the polarization dependence to the phase domain of the fringe pattern. This causes variations of the polarization orientation to manifest itself in changes of the position of the fringe pattern in the final image. However, as the phase of the fringe pattern is not well known, a modulating element which switches the phase delay produced by the multiplet between two states is used, allowing the phase shift produced by changes in the polarization to be determined.

Only a brief overview of the optical layout and final form of the intensity S across the image of each of these instruments is given here. For a more in depth analysis the reader is referred to [1].

2.4.1 Double spatial heterodyne spectro-polarimeter

The first element in the optical chain of the double spatial spectro-polarimeter is a compensated zero-nett delay double Savart plate with its principal section at -45^o with respect to the x-axis. This orientation produces vertically separated rays with polarization $\pm 45^0$.

Following the first Savart plate is a wave plate having its fast axis oriented parallel with the x-axis. When one sets the delay of the 'primary' wave plate provides the spectral discrimination by choosing the delay such that it is comparable to the temporal coherence of the multiplet. It is this mutual delay introduced to the orthogonal components of the separated rays from the Savart plate which gives rise to a non-zero effective contrast ζ. This is followed by a single Savart plate oriented with its optical axis in the $x - z$ plane (co-aligned with the primary wave plate). This plate separates the waves in the x direction producing horizontal fringes on the detector whilst also introducing a small fixed delay. A final polarizer oriented at 45^o causes the various x and y polarized waves to interfere producing orthogonal vertical and horizontal fringe patterns, with there visibility dependent on the polarization of the incident light. Figure 2.8 shows calibration images of

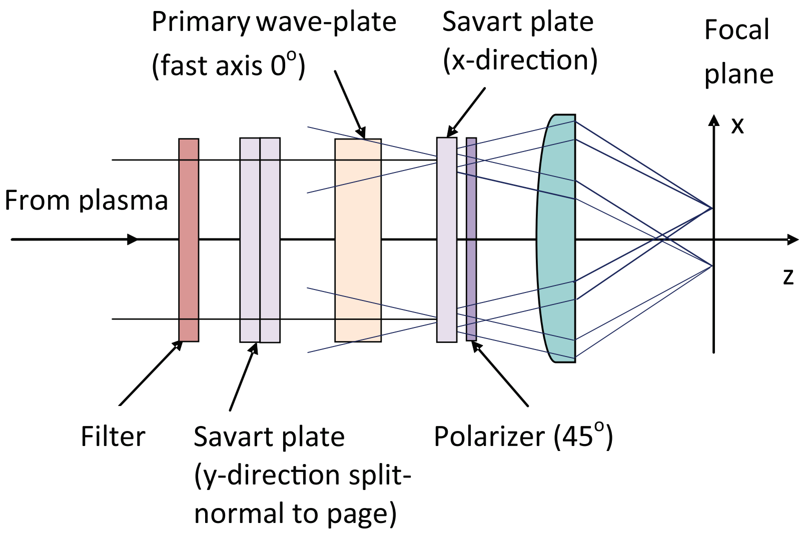

Figure 2.7: Optical arrangement of the double spatial heterodyne spectro-polarimeter.

this system which illustrates the change in the fringe pattern for varying incident polarized light.

A Jones matrix analysis of the optical system response has been completed elsewhere [1]. The irradiance distribution of the image as a function of position across the focal plane is found to be

$$\begin{aligned} S(x,y) &= \frac{I_0}{2}[1+\zeta[\cos 2\theta \cos\phi_2(x) + \sin 2\theta \sin\phi_2(x)\sin\phi_1(y)]], && (2.14)\\ I_0 &= I_\pi + I_\sigma, && (2.15)\\ \zeta &= \frac{I_\sigma\zeta_\sigma - I_\pi\zeta_\pi}{I_\sigma + I_\pi}, && (2.16)\end{aligned}$$

where I_0 is the total multiplet irradiance and ζ is the nett fringe contrast that depends on the polarized component relative intensities (nominally $I_\pi = I_\sigma$), as well as their separation and broadening. The position dependent phase delay $\phi_1(y)$ corresponds to the first Savart plate in the optical chain and $\phi_2(x)$ is due to the second which produces the spectral discrimination.

2.4.2 Switching spatial heterodyne spectro-polarimeter

A purely phase modulated system can be constructed by replacing the first Savart plate in the double heterodyne system with a quarter wave plate and a half-wave ferro-electric liquid crystal (FLC). Through the introduction of a quarter wave-plate, the delay ϕ_1 is now $\phi_1 = \pi/2$ and Eq. 2.14 becomes

$$S(x) = \frac{I_0}{2}[1+\zeta\cos(\phi_2(x) - 2\theta)]. \qquad (2.17)$$

The polarization information is now carried as a phase modulation of the spatial carrier $\phi_2(x)$. As the phase $\phi_2(x)$ is not absolutely known and will vary due to Doppler shifts of the multiplet centre wavelength, modulation methods are required to recover the polarization orientation θ. The modulation used is a temporal shift of the $\phi_2(x)$ carrier through the

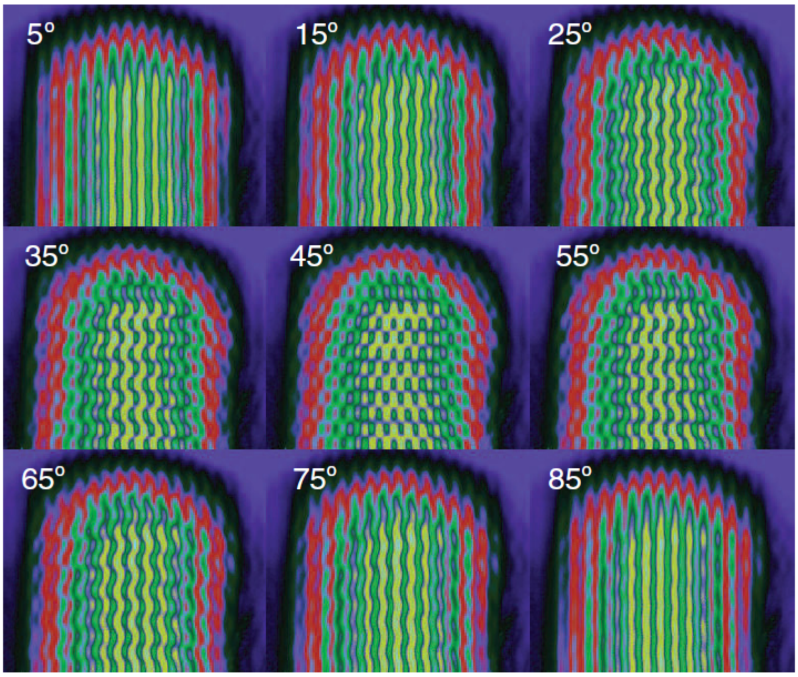

Figure 2.8: Images of a magnetized zinc lamp at 468 nm with the double spatial heterodyne spectro-polarimeter illustrating the resultant 2D fringe pattern. The magnetic field is oriented in the plane of the image. Left to right and top to bottom: the polarization of the multiplet is rotated in 10^o increments. The numbers indicate the nominal values for the polarization angle θ.

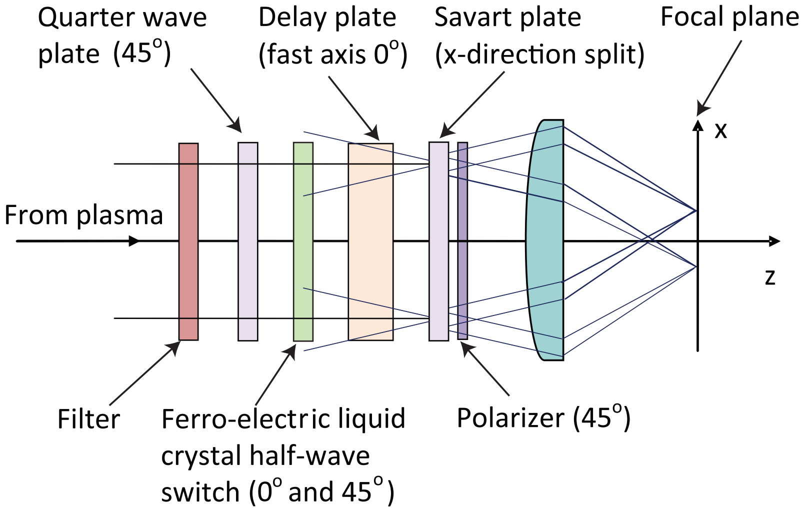

Figure 2.9: Optical arrangement of the switching spatial heterodyne spectro-polarimeter.

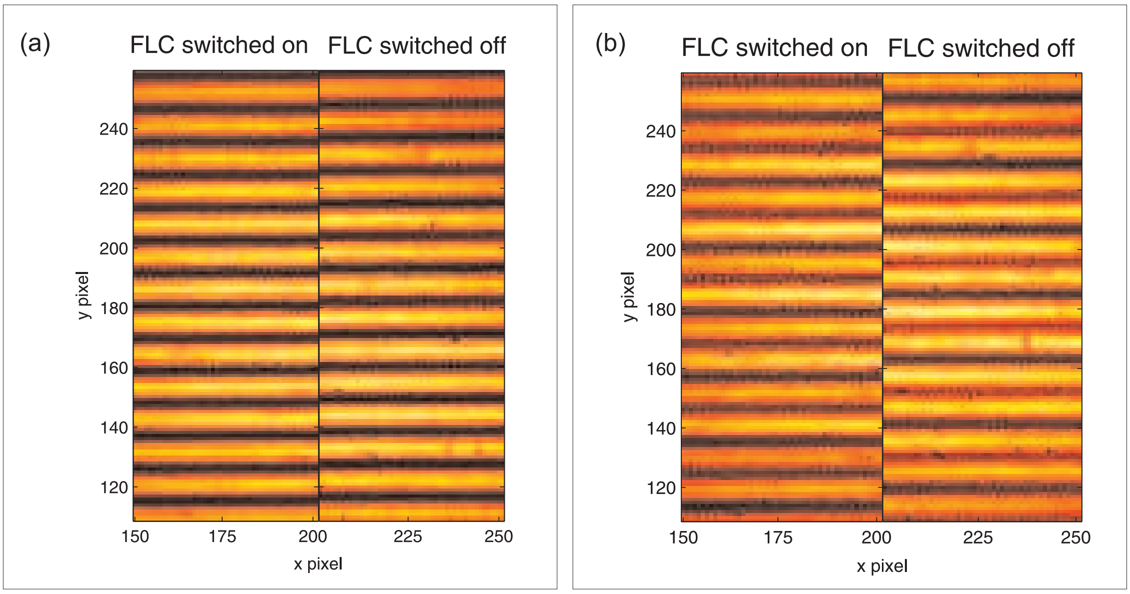

Figure 2.10: Two calibration images for the switching spatial heterodyne spectro-polarimeter, illustrating the change in the observed fringe pattern between the two states of the FLC. **(a)** corresponds to a source illuminating the system with a small polarization angle θ, resulting in only a small change in the fringe pattern between the two states of the FLC and **(b)** corresponds to the incident light having a polarization angle $\theta \approx 22.5^o$ producing $\sim \pi/2$ phase shift between the fringe patterns of the two states of the FLC.

fast switching (10 μs) FLC wave plate. When a 5 volt bias across the FLC is reversed, the optical axis of this component rotates by 45^o, hence producing two states from which the phase change due to the polarization orientation of the MSE multiplet can be extracted.

The first element in the optical chain is the quarter-wave plate which is oriented at 45^o with respect to the x-axis. The FLC is the next element with its optical axis in the un-switched state oriented at 0^o. The rest of the optical chain is exactly the same as in the double spatial heterodyne system. The resulting image states are given by [1]

$$S_-(x) = \frac{I_0}{2}[1 - \zeta \cos(\phi_2(x) - 2\theta)], \tag{2.18}$$

$$S_+(x) = \frac{I_0}{2}[1 + \zeta \cos(\phi_2(x) + 2\theta)]. \tag{2.19}$$

The form of these equations can easily be verified by substituting $\phi_1(y) = \pm 45^o$ in Eq. 2.14.

Figure 2.10 contains a portion of two raw calibration images for the switching system, where in **(a)** the system has been illuminated with a polarized source with a small polarization angle θ and **(b)** is illuminated with a polarization angle $\theta \approx 22.5^o$. The image shown in each of the figures is comprised of adjacent sections of the raw images for successive frames, where the left image corresponds to the FLC switched on and the right when it is switched off. Hence each section of the image illustrates the two states of the pitch angle equation, Eq. 2.18 and 2.19. With a small polarization angle θ there is only a small change in the phase of the fringe pattern, resulting in only a small shift between the two states, as can be seen in Fig. 2.10 **(a)**. When $\theta \approx 22.5^o$ there will be a phase shift between the two states of the fringe pattern of $\approx 90^o$, which is seen in Fig. 2.10 **(b)**.

Illuminating this system with a polarized source which is not constant across the field of view, such as the emission from the neutral heating beam, will result in the phase shift of the fringe pattern between the two states of the system varying across the field of view. Through Fourier techniques, the phase difference between two successive frames can be extracted and hence the polarization angle of the source emission across the view. As this process must use two successive frames, it can only be used when the polarization angle across the field of view does not change significantly between the two frames.

With a grounding in the instruments used to measure the internal magnetic pitch angle, the focus of this thesis will now shift to understanding the fundamentals behind the magnetic pitch angle itself and the implications this has for the capabilities of this 2D MSE imaging system. The instruments themselves are revisited when the deployment of these systems on the DIII-D tokamak is discussed in chapter 6.

Chapter 3

Principles of a 2D MSE System

To understand the capabilities of the new 2D imaging system, the underlying equation which links the magnetic pitch angle to the measured polarization angle of the MSE multiplet is investigated in this chapter. As this measurement is the projection of the polarization angle of Stark multiplet, defined by $\mathbf{E} = \mathbf{v} \times \mathbf{B}$, onto the viewing plane of the instrument; the neutral beam, internal magnetic field and the view of the instrument must all be considered in allowing the magnetic pitch angle equation to be derived. The link between these components is achieved by expressing the neutral beam velocity and the internal magnetic field as well as the instrument view of the neutral beam from an arbitrary position in terms of the natural basis of the tokamak, a cylindrical coordinate system. This derivation also provides the basis for the modelling of later chapters.

Because an imaging system is considered, it is essential to take account of the spatial variation of the beam velocity vector (beam divergence). This chapter extends previous simple analyses in which it was valid to ignore the beam divergence. For imaging systems, it is shown that it is extremely important to accurately take account of the beam velocity profile.

The properties of this equation are then explored for some special case viewing geometries. Through a consideration of these properties, the additional information which the 2D system captures over the conventional discrete channel 1D MSE system is considered. As this new system can inherently capture 2D information, an investigation into the possibility of extracting magnetic field perturbations associated with instabilities using synchronous imaging techniques follows.

3.1 Co-ordinate system used to describe viewing geometry

A MSE instrument analyzes the polarization angle of the emission from the atoms of the neutral heating beam. As the neutral heating beam has non-zero width, it will be the accumulated emission along a sight line which is measured. In order construct a general formalism to take this line integration effect into account, the neutral beam is divided in a number of ideal vertical slices or *sheets*. Using these sheets, one can consider the emission across the view of an instrument as the that which originates from the points where the sight-line intersects the sheet.

The natural coordinate system for spatial positions within a tokamak is the cylindrical basis (Fig. 3.1), where any point is described by: the radius R from the centre of the tokamak, the height Z from the mid-plane of the tokamak and the toroidal angle ϕ.

Some simplifications arise by orienting the (R, Z, ϕ) tokamak co-ordinate system such that the central sheet of the neutral beam propagates antiparallel to the x-axis of the basic cartesian system (see Fig. 3.2).

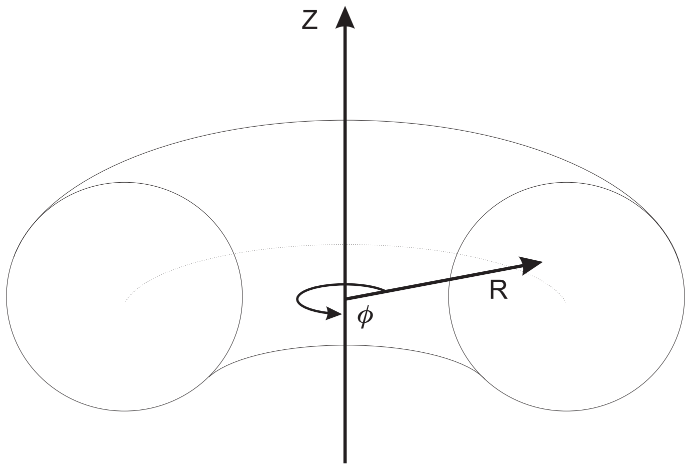

Figure 3.1: Schematic of a section of a tokamak which illustrates the natural cylindrical coordinate system used to describe a position within the tokamak.

The sight lines of the 2D instrument originate from a view origin and are defined by two angles: a horizontal angle χ (in the $x-y$ plane) and vertical angle θ (out of the $x-y$ plane). When the view of such a system is not inclined from the horizontal plane of the tokamak, the horizontal angle χ is simply related to the toroidal angle ϕ. For the case of the 2D imaging system, considered here, images of the plasma are assumed to be taken with a CCD camera oriented such that it looks along the horizontal mid-plane of the tokamak.

With reference to Fig. 3.2 the position of the instrument and hence the view origin is given by the co-ordinates $(R_0, 0, \delta)$. As the coordinate system is oriented such that the central sheet is parallel to the x-axis, the equation for this sheet is simply $y = R_y$.

Defining the horizontal angle of the instrument χ from the x-axis (Fig. 3.2), the intersection of a sight-line in the horizontal midplane ($\theta = 0$) and the sheet is given by

$$y_i = R_y, \tag{3.1}$$

$$x_i = \frac{R_y - y_o}{\tan\chi} + x_o, \tag{3.2}$$

where x_o and y_o are the (x, y) coordinates of the viewing origin. The intersection point in cylindrical coordinates is

$$R = \sqrt{x_i^2 + y_i^2}, \tag{3.3}$$

$$\phi = \tan^{-1}\frac{y_i}{x_i}. \tag{3.4}$$

For a sightline which is inclined to the midplane, the vertical position Z is given by

$$Z = P\tan\theta. \tag{3.5}$$

where P is the length shown in Fig. 3.2, given by

$$P = \sqrt{R^2 + R_0^2 - 2RR_0\cos\eta}. \tag{3.6}$$

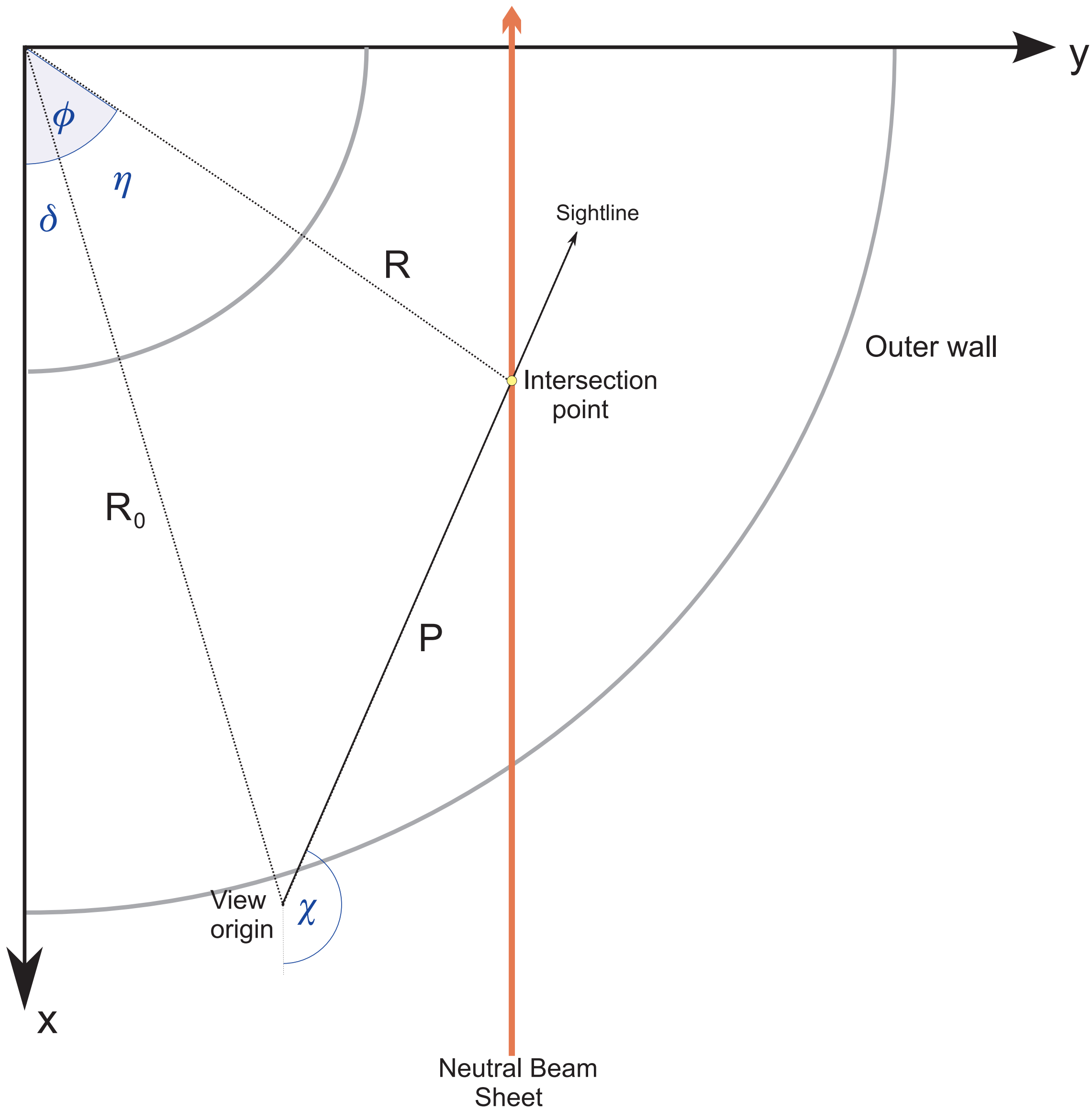

Figure 3.2: Schematic plan view of an individual sightline, described by the angle χ, showing the intersection point with a neutral beam sheet. The coordinates (R_0, δ) used to describe the viewing origin of the system are shown as well as the radius R of the intersection point and the base length P from the view origin to the intersection point. The toroidal angle ϕ from the x-axis is shown along with η used to determine P.

where $\eta = \phi - \delta$.

For any viewing geometry the corresponding spatial positions of the intersection point of a given sight line and the central sheet in terms of the cylindrical (R, Z, ϕ) coordinates is now given.

3.2 Description of the neutral heating beam

For a complete representation the non-zero width of the neutral heating beams must be considered.

In the case of an ideal beam, in which the velocities of all atoms are parallel, the beam is split up to n sheets, where each of these sheets will be parallel and separated by equal an distance $\Delta_b = w_b/n$, where w_b is the width of the beam. Thus it is trivial to find the points of intersection of any sight line and sheet by following the method explained in the previous section with varying R_y, corresponding to the position which the sheet crosses the y-axis.

However, neutral beams are not ideal and tend to diverge. Through extensive studies of the installed beams on various tokamaks the value for the maximum beam divergence is generally well known[24][25]. As a first order approximation it will be assumed that the beam originates from a point in the midplane and that it diverges uniformly from its origin. As the horizontal and vertical dimensions of a neutral beam may not be equal, a horizontal and vertical origin for the beam is set. For such a beam, the motion of atoms can be described by the magnitude of the velocity v_0 and the angles ι (horizontal) and ξ (vertical), where these angles are from the origin of the neutral beam.

The sheets in this case will be vertical slices of the neutral beam arranged at varying horizontal angles ι. In order to find the (R, Z, ϕ) coordinates of the intersection point between a sight-line and the sheet, the same method as described in the previous section will be followed. The equations for a sight-line and sheet in the midplane are respectively

$$y = \tan\chi(x - x_o) + y_o, \tag{3.7}$$
$$y = \tan\iota(x - x_h) + y_h, \tag{3.8}$$

where (x_o, y_o) are the coordinates of the view origin of the instrument and (x_h, y_h) are the coordinates of the horizontal origin of the neutral beams. Thus the coordinates for the intersection point are given by

$$x_i = \frac{\tan\chi x_{vo} - \tan\iota x_{bho} + y_{bho} - y_{vo}}{\tan\chi - \tan\iota}, \tag{3.9}$$
$$y_i = \tan\chi(x_i - x_{vo}) + y_{vo}. \tag{3.10}$$

The corresponding cylindrical coordinates are given by Eqs. 3.3 and 3.4.

To determine the polarization angle of the MSE multiplet the velocity of the atoms within the neutral beam is expressed in terms of the basis vectors $(\hat{\mathbf{R}}, \hat{\mathbf{Z}}, \hat{\phi})$. The velocity of the atoms at an intersection point can be resolved into the vertical component v_Z and horizontal component v_h by using the vertical angle ξ:

$$v_Z = v_0 \sin\xi, \tag{3.11}$$

$$v_h = v_0 \cos\xi. \tag{3.12}$$

Defining the angle α between the velocity component in the midplane and the unit vector $\hat{\phi}$ (Fig. 3.3), the velocity can be separated into $\hat{\mathbf{R}}$ and $\hat{\phi}$ components. The angle α is given by

$$\alpha = \frac{\pi}{2} - \phi + \iota. \tag{3.13}$$

Thus the $(\hat{\mathbf{R}}, \hat{\phi})$ components of the velocity are

$$v_R = -v_h \sin\alpha, \tag{3.14}$$

$$v_\phi = v_h \cos\alpha, \tag{3.15}$$

where the velocity v_h is that of Eq. 3.12. The resolution of the general velocity vector at an intersection point is illustrated in Fig. 3.3.

The complete description of the velocity of an atom in this ideal divergent beam at any intersection point is

$$\mathbf{v} = v_0(-\sin\alpha\cos\xi\hat{\mathbf{R}} + \sin\xi\hat{\mathbf{Z}} + \cos\alpha\cos\xi\hat{\phi}), \tag{3.16}$$

where v_0 is the magnitude of the velocity at the given point, which does not need to be known (this will become evident in the next section).

3.3 Equation describing magnetic pitch angle

The polarization orientation of the σ and π components of the motional Stark split emission from the neutral heating beam is set by the relative direction of the induced electric field, due to the motion of the atoms across the magnetic field as well as any large internal electric field of the tokamak ($\mathbf{E}_{tot} = \mathbf{E}_{internal} + \mathbf{v} \times \mathbf{B}$). It has been shown by Rice *et al* [26] that in some enhanced confinement regimes in tokamaks, a strong radial electric field E_R is present which can alter the pitch angle by a non-negligible amount. However, this is not normally the case, and in any case such effects go beyond the scope of this thesis and will not be considered.

By measuring the orientation of the polarized emission, the direction of the induced electric field $\mathbf{E}$ can be found and linked to the relative amplitudes of the magnetic field components (B_R, B_Z, B_ϕ).

Each sight-line of the instrument is only able to resolve the direction of the polarization which is projected on to it's viewing plane, which is normal to the sight-line. Defining the unit vector $\hat{\mathbf{i}}$ to describe a sight-line and $\hat{\mathbf{j}}, \hat{\mathbf{k}}$ to span the associated viewing plane. Figure 3.4 illustrates these unit vectors for an arbitrary sight-line and neutral beam sheet. To express these unit vectors in cylindrical coordinates the angle β is introduced. It is defined as the angle in the midplane between the unit vectors $\hat{\phi}$ and $\hat{\mathbf{i}}$. The value of β is

$$\beta = \pi + \iota - \chi - \alpha. \tag{3.17}$$

The unit vector of the sight line $\hat{\mathbf{i}}$, is given by

$$\hat{\mathbf{i}} = \sin\beta\cos\theta\hat{\mathbf{R}} + \sin\theta\hat{\mathbf{Z}} + \cos\beta\cos\theta\hat{\phi}, \tag{3.18}$$

where θ is the vertical angle between the sight line and the mid-plane (Fig. 3.4).

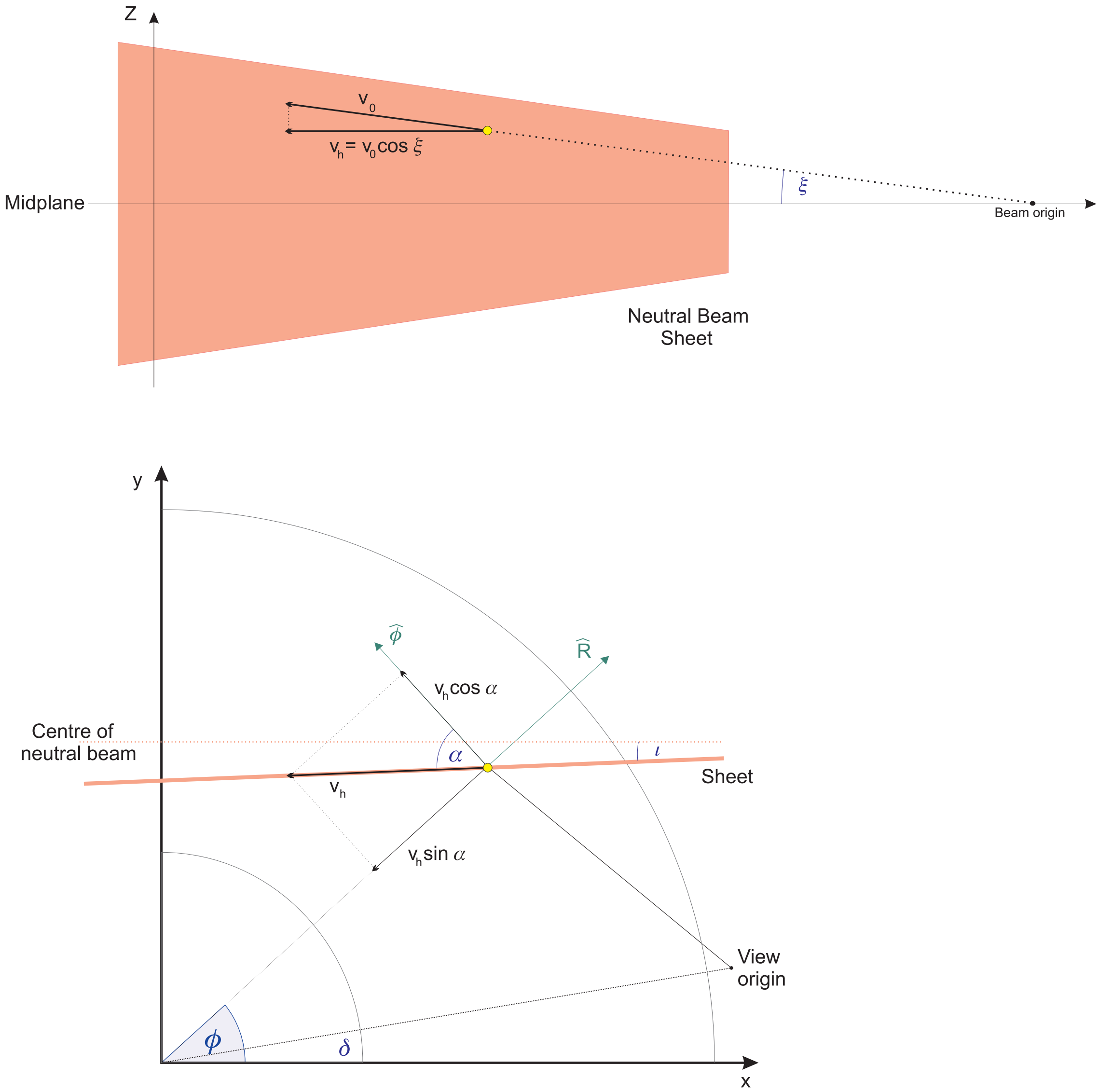

Figure 3.3: The top figure is a side on view of a neutral beam sheet showing the angle ξ, which describes the vertical component of the velocity of the atoms for ideal beam divergence. The lower figure is a plan view of the tokamak illustrating the decomposition of the horizontal component v_h, as shown in the upper figure, into the toroidal $\hat{\phi}$ and radial $\hat{\mathbf{R}}$ components. Note the beam divergence has been exaggerated for the purpose of this illustration.

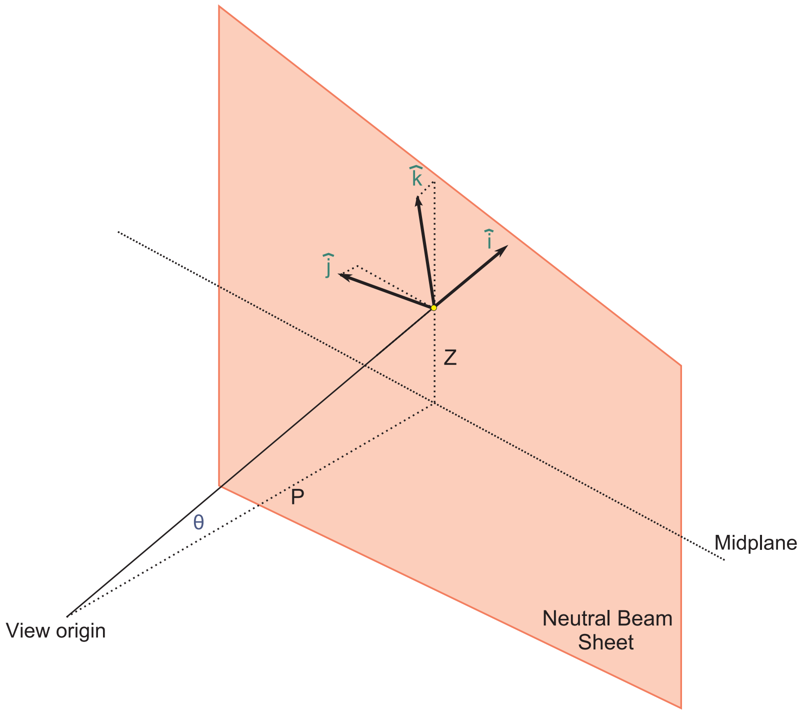

Figure 3.4: 3D schematic of a neutral beam sheet and a sightline of the imaging system, illustrating the unit vector $\hat{\mathbf{i}}$ describing the sightline and the unit vectors $\hat{\mathbf{j}}$ and $\hat{\mathbf{k}}$ which describe the viewing plane for that sightline. Note that $\hat{\mathbf{j}}$ is defined such that it is parallel with the midplane.

As it is the vertical and horizontal components of the magnetic field (B_R, B_Z) which are of interest, the unit vector $\hat{\mathbf{j}}$ has been defined such that it has no $\hat{\mathbf{Z}}$ component. The orthogonal unit vector $\hat{\mathbf{k}}$ is then given by the cross product of $\hat{\mathbf{i}}$ with $\hat{\mathbf{j}}$. The viewing plane unit vectors are given by

$$\begin{aligned} \hat{\mathbf{j}} &= -\cos\beta\hat{\mathbf{R}} + \sin\beta\hat{\phi}, & (3.19) \\ \hat{\mathbf{k}} &= -\sin\beta\sin\theta\hat{\mathbf{R}} + \cos\theta\hat{\mathbf{Z}} - \cos\beta\sin\theta\hat{\phi}. & (3.20) \end{aligned}$$

The induced electric field $\mathbf{E} = \mathbf{v} \times \mathbf{B}$ for an atom at any intersection point is found using the equation for the velocity of the atom, Eq. 3.16, and the total magnetic field represented in cylindrical components:

$$\mathbf{B} = B_R\hat{\mathbf{R}} + B_Z\hat{\mathbf{Z}} + B_\phi\hat{\phi}. \tag{3.21}$$

The form of the induced electric field is

$$\begin{aligned} \mathbf{E} &= v[(\cos\alpha\cos\xi B_z - \sin\xi B_\phi)\hat{\mathbf{R}} - (\sin\alpha\cos\xi B_\phi + \cos\alpha\cos\xi B_R)\hat{\mathbf{Z}} \\ &\quad +(\sin\xi B_R + \sin\alpha\cos\xi B_z)\hat{\phi}]. & (3.22) \end{aligned}$$

The components of the induced electric field projected onto the viewing plane of a sightline is given by the dot product of the two unit vectors describing the viewing plane,

$\hat{\mathbf{j}}, \hat{\mathbf{k}}$, and the electric field $\mathbf{E}$. These two components are

$$E_j = \hat{\mathbf{j}} \cdot \mathbf{E} = v[\sin\xi(\sin\beta B_R + \cos\beta B_\phi) - \cos(\alpha+\beta)\cos\xi B_Z], \tag{3.23}$$

and

$$\begin{aligned} E_k = \hat{\mathbf{k}} \cdot \mathbf{E} \;\; &= \;\; v[-(\cos\beta\sin\theta\sin\xi + \cos\alpha\cos\theta\cos\xi)B_R \\ &\quad - \sin(\alpha+\beta)\sin\theta\cos\xi B_Z + (\sin\beta\sin\theta\sin\xi - \sin\alpha\cos\theta\cos\xi)B_\phi]. \end{aligned} \tag{3.24}$$

The angle of the polarized emission is given by the ratio of these two components of the electric field. For the angle to be zero at the horizontal axis of the image captured and increase counter clock-wise, the pitch angle γ is defined by the ratio

$$S = \tan\gamma = \frac{E_k}{-E_j}, \tag{3.25}$$

and hence

$$\boxed{\begin{aligned} S &= \frac{a_1 B_R + a_2 B_Z - a_3 B_\phi}{\sin\xi(\sin\beta B_R + \cos\beta B_\phi) - \cos(\alpha+\beta)\cos\xi B_Z}, \qquad (3.26) \\ a_1 &= \cos\beta\sin\theta\sin\xi + \cos\alpha\cos\theta\cos\xi, \\ a_2 &= \sin(\alpha+\beta)\sin\theta\cos\xi, \\ a_3 &= \sin\beta\sin\theta\sin\xi - \sin\alpha\cos\theta\cos\xi, \end{aligned}}$$

This is the basic equation which describes the polarization angle projected onto the viewing plane of a sightline for a general 2D MSE imaging instrument. As it is the ratio of magnitudes of the two orthogonal induced electric fields, E_j and E_k, there is no dependence on the magnitude of the velocity in the final form, only the velocity direction.

3.3.1 1D simplification

As the conventional 1D MSE systems are constructed such that their view is along the midplane or tilted by a small angle with respect to it (θ small) the section of the neutral beam viewed can be considered to have its velocity entirely in the midplane ($\xi = 0$). As a result Eq. 3.26 reduces to

$$S = \frac{\cos\alpha\cos\theta B_R + \sin(\alpha+\beta)\sin\theta B_Z + \sin\alpha\cos\theta B_\phi}{-\cos(\alpha+\beta)B_Z}, \tag{3.27}$$

which agrees with the standard form given in literature [26].

As θ and B_R near the midplane are small, the above equation can be approximated by

$$S \approx \frac{\sin\alpha B_\phi}{-\cos(\alpha+\beta)B_Z}. \tag{3.28}$$

Since the toroidal field (B_ϕ) and the geometric angles (α, β) are well known, this simple equation provides a very important link to the vertical magnetic field, and is used extensively as a constraint in numerical equilibrium reconstruction codes.

3.4 Simplified 2D pitch angle equation

The full magnetic pitch angle equation (Eq. 3.26) describing the polarization angle of the MSE multiplet for a 2D system is quite complex. It is important to identify the major terms contributing to the pitch angle in order to compare the information gathered with this novel new 2D system to that of the conventional 1D instruments and so to assess its capabilities.

In practice the neutral beam divergence is small, ranging from approximately -2 to 2^o. As a result the vertical size of the neutral beam is relatively small, in the order of 0.5 m, so that the vertical viewing angle θ is also small, typically -5 to 5^o. Taylor expanding the trigonometric terms dependent on these values in Eq. 3.26 and neglecting terms which are second or higher order, the pitch angle equation simplifies to

$$S \approx \frac{\cos\alpha B_R + \theta\sin(\alpha+\beta)B_Z + \sin\alpha B_\phi}{\xi(\sin\beta B_R + \cos\beta B_\phi) - \cos(\alpha+\beta)B_Z}. \tag{3.29}$$

This equation retains the dominant terms for each of the magnetic field components in the numerator and denominator. Further simplifications can be considered for particular viewing geometries, which will be discussed shortly.

3.4.1 Effect of neutral beam divergence

The beam divergence term ξ introduces an additional unknown into the pitch angle equation for a 2D MSE imaging system. If accurate information about the poloidal magnetic field components is to be extracted from a 2D pitch angle image, the profile of ξ must be well known across the view of the system in order to allow the removal of its dependence. For particular viewing geometries, where the terms of the denominator are comparable, the magnetic pitch angle map is sensitive to the beam divergence, with a large change observed in the expected form of the pitch angle when comparing the no beam divergence and divergence cases (figures illustrating this are shown in chapter 5, Fig. 5.5 & 5.6).

As ξ only appears in the denominator, it is possible to determine the velocity profile by imaging the neutral beam when there is no poloidal magnetic field present. Such conditions are routinely employed within tokamaks to calibrate other diagnostics. These shots are called "beam-into-gas", where the neutral beams are fired into the tokamak with only the toroidal magnetic field present and no plasma. For such a situation the full pitch angle equation, Eq. 3.26, reduces to

$$S_{gas} = \frac{\sin\beta\sin\theta\sin\xi - \sin\alpha\cos\theta\cos\xi}{\sin\xi\cos\beta}. \tag{3.30}$$

As the geometrical angles α, β and θ are well known for a given viewing geometry, the above equation can be rearranged to give an expression for the horizontal divergence angle ξ of the neutral heating beam over the entire view of the system.

$$\tan\xi = \frac{\sin\alpha\cos\theta}{\tan\beta\sin\theta - S_{gas}}. \tag{3.31}$$

This method to determine the horizontal divergence ξ is dependent on how accurate the pitch angle S_{gas} can be measured. A large number of images of the neutral beam can be taken during dedicated calibration beam-into-gas shots, allowing S_{gas} to be locked down with high confidence.

The 2D MSE imaging systems which have been developed also intrinsically provide

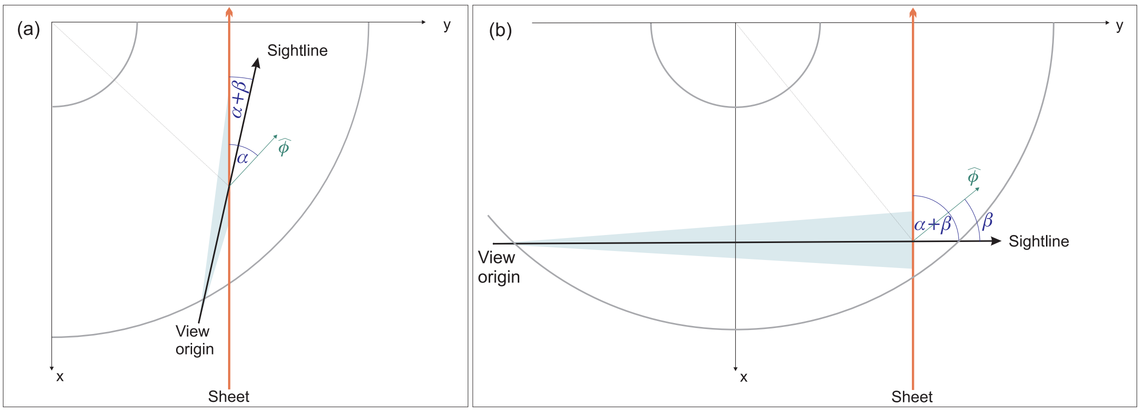

Figure 3.5: (a) The viewing position needed to reduce the numerator of the pitch angle equation to only posses a dominant B_ϕ term. **(b)** The viewing position needed to reduce the denominator of the pitch angle equation to only posses a dominant B_ϕ term.

an alternative method to self consistently determine the velocity profile, based on the Doppler shift of interference fringes. Due to the scope of this thesis, this technique will not be considered further.

3.4.2 Optimum viewing

As the general form of the pitch angle equation has two unknown values[1], B_R and B_Z, which appear in the numerator and denominator, in many cases it is not possible to manipulate the equation in order for information about these two terms to be extracted. In this section ways in which the approximate form of the pitch angle equation, Eq. 3.29, can be simplified through manipulation of the viewing geometry of the neutral beam are explored.

A desirable form of the approximate pitch angle equation, Eq. 3.29, is one in which the unknowns only appear in the numerator or denominator. In order to reduce the numerator such that it depends only on B_ϕ (known) requires the conditions

$$\cos\alpha \to 0 \quad \& \quad \theta \sin(\alpha+\beta) \to 0. \tag{3.32}$$

Which implies $\alpha \to \frac{\pi}{2}$ and $\alpha+\beta$ small.

When the relative sizes of the magnetic fields are considered, these conditions can be relaxed to produce the desired approximations by neglecting any terms which are very small compared to the dominant term, typically B_ϕ. As the neutral beams are injected in the midplane and only light up a small section of the plasma above and below, the radial component B_R of the poloidal magnetic field will be small compared to the vertical component B_Z. Also in general the toroidal magnetic field B_ϕ is an order of magnitude larger than the maximum poloidal magnetic field, hence for regions illuminated by a neutral beam injected on the midplane $B_\phi >> B_R$. The terms of interest can thus be compared to the size of the dominant B_ϕ term.

To reduce the form of the numerator, there will now be the weak condition that α must not be small, to insure the B_ϕ term is not negligible, and $\alpha+\beta$ be small. Such a viewing

[1]The true unknown value is the poloidal magnetic field. For circular flux surfaces there is a simple relationship between B_R and B_Z, but for shaped flux surfaces this relationship is not known if the shape parameters are unknown.

geometry manifests itself as the instrument looking at the section of the neutral beam near the outer region of the plasma and will be looking along the beam, such a setup is shown in Fig. 3.5 **(a)**. This viewing geometry corresponds to the typical viewing geometry for present discrete channel MSE systems. The corresponding approximate form of the pitch angle is

$$S \approx \frac{\sin\alpha B_\phi}{\xi(\sin\beta B_R + \cos\beta B_\phi) - \cos(\alpha+\beta)B_Z} \approx \frac{\sin\alpha B_\phi}{\xi\cos\beta B_\phi - \cos(\alpha+\beta)B_Z}, \tag{3.33}$$

where the radial magnetic field B_R has been neglected, as $\sin\beta$ and $\cos\beta$ are of similar size for such a viewing geometry.

Conversely, for the denominator to only depend on B_ϕ, the conditions are

$$\sin\beta \to 0 \quad \& \quad \cos(\alpha+\beta) \to 0. \tag{3.34}$$

In this case for the B_ϕ term to dominate in the denominator, there will be the weak condition for β to be small but a stronger dependence on $\alpha+\beta \to \pi/2$, in order to insure that the sizes of the B_ϕ and B_Z terms are not comparable. These conditions are met for a viewing geometry where the view is approximately perpendicular to the direction of the neutral beam and near the plasma edge to insure β is small, this viewing geometry is shown in Fig. 3.5 **(b)**. With this view perpendicular to the motion of the beam, the technical feasibility of the measurement is decreased due to negligible Doppler shifting of the Stark multiplet. The corresponding form of the approximate pitch angle equation is

$$S \approx \frac{\theta B_Z + \sin\alpha B_\phi}{\xi\cos\beta B_\phi}, \tag{3.35}$$

where the B_R term in the numerator has been neglected due to the fact that in general $B_\phi >> B_R$ and the simplification $\sin(\alpha+\beta) \approx 1$ has also been applied. As θ is small it is seen that for such a viewing geometry the magnetic pitch angle S is only weakly dependent on the vertical component of the poloidal magnetic field B_Z.

For these two viewing geometries considered the form of the equation may have been simplified, but they are not favorable as the sensitivity to B_R is negligible and B_Z is small, due to the dominant B_ϕ terms. Moreover, these approximations which reduce the form of the pitch angle equation may not be valid across the entire captured image.

As it is the poloidal magnetic field which is desired, it is logical to have a viewing geometry which minimises the effect of B_ϕ on the pitch angle. From Eq. 3.29 the conditions needed for B_ϕ to be minimised are

$$\sin\alpha \to 0 \quad \& \quad \cos\beta \to 0, \tag{3.36}$$

hence

$$\alpha \to 0 \quad \& \quad \beta \to -\frac{\pi}{2}. \tag{3.37}$$

For α to be zero requires that the viewed section of the neutral beam is in the centre region of the plasma, from this the instrument must be viewing perpendicular to the beam for $\beta \to -\pi/2$, as shown clearly in Fig. 3.6 **(a)**. This position where there is now dependence on B_ϕ corresponds to the position where the velocity of the beam is parallel to the toroidal magnetic field, conforming with the underlying equation $\mathbf{v} \times \mathbf{B}$.

However, such a view of the neutral beam manifests itself as a vertical cross section of the plasma. As it will be near the centre of the plasma, the poloidal magnetic field

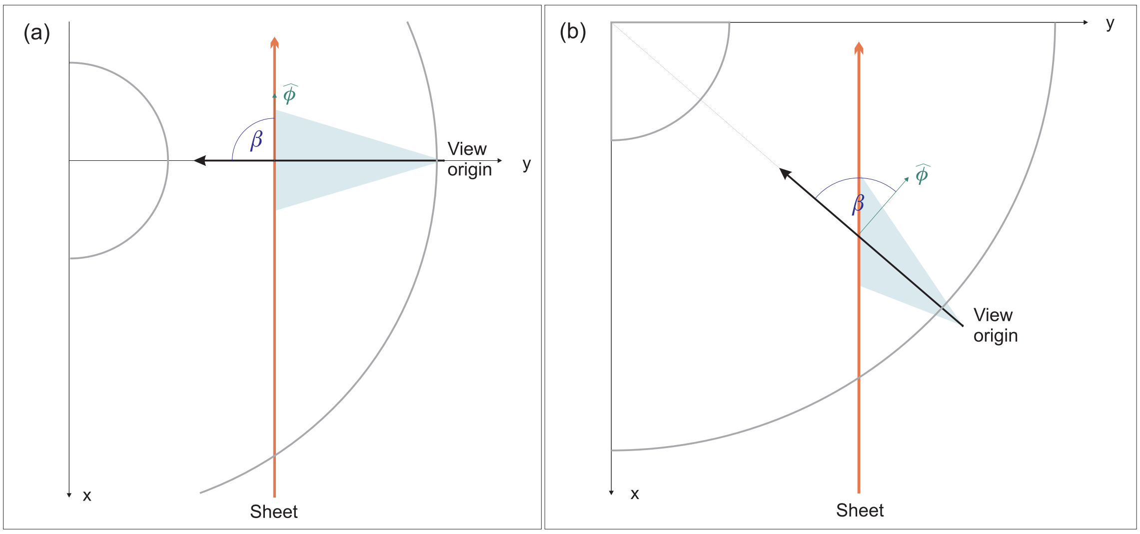

Figure 3.6: (a) The optimum view of the neutral beam which minimises the effect of the toroidal magnetic field B_ϕ on the magnetic pitch angle. **(b)** A feasible viewing arrangement which retains one of the constraints to minimise B_ϕ whilst viewing a radial profile of the plasma.

strengths will be small. Imaging of this area may not be feasible due to these small magnetic fields but more importantly due to the lack of signal, since the neutral beam is attenuated as it penetrates the plasma, and no observed Doppler shift os the Stark multiplet.

To image the radial profile of the magnetic field, $\beta \rightarrow -\pi/2$ can be retained but the condition for α can not be, as a different region of the neutral beam must be imaged. A setup which minimises B_ϕ and enables radial profile imaging is shown in Fig. 3.6 **(b)**. Such a radial view will suffer from line of sight integration effects decreasing the quality of the measurement, as it is looking "across" the magnetic surfaces.

With all of these considerations, the optimum viewing geometry for the 2D imaging system is that of Fig. 3.29 **(a)** looking "along" the magnetic surfaces. As the pitch angle equation has a desirable approximate form and due to the technical feasibility (large Doppler shift of the Stark multiplet). This view corresponds to the typical viewing geometries adopted by existing MSE systems.

3.4.3 Additional information captured?

The 2D system has the inherent possibility of simultaneously capturing poloidal magnetic field information over an area of the plasma. However, due to the the nature of the pitch angle equation and the relative magnetic fields strengths involved, the magnetic pitch angle is dominated by the toroidal field. In effect this results in the additional information which is captured by the 2D system is the spatial variation of the vertical magnetic component (B_Z) and the velocity profile of the neutral beam. The low sensitivity to the radial magnetic field component (B_R) is due to the fact that it lies in the same plane as B_ϕ.

By altering the view for the system the effect of the dominant B_ϕ term can be minimised. However, in these circumstances the view is looking "across" the magnetic surfaces and information on the unknown poloidal magnetic field is potentially lost due to line of sight integration effects. Technical considerations also indicate that a minimised B_ϕ view is not feasible, such as only a weak signal is expected as a result of the attenuation of the neutral beam into the plasma and little to no Doppler shifting of the MSE multiplet as the view is perpendicular to the beam.

As the new technique is a 2D imaging method, there are two main areas in which this system has major advantages over the existing discrete channel systems:

1. Much more amounts of data is collected. For example, the data in a small region above and below the horizontal plane captured with a 2D system can be averaged, to produce a 1D slice of the pitch angle with increased signal to noise ratio than the discrete 1D instruments. Applying the approximations for the pitch angle across the mid plane, a continuous radial profile of the vertical magnetic field B_Z can be estimated, which has the possibility to increase the accuracy of numerical equilibrium reconstruction codes.

2. Internal magnetic field structure information is captured. It is shown how it is possible to extract this information through manipulation of images in the following section.

So far only the existing neutral beam geometries have been considered, that is beams injected toroidally along the horizontal plane of the tokamak. In further upgrades on some tokamaks, namely DIII-D, off-axis neutral beam injection will be implemented [27]. Such injection will illuminate areas of the plasma in which the radial magnetic field component B_R will be stronger. As the pitch angle is the ratio of two terms, each dependent on the unknowns B_R and B_Z, very little can be done to extract information through analytic manipulation of the equation describing S. This implies that in order for information to be extracted from such a 2D image, it needs to be used as a basis from which a realistic parameterized model can be optimised.

3.5 Magnetic field structure and perturbation analysis

It is well known that instabilities within tokamaks have significant magnetic perturbation components. As these observed magnetic perturbations are often periodic, synchronous imaging techniques provide a possible method to measure such perturbations using the 2D MSE instrument. Synchronising the measurement of the pitch angle with the instability phase produces an image which captures the perturbed and DC magnetic fields. An image which has been taken with an exposure over many cycles of the perturbation without regard to synchronisation will produce an image of the DC magnetic field. Through the appropriate manipulation of these images it is possible to extract the perturbed magnetic field component. This section derives the equation which indicates how the appropriate synchronous and DC images should be manipulated.

As the pitch angle equation is a ratio of the magnetic field components, the pitch angle equation must be in a simple form where the unknown quantities appear in only the numerator or denominator in order for information on a magnetic perturbation to be easily extracted. The only view producing an approximate form for the pitch angle equation which satisfies this condition is one that looks “along” the neutral beam from the inboard side, such as the “standard” view illustrated in Fig. 3.29 **(a)**. The approximate form of the pitch angle equation for this view is

$$S = \tan\gamma \approx \frac{\sin\alpha B_\phi}{\xi\cos\beta B_\phi - \cos(\alpha+\beta)B_Z}, \tag{3.38}$$

where γ is the measured pitch angle.

The magnetic perturbation can be expressed as perturbations to the vertical and radial magnetic field components:

$$B_Z = B_{Z_0} + \tilde{B}_Z, \tag{3.39}$$
$$B_R = B_{R_0} + \tilde{B}_R, \tag{3.40}$$

where B_{x_0} is the initial component and $\tilde{B}_x$ is the perturbation.

For the view considered here, the radial component does not contribute significantly to the pitch angle equation. From this it can be assumed that for an image of the perturbed magnetic field the perturbed radial component will not contribute either. This assumption and the approximate form of the pitch angle equation will be validated in chapter 6.

Substituting this form for the vertical magnetic field into the reciprocal of the approximate pitch angle equation, Eq. 5.26, gives

$$\begin{aligned}\cot\tilde{\gamma} &= \frac{\xi\cos\beta B_\phi - \cos(\alpha+\beta)(B_{Z_0}+\tilde{B}_Z)}{\sin\alpha B_\phi}, \\ &= \cot\gamma_0 - \frac{\cos(\alpha+\beta)\tilde{B}_Z}{\sin\alpha B_\phi},\end{aligned} \tag{3.41}$$

where

$$\cot\gamma_0 = \frac{\xi\cos\beta B_\phi - \cos(\alpha+\beta)B_{Z_0}}{\sin\alpha B_\phi}, \tag{3.42}$$

represents the pitch angle map produced by the DC magnetic fields.

As the DC pitch angle map can be determined, the toroidal magnetic field B_ϕ is well known and the geometrical angles α, β are known across the field of view, manipulation of Eq. 3.41 allows the perturbed vertical magnetic field component to be estimated:

$$\tilde{B}_Z = \frac{\sin\alpha\ B_\phi\ (\cot\gamma_0 - \cot\tilde{\gamma})}{\cos(\alpha+\beta)}. \tag{3.43}$$

This result shows that the 2D MSE imaging system has the ability to resolve a perturbed magnetic field associated with a instability of the plasma. However, it must be shown that the approximate equation used to derive this result is valid over the field of view for the case of the unperturbed and perturbed magnetic field. In order to asses this, an accurate model to predict the internal magnetic fields of a tokamak is developed in the following chapters, which allows the validity of this method to be ascertained. For the determination of the magnetic fields, the natural coordinate system for the plasma has been adopted using a parameterized flux surface model, called the *Miller equilibrium* flux surface model, which is discussed in the next chapter.

Chapter 4

Miller Flux Surface Representation

The “natural” coordinate system for the computation of the physics of a magnetically confined plasma is the set of the nested magnetic flux surfaces, which confine the plasma and over which many plasma properties are constant. In a tokamak these flux surface co-ordinates are found by numerically solving the equation describing the plasma force-balance, the Grad-Shafranov equation. An analytical representation of a set of valid solutions to the Grad-Shafranov equation for the equilibrium magnetic flux surface geometry in tokamaks has been developed by Miller *et al* [28]. The Miller representation has become a powerful tool to help understand transportation and turbulence phenomena in shaped plasmas [29][30][31].

In this thesis, model 2D MSE images have been calculated by specifying functions of the poloidal flux using the Miller flux surface geometry. From Maxwell’s equations the magnetic field can then be found and the expected ideal MSE image calculated. This representation, involves a non-orthogonal curvilinear coordinate system which means that in order to determine the magnetic fields, a tensor analysis must be employed.

In an attempt to implement this model based on previously published material by Stacey [32], inconsistencies were found in the stated metrics for the Miller coordinate transformation. In this chapter a complete analysis of the Miller representation, in terms of a general non-orthogonal curvilinear coordinate system, has identified the inaccuracies in this published work. The revised metric tensors are derived and presented here. Following this, the differential expressions used for the modeling are given.

4.1 Curvilinear coordinate transformation

The model developed by Miller involves representing the nested magnetic flux surfaces in terms of a general non-orthogonal curvilinear coordinate system, described by variables (r, θ, ϕ). The variable r is defined as the half diameter of a flux surface along the midplane, see Fig. 4.1, θ as a “poloidal” like angle from the outer mid-plane with the positive direction towards the inner mid-plane and ϕ is the toroidal angle which is the same as the general toroidal angle. This “poloidal” like angle θ must not be thought of as equivalent to the usual poloidal angle θ.

The shape of the flux surfaces are determined by three parameters: $\kappa(r)$ which describes the elongation, $\delta(r)$ the triangularity and $R_0(r)$ which describes the Shafranov shift, which is the pressure induced outward displacement of the centre of the flux surface from the nominal “zero” pressure magnetic axis. As stated these parameters can be a function of the radius r, which allows variations in the flux surface shapes between the

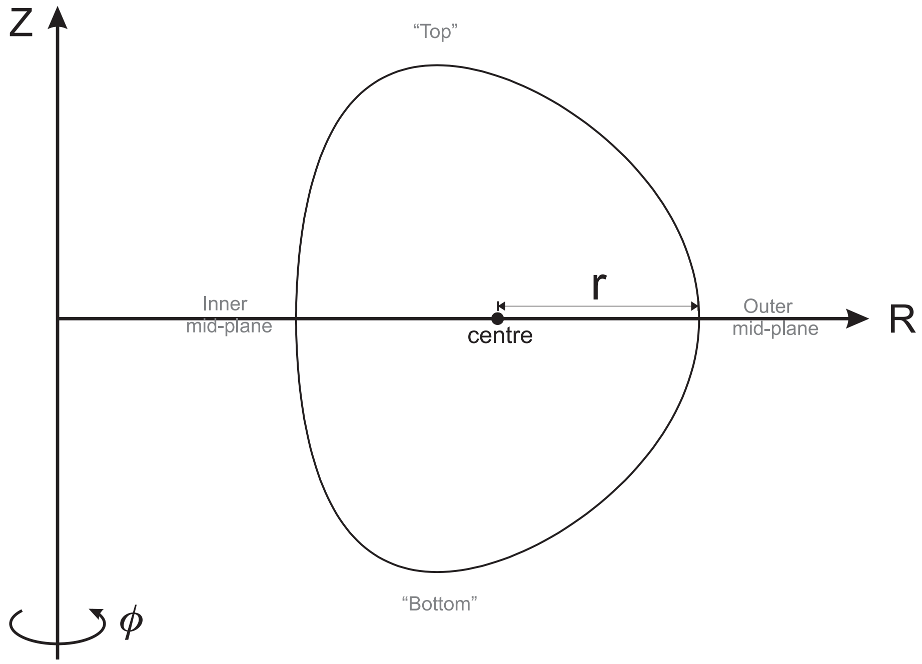

Figure 4.1: Representation of a "D" shaped magnetic flux surface of a tokamak, illustrating the half diameter r of the flux surface. Also regions of interest which will be used later in this chapter have been labeled.

centre and outer regions of the plasma. Figure 4.2 shows four flux surface sets to help the reader visualise the dependence on the parameters δ, κ and $R_0(r)$.

The transformation equations between this curvilinear coordinate system and the cylindrical coordinate system (R,Z, ϕ) of Fig. 4.1, are [28]

$$\begin{aligned} R(r,\theta) &= R_0(r) + r\cos[\theta + \chi\sin\theta], \\ Z(r,\theta) &= \kappa(r) r \sin\theta, \\ \phi &= \phi, \end{aligned} \tag{4.1}$$

where $\chi = \sin^{-1}\delta(r)$.

In this new curvilinear coordinate system a surface of constant poloidal magnetic flux, will now be refered to as a *flux surface*, is given by a coordinate curve for θ. (A coordinate curve is generated by varying one parameter whilst holding the two others constant, for example a θ coordinate curve is generated by holding r and ϕ constant and varying θ.)

A curvilinear coordinate system is determined to be orthogonal or non-orthogonal system depending on whether the coordinate curves are perpendicular everywhere. Figure 4.3 is a poloidal cross section which shows the coordinate curves for r and θ for a model "D" shaped plasma with no Shafranov shift. It is clear from this figure that the coordinate curves for r and θ are not perpendicular everywhere. Thus this Miller representation is a non-orthogonal curvilinear coordinate system. This is very important as 3D vector algebra and differentials in a non-orthogonal curvilinear coordinate system must be treated with a tensor analysis.

The fundamental relations concerning 3D vector algebra and calculus in the Miller coordinate system, or any other curvilinear coordinate system, must be derived from expressions based on the fundamental Cartesian coordinates. Hence the Miller transformation

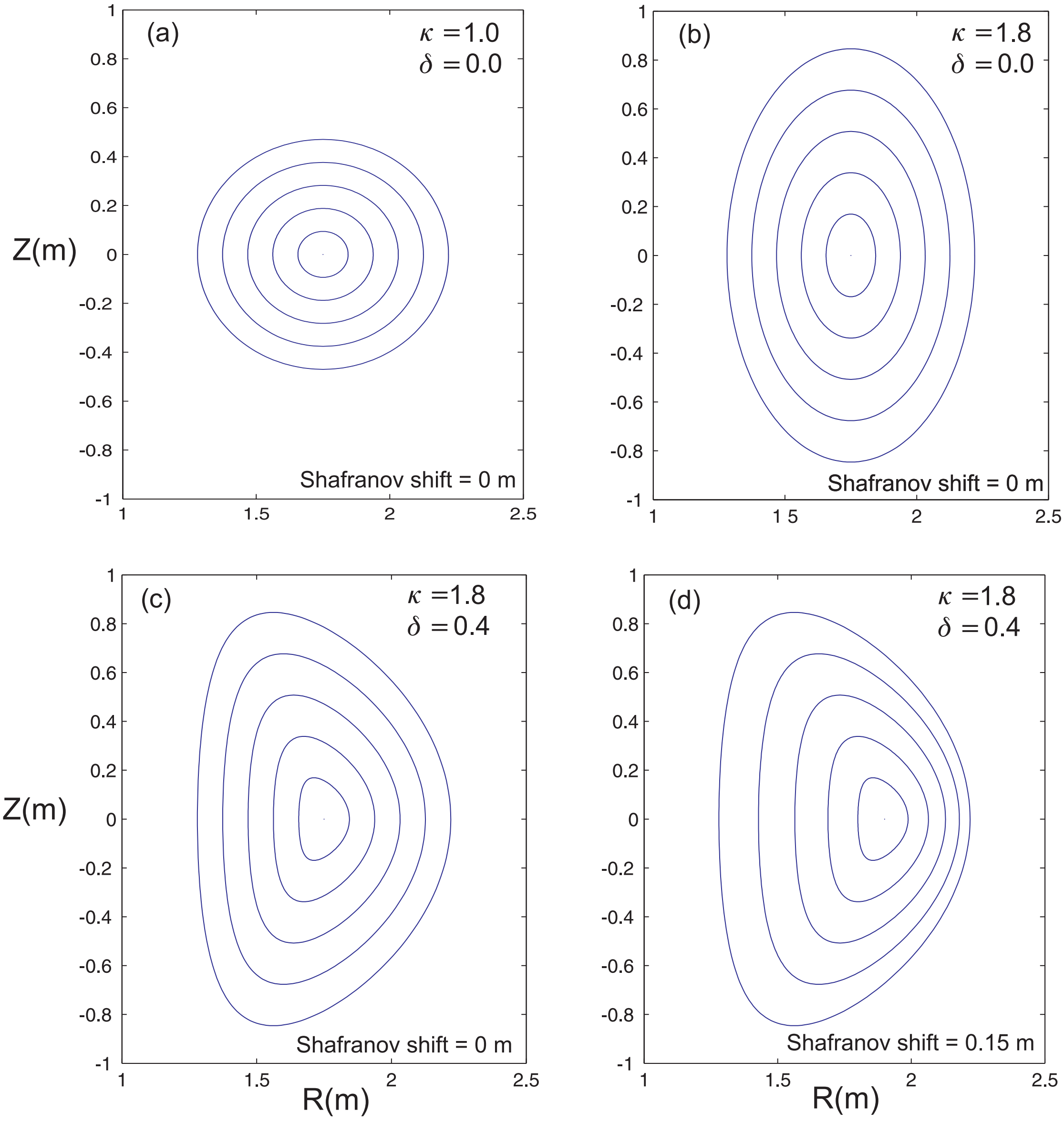

Figure 4.2: Poloidal cross section plots illustrating the effect of the Miller shape parameters; elongation κ, triangularity δ and Shafranov shift $R_0(r)$ on the shape of poloidal magnetic flux surfaces. This has been created based on a plasma with $R_{major} = 1.75$ m and $a = 0.5$ m, note only 5 surfaces have been shown for clarity with constant κ and δ values. (a) through to (c) have concentric flux surfaces with no Shafranov shift, while (d) has a magnetic axis displacement of 0.15 m with $R_0(r)$ having a quadratic dependence on r.

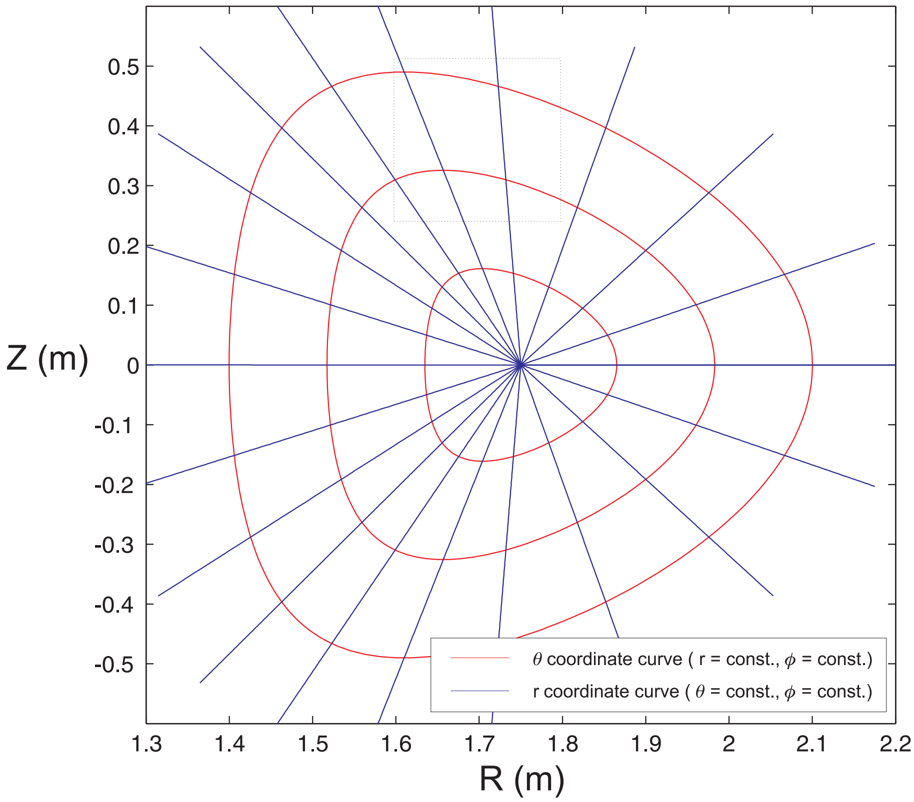

Figure 4.3: Coordinate curves for r and θ for an equilibrium with $\kappa = 1.4$, $\delta = 0.4$, no Shafranov shift and with no variation of the flux surface parameters between surfaces. The r coordinate curves plotted have an equal θ spacing between them which is $\Delta\theta = \pi/10$ and the θ coordinate curves have an equal spacing of $\Delta r = 0.11$ m. It is clear from this figure that the two coordinate curves do not intersect perpendicular everywhere, thus this is a non-orthogonal curvilinear coordinate system.

equations, Eq. 4.1, must be given in terms of a Cartesian coordinate system.

Now as it is a Euclidean space in which we work, the curvilinear transformation will be developed in terms of the Cartesian components (x, y, z) of a 3D vector $\mathbf{R}$ (not to be confused with the cylindrical coordinate R). In terms of the Miller representation coordinates (r, θ, ϕ) a general point $\mathbf{R}$ can be expressed as:

$$\begin{aligned} & x &=& \; R(r,\theta)\cos\phi = [R_0(r) + r\cos(\theta + \chi\sin\theta)]\cos\phi, \\ \mathbf{R}(r,\theta,\phi) : & y &=& \; R(r,\theta)\sin(\phi) = [R_0(r) + r\cos(\theta + \chi\sin\theta)]\sin\phi, \\ & z &=& \; Z(r,\theta) = \kappa(r) r\sin\theta, \end{aligned} \tag{4.2}$$

4.1.1 Derivatives of the transformation equations

In later sections the various derivatives of the transformation equations will be used extensively. As these can be quite lengthy expressions, the form of the key derivatives will be stated here and the short hand expressions used later.

Explicitly, the derivatives of the vector $\mathbf{R}$ with respect to the coordinates r, θ and ϕ will be needed. Using the chain rule the derivatives of a component of the position vector $\mathbf{R}$

can be written in terms of the derivative of the transformation equations $R(r,\theta)$ or $Z(r,\theta)$. Hence it is only necessary to specify the derivatives of the transformation equations $R(r,\theta)$ and $Z(r,\theta)$ with respect to r and θ.

The derivatives needed are

$$\partial_r R \equiv \frac{\partial R}{\partial r} = \partial_r R_0 + \cos(\theta + \chi\sin\theta) - s_\delta \sin\theta\sin(\theta+\chi\sin\theta), \tag{4.3}$$

$$\partial_r R \equiv \frac{\partial R}{\partial \theta} = -r(1+\chi\cos\theta)\sin(\theta+\chi\sin\theta), \tag{4.4}$$

$$\partial_r R \equiv \frac{\partial Z}{\partial r} = \kappa\sin\theta(1+s_\kappa), \tag{4.5}$$

$$\partial_r R \equiv \frac{\partial Z}{\partial \theta} = r\kappa\cos\theta, \tag{4.6}$$

where

$$s_\delta = \frac{r\partial_r\delta}{\sqrt{1-\delta^2}}, \tag{4.7}$$

$$s_\kappa = \frac{r\partial_r\kappa}{\kappa}. \tag{4.8}$$

4.2 Basis vectors

4.2.1 Tangent-basis vector

For notational ease, the vector $\mathbf{R}$ will be written in terms of general parameters u^1, u^2 and u^3, that is $\mathbf{R}(u^1,u^2,u^3)$, with the identification $u^1 \equiv r, u^2 \equiv \theta$ and $u^3 \equiv \phi$.

A *basis* for 3D space is meant any set of three linearly independent vectors $\mathbf{e}_1, \mathbf{e}_2$ and $\mathbf{e}_3$. In a general coordinate system the basis vectors $\mathbf{e}_1, \mathbf{e}_2$ and $\mathbf{e}_3$ at a point P, determined by the position vector $\mathbf{R}$, are defined to be the tangent vectors of the coordinate curves at the point P [33].

Simple differential geometry considerations show that $\partial\mathbf{R}/\partial u^i$ is a tangent vector of the u^i-coordinate curve [34]. The tangent-basis vectors for the Miller coordinate system are then written as

$$\mathbf{e}_r = \frac{\partial\mathbf{R}}{\partial r}, \qquad \mathbf{e}_\theta = \frac{\partial\mathbf{R}}{\partial\theta}, \qquad \mathbf{e}_\phi = \frac{\partial\mathbf{R}}{\partial\phi}. \tag{4.9}$$

The form of these tangent basis vectors are not given explicitly here, but can easily be found through the chain rule and the derivatives presented above.

These basis vectors are said to be local, as they vary from point to point. In general they are neither of unit length nor dimensionless, since for example $\partial\mathbf{R}/\partial\theta$ has unit of length. Referring to Fig. 4.3, which has coordinate curves plotted with equal spacing, it can be seen that the arc length between any two successive coordinate curves varies around a flux surface, hence the value for $\partial\mathbf{R}/\partial\theta$ will vary from point to point. Nevertheless, one can define a unit tangent vector through the obvious prescription

$$\hat{\mathbf{e}}_i \equiv \frac{\mathbf{e}_i}{|\mathbf{e}_i|} = \frac{\partial\mathbf{R}}{\partial u^i}\Bigg/\left|\frac{\partial\mathbf{R}}{\partial u^i}\right|. \tag{4.10}$$

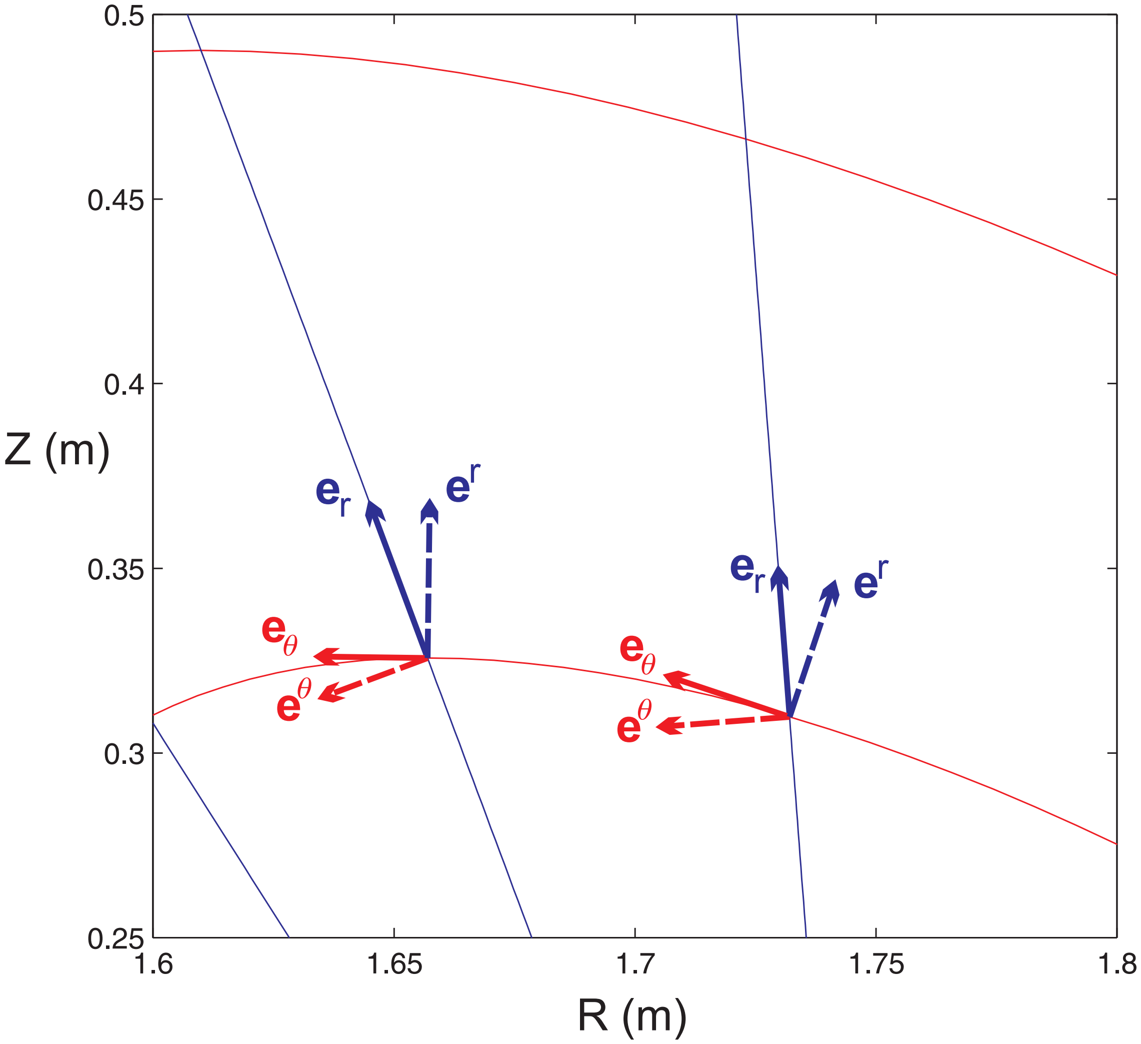

Figure 4.4: An enlarged section of Fig. 4.3 (indicated by the dotted box) which shows the basis vectors at two point of intersection for the Miller curvilinear coordinate system. The basis vectors $\mathbf{e}_r$ and $\mathbf{e}_\theta$ are tangent vectors of the coordinate curves and the reciprocal basis vectors $\mathbf{e}^r$ and $\mathbf{e}^\theta$ are perpendicular to the coordinate surfaces. It should be noticed that the angle between the basis vectors $\mathbf{e}_r$ and $\mathbf{e}_\theta$ will vary around a given flux surface, hence when certain operations are done in this basis one must account for the variation in the basis vectors. Note that when the shape parameters describing the flux surface geometry change, so do the basis vectors.

4.2.2 Reciprocal-basis vector

The gradient of the coordinate u^i, ∇u^i, is defined such that the differential du^i is given by

$$du^i = \nabla u^i \cdot d\mathbf{R}. \tag{4.11}$$

Applying the chain rule, the differential $d\mathbf{R}$ is given by

$$d\mathbf{R} = \sum_{j=1}^{3} \frac{\partial \mathbf{R}}{\partial u^j} du^j = \frac{\partial \mathbf{R}}{\partial u^j} du^j \equiv \mathbf{e}_j du^j, \tag{4.12}$$

where the general definition of $\mathbf{e}_j$ from Eq. 4.9 has been used and in the final two forms the summation convention has been adopted. In this convention if a letter is used as a subscript and also as a superscript on the same side of the equation, then that side of the equation should be summed over all values of that index.

Substituting the form of $d\mathbf{R}$ from Eq. 4.12 into Eq. 4.11 leads to

$$du^i = \nabla u^i \cdot \mathbf{e}_j du^j, \tag{4.13}$$

which holds if and only if

$$\nabla u^i \cdot \mathbf{e}_j = \delta^i_j, \tag{4.14}$$

where δ^i_j is the Kronecker delta function.

This relationship states that the set of vectors ∇u^i and $\mathbf{e}_j$ form reciprocal sets of vectors. Therefore, the set ∇u^i is defined as the *reciprocal-basis vectors* $\mathbf{e}^i$, and Eq. 4.14 now reads

$$\mathbf{e}^i \cdot \mathbf{e}_j = \delta^i_j. \tag{4.15}$$

The unit reciprocal-basis vector is given by[33]

$$\hat{\mathbf{e}}^i = \mathbf{e}^i |\mathbf{e}^i|. \tag{4.16}$$

For the Miller representation the reciprocal-basis vectors are

$$\mathbf{e}^r = \nabla r, \qquad \mathbf{e}^\theta = \nabla \theta, \qquad \mathbf{e}^\phi = \nabla \phi. \tag{4.17}$$

These reciprocal-basis vectors $\mathbf{e}^i$ are perpendicular to the coordinate surfaces $u^i = c^i$, where a coordinate surface is defined as the surface created by holding one variable constant, the variable which is held constant specifies which coordinate surface it is. Like the tangent-basis vectors, the length of the reciprocal basis vectors is not necessarily constant.

The reciprocal-basis vectors $\mathbf{e}^r$ and $\mathbf{e}^\theta$ are shown in Fig. 4.4 at two positions. As this figure is a poloidal cross section of the tokamak, by definition the toroidal basis vector $\mathbf{e}_\phi$ is perpendicular to the $R - Z$ plane everywhere (normal to the page). Therefore the coordinate curves also represent a section of the coordinate surfaces, that is the coordinate curve for r also is a slice of the coordinate surface for θ.

4.3 Vector representation in a curvilinear coordinate system

In general any vector can be represented as a linear combination of either the tangent- or reciprocal-basis vectors. For an orthogonal coordinate system, e.g. Cartesian, the tangent- and reciprocal-basis vectors are equivalent, hence there is only one representation for a vector. But for a non-orthogonal curvilinear coordinate system, there are two representations. Any vector $\mathbf{D}$ can be written as[34]

$$\mathbf{D} = (\mathbf{D}\cdot\mathbf{e}_r)\mathbf{e}^r + (\mathbf{D}\cdot\mathbf{e}_\theta)\mathbf{e}^\theta + (\mathbf{D}\cdot\mathbf{e}_\phi)\mathbf{e}^\phi, \tag{4.18}$$

or

$$\mathbf{D} = (\mathbf{D}\cdot\mathbf{e}^r)\mathbf{e}_r + (\mathbf{D}\cdot\mathbf{e}^\theta)\mathbf{e}_\theta + (\mathbf{D}\cdot\mathbf{e}^\phi)\mathbf{e}_\phi. \tag{4.19}$$

In summary for the general case

$$\mathbf{D} = D_i\mathbf{e}^i \quad \text{with} \quad D_i \equiv \mathbf{D}\cdot\mathbf{e}_i, \tag{4.20}$$
$$\mathbf{D} = D^i\mathbf{e}_i \quad \text{with} \quad D^i \equiv \mathbf{D}\cdot\mathbf{e}^i, \tag{4.21}$$

where the summation convention over the indices is implied. The coefficients D_i are called the *covariant components* of the vector $\mathbf{D}$ while D^i are called the *contravariant components* of the vector $\mathbf{D}$. This follows the convention for naming the components of a vector

$$\begin{aligned} \text{covariant} &\equiv \text{subscripts} \equiv (\quad)_i, \\ \text{contravariant} &\equiv \text{superscripts} \equiv (\quad)^i. \end{aligned} \tag{4.22}$$

These vector components are given the name covariant and contravariant due to their transformation properties between coordinate systems, see Sokolnikoff [35] pages (57-62).

4.4 The metric coefficients g_{ij} and g^{ij}

The metric coefficients g_{ij} and g^{ij} describe the fundamental geometric characteristics of a general curvilinear coordinate system. They determine the differential arc length along a curve, allow covariant and contravariant components of a vector to be converted from one to the other plus allow the means to calculate the dot and cross product of two vectors.

These metric coefficients can be obtained using the fact that an arc length ds is an invariant. We consider the arc length ds between two infinitely close points with the vector $d\mathbf{r}$ joining the two points, having covariant components du_i and contravariant components du^i. Then [33]

$$ds^2 = |d\mathbf{r}|^2 = d\mathbf{r}\cdot d\mathbf{r} = du^i\mathbf{e}_i \cdot du^j\mathbf{e}_j = du_i\mathbf{e}^i \cdot du_j\mathbf{e}^j, \tag{4.23}$$

This equation allows us to introduce the metric coefficients

$$\begin{aligned} ds^2 &= g_{ij}du^i du^j, \\ ds^2 &= g^{ij}du_i du_j. \end{aligned} \tag{4.24}$$

with g_{ij} defined as the dot product of the tangent-basis vectors

$$g_{ij} = \mathbf{e}_i\cdot\mathbf{e}_j = \frac{\partial\mathbf{R}}{\partial u^i}\cdot\frac{\partial\mathbf{R}}{\partial u^j}, \tag{4.25}$$

and g^{ij} defined as the dot product of the reciprocal-basis vectors

$$g^{ij} = \mathbf{e}^i \cdot \mathbf{e}^j = \nabla u^i \cdot \nabla u^j. \tag{4.26}$$

The set of functions g_{ij} and g^{ij} represent symmetric tensors, called the covariant and contravariant metric tensors respectively. The naming of these tensors follows from the adopted notation convention stated in Eq. 4.22. The diagonal components of the covariant metric tensor are often represented by

$$h_i = \sqrt{g_{ii}}. \tag{4.27}$$

These components are often called the metrics as orthogonal coordinate systems only have these diagonal components of the metric tensor which are non-zero. For example the metrics for a cylindrical coordinate system are $h_r = 1, h_\theta = r$ and $h_z = 1$.

Using these metric coefficients it is then trivial to convert between co- and contravariant vector components. Substituting the definition of the covariant metric coefficient from Eq. 4.25 into the definition of the covariant component of a vector, Eq. 4.21 and using the symmetry property of g_{ij}, it is found

$$D_i = \mathbf{D} \cdot \mathbf{e}_i = D^j \mathbf{e}_j \cdot \mathbf{e}_i = D^j g_{ji} = g_{ij} D^j, \tag{4.28}$$

similarly for the contravariant components

$$D^k = \mathbf{D} \cdot \mathbf{e}^k = D_i \mathbf{e}^i \cdot \mathbf{e}^k = D_i g^{ik} = g^{ki} D_i. \tag{4.29}$$

Analogous expressions hold for the covariant and contravariant basis vectors

$$\mathbf{e}_i = (\mathbf{e}_i \cdot \mathbf{e}_j)\mathbf{e}^j = g_{ij}\mathbf{e}^j, \tag{4.30}$$
$$\mathbf{e}^i = (\mathbf{e}^i \cdot \mathbf{e}^j)\mathbf{e}_j = g^{ij}\mathbf{e}_j. \tag{4.31}$$

Taking the dot product of a tangent- and reciprocal-basis vector, yields a relationship between the two metric tensors and the Kronecker delta function:

$$\mathbf{e}_i \cdot \mathbf{e}_j = g_{ij}\mathbf{e}^j \cdot \mathbf{e}^k. \tag{4.32}$$

Using the relation in Eq. 4.15, it is found

$$\delta_i^k = g_{ij} g^{jk}. \tag{4.33}$$

4.4.1 Metric tensors for the Miller representation

Through the formalism developed in the previous sections, the covariant and contravariant metric tensors for the Miller representation can be easily determined. These will be used in the numerical simulations in later chapters.

The covariant metric tensor for the Miller representation is

$$g_{ij} = \begin{pmatrix} g_{rr} & g_{r\theta} & 0 \\ g_{r\theta} & g_{\theta\theta} & 0 \\ 0 & 0 & g_{\phi\phi} \end{pmatrix}, \tag{4.34}$$

where

$$g_{rr} = \left(\frac{\partial R}{\partial r}\right)^2 + \left(\frac{\partial Z}{\partial r}\right)^2, \tag{4.35}$$

$$g_{\theta\theta} = \left(\frac{\partial R}{\partial \theta}\right)^2 + \left(\frac{\partial Z}{\partial \theta}\right)^2, \tag{4.36}$$

$$g_{r\theta} = \frac{\partial R}{\partial r}\frac{\partial R}{\partial \theta} + \frac{\partial Z}{\partial r}\frac{\partial Z}{\partial \theta}, \tag{4.37}$$

$$g_{\phi\phi} = R^2. \tag{4.38}$$

The contravariant metric tensor is calculated by finding the inverse of the g_{ij} matrix of Eq. 4.34, using the relation $g_{ij}g^{jk} = \delta_i^k$ of Eq. 4.33. The form of g^{ij}, is found to be

$$g^{ij} \equiv \begin{pmatrix} (\nabla r)^2 & \nabla r \cdot \nabla \theta & 0 \\ \nabla r \cdot \nabla \theta & (\nabla \theta)^2 & 0 \\ 0 & 0 & (\nabla \phi)^2 \end{pmatrix}, \tag{4.39}$$

$$= \frac{1}{G}\begin{pmatrix} g_{\theta\theta}g_{\phi\phi} & g_{r\theta}g_{\phi\phi} & 0 \\ g_{r\theta}g_{\phi\phi} & g_{rr}g_{\phi\phi} & 0 \\ 0 & 0 & g_{rr}g_{\theta\theta} - g_{r\theta}^2 \end{pmatrix}, \tag{4.40}$$

$$\tag{4.41}$$

where $G = \det(g_{ij})$, which can be shown to be

$$G = R^2\left(\frac{\partial R}{\partial r}\frac{\partial Z}{\partial \theta} - \frac{\partial R}{\partial \theta}\frac{\partial Z}{\partial r}\right)^2. \tag{4.42}$$

The final form of the co- and contravariant metric tensors can easily be found by substituting the derivatives of the transformation equations $R(r, \theta)$ and $Z(r, \theta)$ from Eqs. (4.3-4.6).

4.5 Incorrect metrics reported in literature

Incorrect metrics and have been found in recent literature by W. Stacey [31][32][36][37]. In one paper[31], Stacey has stated that the Miller flux surface coordinate system is an orthogonal basis and then proceeded to state the diagonal metrics h_r, h_θ and h_ϕ without derivation as:

$$h_r = \frac{1}{|\nabla r|}, \tag{4.43}$$

$$h_\theta = r\sqrt{\cos^2(\theta + \chi\sin\theta) + \kappa^2\sin^2\theta}, \tag{4.44}$$

$$h_\phi = R_0 + r\cos(\theta + \chi\sin\theta), \tag{4.45}$$

where

$$|\nabla r| = \frac{\kappa^{-1}[\sin^2(\theta + \chi\sin\theta)(1 + \chi\cos\theta)^2 + \kappa^2\cos^2\theta]^{1/2}}{\cos(\chi\sin\theta) + \partial_r R_0\cos\theta + [s_\kappa - s_\delta\cos\theta + (1 + s_\kappa)\chi\cos\theta]\sin\theta\sin(\theta + \chi\sin\theta)}. \tag{4.46}$$

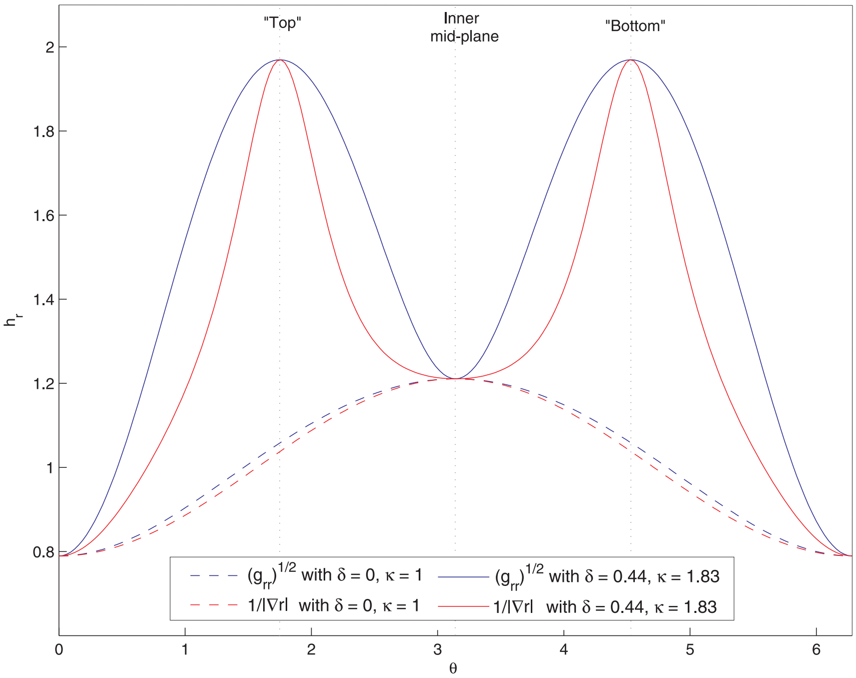

Figure 4.5: Comparisons of the metric coefficients h_r as stated by Stacey (red), given by $1/|\nabla r|$, and that as calculated from first principles (blue), $\sqrt{g_{rr}}$, as a function of θ. These metrics have been plotted for two flux surface shapes; the dashed lines correspond to circular flux surfaces with a Shafranov shift $R_0(r) \propto r^2$ and the magnetic axis displaced by $\sim a/5$, the full lines are for a "D" shaped plasma with the same Shafranov shift. The shaping parameters used are given in the legend.

The correct form for these metrics, given by $\sqrt{g_{rr}}$, $\sqrt{g_{\theta\theta}}$ and $\sqrt{g_{\phi\phi}}$, written out in full is

$$h_r = \sqrt{[\partial_r R_0 + \cos(\theta + \chi\sin\theta) - s_\delta \sin\theta \sin(\theta + \chi\sin\theta)]^2 + \kappa^2 \sin^2\theta (1 + s_\kappa)^2}, \tag{4.47}$$

$$h_\theta = r\sqrt{(1 + x\cos\theta)^2 \sin^2(\theta + \chi\sin\theta) + \kappa^2\cos^2\theta}, \tag{4.48}$$

$$h_\phi = R_0 + r\cos(\theta + \chi\sin\theta). \tag{4.49}$$

The form for $|\nabla r|$, Eq. 4.46, stated in Stacey's papers, agrees with the contravariant metric coefficient $\sqrt{g^{rr}} = |\nabla r|$ when calculated from first principles. If the coordinate system was orthogonal with this form of $|\nabla r|$, then $h_r = 1/|\nabla r|$ would be valid through the relation $\delta_i^k = g_{ij}g^{jk}$. However, as it is in fact a non-orthogonal coordinate system there are non-zero off-diagonal metric components. When the summation over all indices is carried out, a relation for the covariant metric g_{rr} can be found as

$$g_{rr} = \frac{1 - g_{r\theta}g^{r\theta}}{g^{rr}}. \tag{4.50}$$

It has been verified that the covariant metric component g_{rr} given by this formula and that of the direct formula, Eq. 4.35, are in fact equivalent. Figure 4.5 shows the metric h_r as given by Stacey, Eq. 4.43, plotted against the form derived from first principles for a non-orthogonal coordinate system as given by Eq. 4.47. The two metrics have been

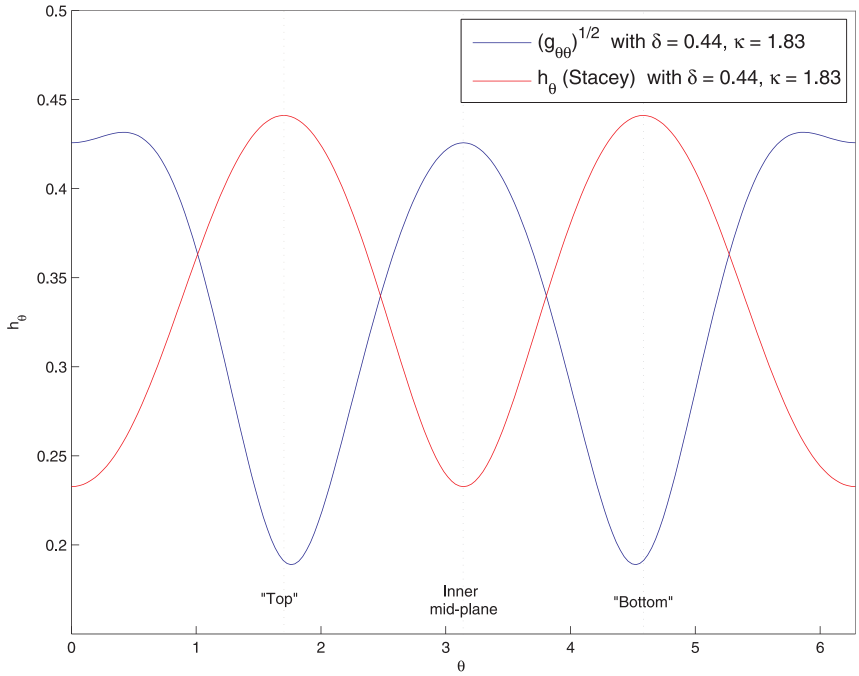

Figure 4.6: Comparison of the metric coefficient h_θ as stated by Stacey (red), Eq. 4.44, and that as calculated from first principles (blue), $\sqrt{g_{rr}}$, as a function of θ. These metrics have been plotted for "D" shaped flux surfaces with a Shafranov shift $R_0(r) \propto r^2$ and the magnetic axis displaced by $\sim a/5$. The shaping parameters used are given in the legend.

plotted for two flux surface shapes; one for Shafranov shifted circular surfaces (as given by dashed lines) and a second for "D" shaped flux surfaces with the same Shafranov shift. The form of the Shafranov shift used has $R_0(r)$ quadratic in r, with the magnetic axis displaced by $\sim a/5$ (where a is the minor radius of the plasma).

The author states in [36][37] that the poloidal arc length for the Miller representation is

$$dl_\theta = r\sqrt{\cos^2(\theta + \chi\sin\theta) + \kappa^2\sin^2\theta}\; d\theta. \tag{4.51}$$

In this Miller representation the "radius" r^* from the centre of a flux surface to the surface itself is given by

$$r^* = \sqrt{(R(r,\theta) - R_0(r))^2 + Z(r,\theta)^2} = r\sqrt{\cos^2(\theta + \chi\sin\theta) + \kappa^2\sin^2\theta}\,. \tag{4.52}$$

It follows that if the Miller coordinate system is equated to a cylindrical coordinate system, which has surfaces at radius r and arc length $dl_\theta = h_\theta d\theta = r d\theta$, one could arrive at the same poloidal arc length as stated by Stacey. However, the coordinate θ in the Miller representation must not be confused with the everyday "poloidal" angle "θ" which is used in the cylindrical coordinate system. This metric h_θ given by Miller does not intuitively make sense, the arc length for an angle $d\theta$ at the mid plane is greater than an arc length with the same angle $d\theta$ at the "top" of a shaped flux surface, as can be seen from Fig 4.3.

Figure 4.6 shows the correct form of h_θ, given by Eq. 4.48, plotted against the form of h_θ given by Stacey, Eq. 4.44, for the same "D" shaped flux surfaces as the h_r metric plot, Fig. 4.5. This figure shows a dramatic discrepancy between the two metric components.

The main use of the metric coefficients in the Stacey's work is for calculations of scrape-off layer flows. However, much off the work presented is fundamentally flawed as many of the calculations involve the metric coefficient h_θ, which has the largest discrepancy. Also in one paper in which he derives the representation of the plasma fluid equations in "Miller equilibrium" analytical flux surface geometry [32], all the differential operators, which define the fluid equations, are for orthogonal coordinate systems. Thus, no off-diagonal terms in the derivatives are considered. Some of the correct operators are given in the following section.

4.6 Vector relations and differentials

The vector relations and differentials needed for the simulations produced in this thesis, will be stated here in the general form for a non-orthogonal coordinate system. For the complete derivation of the relations given in this section the reader is referred to [33] and [34].

4.6.1 The dot and cross-product

The dot product of two vectors, **A** and **B**, in general curvilinear coordinates is

$$\mathbf{A}\cdot\mathbf{B} = A^i B_i = A_i B^i = g_{ij} A^i B^j = g^{ij} A_i B_j. \tag{4.53}$$

The cross-product is given by

$$\begin{aligned} \mathbf{A}\times\mathbf{B} &= \frac{1}{\sqrt{G}}\sum_k (A_i B_j - A_j B_i)\mathbf{e}_k, \qquad i,j,k \quad \text{cycle} \quad 1,2,3, \\ &= \frac{1}{\sqrt{G}}[(A_r B_\theta - A_\theta B_r)\mathbf{e}_\phi + (A_\phi B_r - A_r B_\phi)\mathbf{e}_\theta + (A_\theta B_\phi - A_\phi B_\theta)\mathbf{e}_r], \end{aligned} \tag{4.54}$$

where $G = \det(g_{ij})$ and the summation is over the cycling of the indices, which has been written out in full for the Miller representation.

4.6.2 Differential elements

The differential arc length along a coordinate curve u^i, which is denoted by $dl(i)$, is

$$dl(i) = \sqrt{g_{ii}}\, du^i = h_i du^i. \tag{4.55}$$

The differential element of area in the coordinate surface u^i, which is denoted $dS(i)$, is

$$dS(i) = \sqrt{g_{jj} g_{kk} - g_{jk}^2}\, du^j du^k. \tag{4.56}$$

The volume element d^3R is

$$d^3R = \sqrt{G}\, dU^i du^j du^k. \tag{4.57}$$

4.6.3 Operations involving ∇

The gradient of a scalar function $\Phi(u^i, u^j, u^k)$ is

$$\nabla\Phi = \frac{\partial\Phi}{\partial u^i}\mathbf{e}^i. \tag{4.58}$$

The divergence of a vector $\mathbf{A}$ is

$$\nabla \cdot \mathbf{A} = \frac{1}{\sqrt{g}} \frac{\partial}{\partial u^i} (\sqrt{g}\, A^i). \tag{4.59}$$

The curl of a vector $\mathbf{A}$ is

$$\nabla \times \mathbf{A} = \frac{1}{\sqrt{G}} \sum_k \left(\frac{\partial A_j}{\partial u^i} - \frac{\partial A_i}{\partial u^j} \right) \mathbf{e}_k \qquad i, j, k \quad \text{cycle} \quad 1, 2, 3, \tag{4.60}$$

where the same summation as the cross-product appears.

Chapter 5

Modelling of MSE polarization images

For accurate modeling of the 2D MSE imaging system, the internal magnetic components of the tokamak need to be expressed in the cylindrical basis (R, Z, ϕ). The poloidal magnetic field is produced by the toroidal plasma current which generally is comprised of inductive, externally driven and self-consistent components. Due to the toroidal bending of the plasma current distribution, the determination of the poloidal magnetic field is not straight forward. Whereas, the toroidal magnetic field component B_ϕ is well known as it is produced by external current carrying coils.

In this chapter, a method has been developed to determine the poloidal magnetic fields from a prescribed poloidal flux function ψ. The Miller equilibrium flux surface representation has been adopted here to provide the coordinates in which ψ is defined. This method has been developed such that the equilibrium conditions for the plasma are automatically satisfied. Through the use of this method the MSE pitch angle maps for a given viewing geometry of a neutral beam can be properly modelled. Further, as a first approximation, this can be used to model certain plasma instabilities which have a strong magnetic perturbation component, such as the sawtooth instability. This then allows the validity of the approximate form of the pitch angle equation to be ascertained, which is crucial if the method for extracting an image of the perturbed magnetic field from a DC and synchronous pitch angle image (as explained in chapter 3) is to be viable. A brief discussion on the technical feasibility of such a method follows.

The model parameters used here will be that of TEXTOR (a tokamak in Germany). The reasons for this choice are: (i) have encouraging results from previous implementation of the instrument on this tokamak, (ii) the neutral beam view achieved meets the requirements needed for imaging magnetic field structure and (iii) the system is returning in 2010 for further measurements. In addition, TEXTOR is a world leader in producing controlled MHD instabilities and produces plasmas with circular shifted, nested flux surfaces, which reduces the complexity of the image interpretation. Nevertheless, the model developed retains sufficient generality so that it can also be applied to "D"-shaped plasmas.

The calculations reported here have been made using the viewing geometry and plasma parameters which were obtained in the previous experimental program at TEXTOR (March 2009).

5.1 A representation for the poloidal magnetic field

The polarization direction of the emission from the neutral beams is determined by the induced electric field $\mathbf{E} = \mathbf{v} \times \mathbf{B}$, which is dependent on the direction of the total magnetic field and the injected beam velocity. The total magnetic field within a tokamak can be separated into two components: a toroidal component, around the torus, and a poloidal component, which lies in a plane which has its normal to the toroidal direction. The total magnetic field is written

$$\mathbf{B} = \mathbf{B}_{toroidal} + \mathbf{B}_{poloidal}. \tag{5.1}$$

The toroidal component of the magnetic field is well known and can be considered to be constant throughout a discharge. It is generated by feedback-controlled external current carrying toroidal solenoidal coils, producing a field on axis in the order of 2 T. In order to perturb this field by a significant amount a very large poloidal plasma current would be necessary. Since this does not occur in practice, for this thesis it will be assumed that the toroidal field, which varies as $1/R$, is unchanging and well known.

The poloidal magnetic field is produced by a toroidal plasma current. Intuitively it may be thought that it would be easiest to calculate the magnetic field from a parameterised toroidal current density by applying Ampère's law, $\oint \mathbf{B} \cdot d\mathbf{l} = \mu_0 \int_S \mathbf{j} \cdot \mathbf{n}\ da$. As the tokamaks of today do not have large aspect ratios (the ratio of the major axis to the average plasma radius R_{major}/a), the toroidal bending of the current distribution must be taken into account. The poloidal magnetic field will thus be stronger on the inboard side, closest to the tokamak axis, than the outer, producing a poloidal magnetic field which has a dependence on the poloidal angle θ. This poloidal variation makes Ampère's law unable to be solved simply. However, a method for determining the poloidal magnetic field can be obtained from a consideration of the topology of the magnetic field lines within the tokamak and the conditions for equilibrium.

For axisymmetric equilibria the magnetic field lines lie in nested toroidal magnetic surfaces [38]. The surfaces can be labeled by a number of different quantities, here they will be labelled according to the poloidal magnetic flux ψ lying within each surface.

The basic condition for equilibrium is that the nett force on the plasma be zero at all points. This requires that the force due to the plasma pressure balances the magnetic force [2], that is

$$\mathbf{j} \times \mathbf{B} = \nabla p. \tag{5.2}$$

It is clear from this equation that there can be no pressure gradient along the magnetic field lines and hence the magnetic surfaces, as $\mathbf{B} \cdot \nabla p = 0$. Therefore these surfaces are isobars. As these surfaces are of constant ψ, force balance implies that the pressure p is a function of ψ, and hence

$$\mathbf{B} \cdot \nabla \psi = 0. \tag{5.3}$$

Thus the magnetic field must also be a flux function. As the magnetic field must also be divergence free ($\nabla \cdot \mathbf{B} = 0$), it can be shown that for axially-symmetric equilibrium the poloidal flux function ψ is related to the toroidal vector potential A_ϕ (see Appendix A).

The poloidal magnetic field in the Miller representation is given by

$$\mathbf{B}_{poloidal} = B^r \mathbf{e}_r + B^\theta \mathbf{e}_\theta. \tag{5.4}$$

where B^r is the radial contravariant component and B^θ is the "poloidal"[1] contravariant

[1]The term "poloidal" is used here as the Miller coordinate θ is a poloidal like angle, also for typical equilibrium $B^r = 0$ and the poloidal magnetic field is described by B^θ.

component of the poloidal magnetic field.

Through the link between A_ϕ and ψ and noting that $\mathbf{B} = \nabla \times \mathbf{A}$, the poloidal magnetic field components are related to the derivatives of ψ:

$$B^r = \frac{\partial_\theta \psi}{\sqrt{G}}, \tag{5.5}$$

$$B^\theta = -\frac{\partial_r \psi}{\sqrt{G}}, \tag{5.6}$$

where G is the determinant of the metric tensor.

As the transformation equations between $(r, \theta\phi) \to (R, Z, \phi)$ are known, the Jacobian can be used to express the Miller poloidal magnetic field components B^r, B^θ in terms of the cylindrical components B_R, B_Z, which are needed for the modelling of the pitch angle (see Appendix B). The relevant equations are:

$$B_R = \partial_r R \; B^r + \partial_\theta R \; B^\theta, \tag{5.7}$$

$$B_Z = \partial_r Z \; B^r + \partial_\theta Z \; B^\theta, \tag{5.8}$$

Thus if a realistic poloidal magnetic flux function is known or prescribed, the poloidal magnetic field components can be calculated.

5.1.1 Model for the poloidal flux function ψ

A parameterized form of the poloidal flux function ψ has been chosen on the basis that the profile of the toroidal plasma current density can often be expressed in the modified parabolic form:

$$j^\phi = j_0 \left(1 - \left(\frac{r}{a}\right)^\alpha\right)^\beta, \tag{5.9}$$

where α controls the general shape of the profile, β controls the shape of the profile at the edge of the plasma, a is the minor radius of the plasma and r is the flux surface radius from the magnetic axis, and is equivalent to the coordinate r in the Miller model.

As α is the dominant parameter which controls the general shape of the current profile, the parametric form for j^ϕ above has been used within this thesis with $\beta = 1$. For a parabolic form $\alpha = 2$ and for a "flatter" profile $\alpha > 2$.

For the case of a large aspect ratio tokamak the toroidal bending of the current density can be neglected, allowing the functional form of the poloidal flux function to be easily calculated using Ampère's law. As a first approximation, it is assumed that the functional form of ψ will not differ significantly between the large and small aspect ratio cases. Using Ampère's law and the definition of ψ, together with the parametric form for the current density above, the parameterised form of ψ obtained is (see Appendix C)

$$\psi = c\left(\frac{r^2}{4} - \frac{r^{\alpha+2}}{(\alpha+2)^2 a^\alpha}\right), \tag{5.10}$$

where c is a constant which alters the magnitude of the derived magnetic fields and α is the same parameter as in Eq. 5.9 which controls the effective current density distribution.

The constant c depends on the total toroidal plasma current and hence controls the magnitude of the poloidal magnetic field calculated from ψ. As will be demonstrated shortly, it is possible to calculate the toroidal current density from ψ. Thus the total toroidal current for the prescribed ψ can be estimated, allowing the constant c to be determined such that it is consistent with the measured total toroidal current on the actual tokamak.

5.1.2 Equilibrium and Shafranov shift

The plasma current, total magnetic field and the plasma pressure are linked through the plasma equilibrium condition. If an accurate model of the magnetic fields within a tokamak is to be created, it must satisfy the equilibrium conditions. Thus in a model only two of the current, magnetic field and pressure can be freely specified [3].

Specifying a parameterized form of the poloidal magnetic flux ψ and the well known toroidal magnetic field B_ϕ, it is clear that the magnetic field has been freely chosen. As Maxwell's equations hold, the plasma current has also been freely chosen, since $\nabla \times \mathbf{B} = \mu_0 \mathbf{j}$. Hence the pressure profile has also been intrinsically specified.

A consequence of the force balance between the plasma pressure and the magnetic pressure is that the centres of the magnetic flux surfaces are displaced with respect to the bounding surface. This displacement of the centre of a flux surface is called the Shafranov shift and is dependent on the particular forms of the pressure profile and poloidal magnetic field [2]. Thus with the method chosen it is not possible to arbitrarily define the Shafranov shift and retain a model which satisfies the equilibrium condition.

The Shafranov shift is a fundamental quantity which appears in the transformation equations for the Miller representation. Correct modelling relies on this quantity being well known.

As a first approximation, the form of the Shafranov shift $\Delta R_0(r)$ used in this model will be that of the large aspect ratio case. Lao *et al.*[39] have shown that the derivative of the Shafranov shift with respect to the flux surface label, $\partial_r \Delta R_0$, for an elliptical generalization is proportional to r. Within the Miller model the centre of a flux surface is described by $R_0(r) = R_{major} + \Delta R_0(r)$, where R_{major} is the major radius of the tokamak. Using $\Delta R_0(r) \propto r$ a logical choice for $R_0(r)$ is

$$R_0(r) = R_{major} + s\left(1 - \frac{r^2}{a^2}\right), \tag{5.11}$$

where s is a constant and is equivalent to the distance the magnetic axis of the plasma is shifted from the major radius.

Using the differential form of Ampère's law, the toroidal plasma current can be numerically estimated directly from the poloidal flux function ψ (see appendix D). The relevant form of j^ϕ is

$$j^\phi = \frac{\sqrt{g_{\phi\phi}}}{\mu_0\sqrt{G}}\left[\frac{\partial}{\partial r}(g_{\theta r}B^r + g_{\theta\theta}B^\theta) - \frac{\partial}{\partial \theta}(g_{rr}B^r + g_{r\theta}B^\theta)\right]. \tag{5.12}$$

The metric coefficients which appear in the formula for the toroidal current are dependent on the derivative of the Shafranov shift $\partial_r \Delta R_0(r)$. Thus varying the constant which describes the magnitude of the Shafranov shift s, causes the form of the calculated current density to vary. As the current is a flux surface quantity, s is optimised such that the calculated current density peaks on axis.

Figure 5.1 shows two identical poloidal flux functions, having parameters $c = 1.08$ and $\alpha = 2$, and the numerically estimated toroidal current density for two different values of the Shafranov shift parameter s. Part (a) has $s = 0$ and (b) has had the Shafranov shift

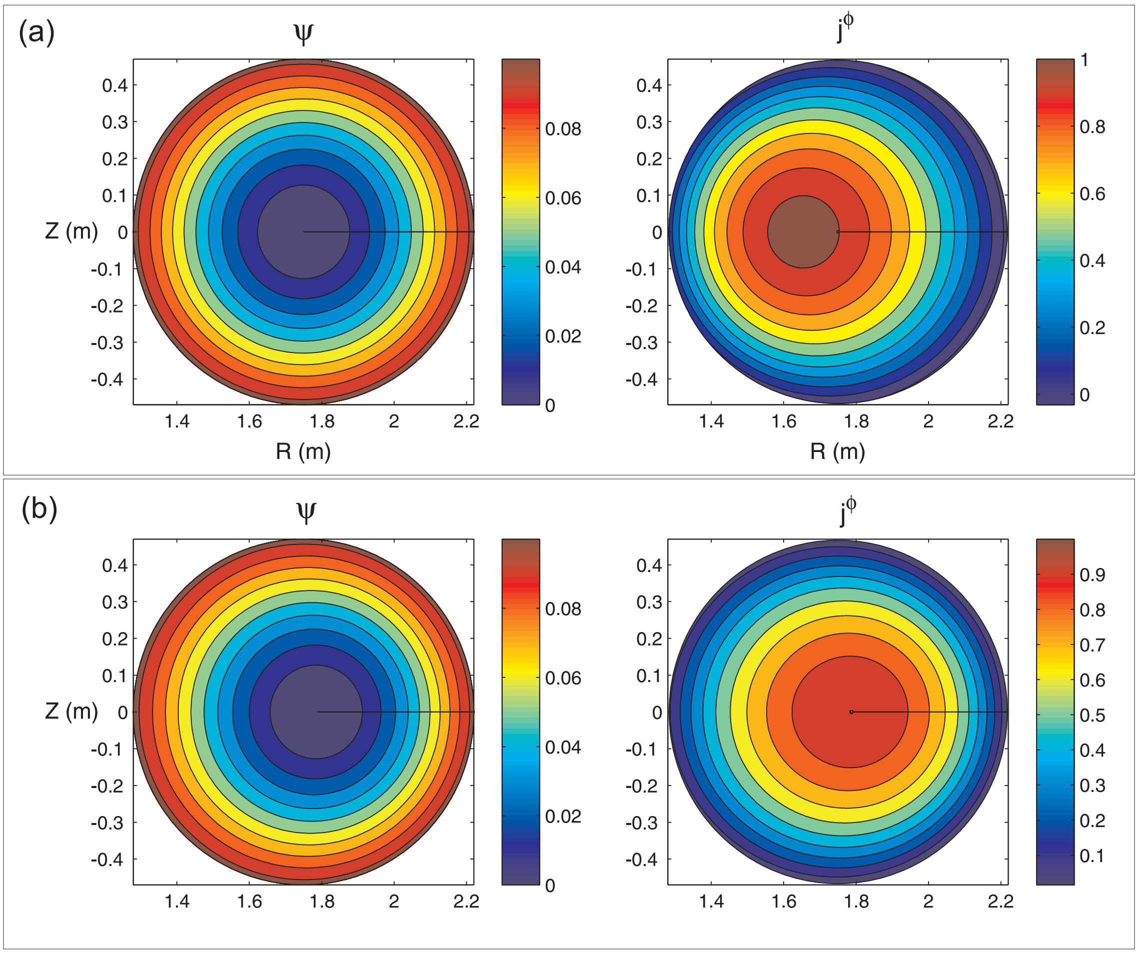

Figure 5.1: **(a)** Contour plot of the prescribed poloidal flux function ψ and the corresponding j^ϕ, calculated with Eq. 5.12, with no Shafranov shift ($s = 0$ m). **(b)** Same form of ψ as in **(a)** and the corresponding j^ϕ, but calculated with the optimised Shafranov shift ($s = 0.038$ m). It is easily seen that without the correct value for s the toroidal current density j^ϕ is not a flux function and hence the configuration does not satisfy the equilibrium condition.

optimised, where for this particular form of ψ $s = 0.038$ m. This optimised value of s, calculated from only the major magnetic components, is close to the observed values for the Shafranov shift on TEXTOR, which range from 5 to 7 cm.

Taking the poloidal surface integral over the numerical estimate of the toroidal current density, the total toroidal current I_ϕ can be estimated. This allows the constant c, controlling the magnitude of ψ Eq. 5.10, to be determined such that I_ϕ is consistent with the total current measured on a tokamak device. This enables the correct magnitude of the poloidal magnetic field to be calculated. The form of I_ϕ is determined by the poloidal surface integral in Miller coordinates:

$$I_\phi = \int_0^{2\pi} \int_0^a j^\phi \sqrt{g_{rr} g_{\theta\theta} - g_{r\theta}^2}\, dr d\theta, \tag{5.13}$$

where a is the minor radius of the plasma.

5.1.3 TEXTOR model poloidal magnetic fields

With the prescription of an appropriate form of the poloidal flux function ψ, physically reasonable poloidal magnetic fields can be modelled. To illustrate this, a poloidal cross section of TEXTOR is shown here with figures of the poloidal magnetic field components B_R, B_Z needed for the computation of the MSE pitch angle.

The parameters which have been used for TEXTOR are

Parameter	Value
Major radius (R_{major})	1.75 m
Minor radius (a)	0.47 m
Toroidal magnetic field on axis ($B_{\phi 0}$)	2.2 T
Toroidal plasma current (I_ϕ)	3.5 x 10^5 A
Elongation (κ)	1.0
Triangularity (δ)	0.0

The values for the toroidal magnetic field and current that are given here are those which were used for the majority of the plasma discharges encountered during the program at TEXTOR. The maximum values which can be obtained on TEXTOR are $B_{\phi_0} = 3.0$ T and $I_\phi = 8$ x 10^5 A.

To reinforce the method used to calculate the poloidal magnetic field components and the approximate value for the Shafranov shift, Figs. 5.2 & 5.3 not only show the magnetic field components B_R, B_Z but also the form of ψ and the estimated current j^ϕ. Radial plots of the flux function and current show the general form.

Figure 5.2 has been calculated with the shape parameter $\alpha = 2$, the constant $c = 1.08$ such that $I_\phi \approx 3.5\text{x}10^5$ A and the optimised value for the displacement of the magnetic axis is $s = 0.038$ m. It can be seen from the radial profile of the current density that it conforms to the expected parabolic profile.

Figure 5.3 has been calculated with the shape parameter $\alpha = 3$, the constant $c = .90$ such that $I_\phi \approx 3.5\text{x}10^5$ A and the optimised value for the displacement of the magnetic axis is $s = 0.038$ m. The current density profile for this shape parameter can be seen to be “flatter” than the parabolic case. It may be noticed that value of j^ϕ does not go to 0 near the outer edge, this is due to the the difficulty of computing numerical derivatives at the periphery of the plasma.

To check the validity of the method outlined, which calculates the poloidal magnetic field B_R and B_Z by transforming the problem to flux surface coordinates and completing the necessary derivatives in this space, an alternate method can be used to calculate the poloidal magnetic fields for a poloidal cross section of a plasma. For the cylindrical coordinate system there are well known relations between B_R, B_Z and the derivatives of ψ:

$$B_R = -\frac{1}{R}\frac{\partial\psi}{\partial Z}, \qquad B_Z = \frac{1}{R}\frac{\partial\psi}{\partial R}. \tag{5.14}$$

Thus the poloidal magnetic field components shown in Fig. 5.2 & 5.3 can be checked against the equivalent components calculated by specifying ψ in terms of the cylindrical coordinates (R, Z), using the transformation equations, and taking the numerical derivatives of ψ. It has been found the poloidal magnetic field components calculated by both methods agree. This has also been checked for plasma which have non-circular flux surface shapes ($\kappa \neq 1, \delta > 0$).

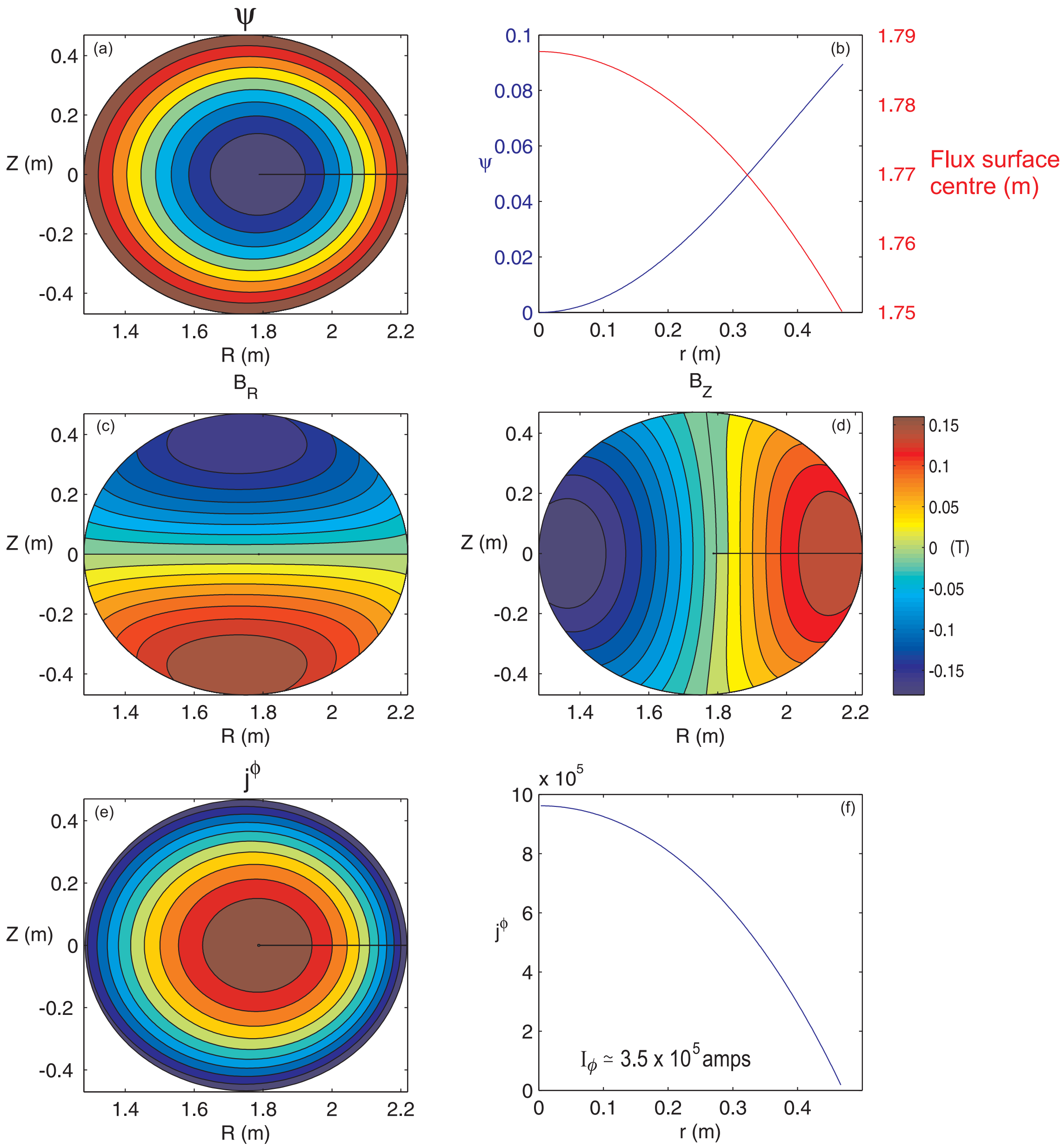

Figure 5.2: **(a)** Poloidal cross section contour plot of the prescribed poloidal flux function with the parameters ($\alpha = 2, c = 2.16, s = 0.038$). **(b)** Radial profiles of ψ (blue) and of the flux surface centre/ Shafranov shift (red). **(c)** & **(d)** Poloidal magnetic field components B_R and B_Z (both have the same colour scaling). **(e)** Calculated toroidal current density j^ϕ with a radial profile given **(f)**, also indicating that the integrated current density gives a value of $I_\phi \approx 3.5$ x 10^5 amps.

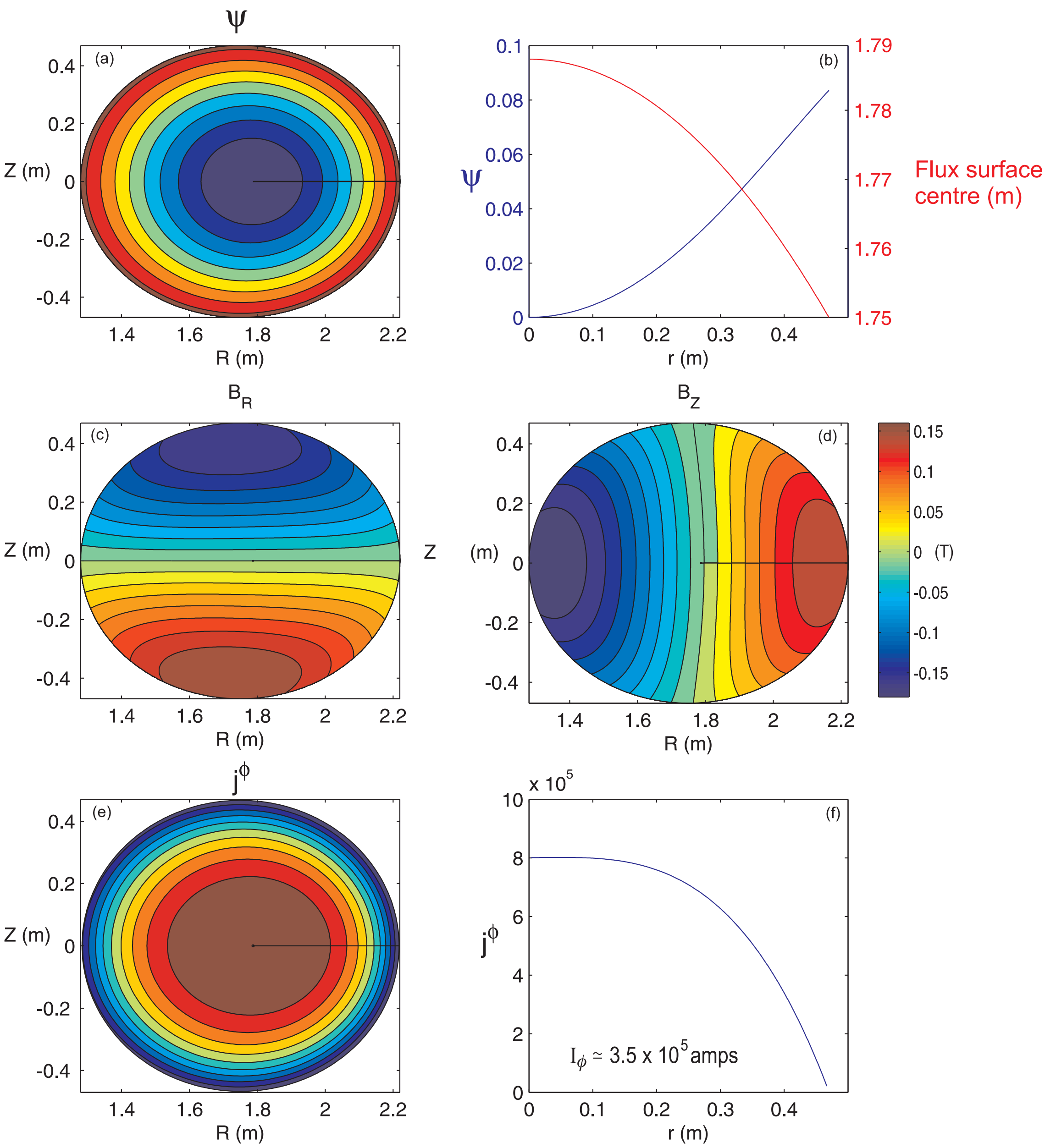

Figure 5.3: **(a)** Poloidal cross section contour plot of the prescribed poloidal flux function with the parameters ($\alpha = 3, c = 1.8, s = 0.037$). **(b)** Radial profiles of ψ (blue) and of the flux surface centre/ Shafranov shift (red). **(c)** & **(d)** Poloidal magnetic field components B_R and B_Z (both have the same colour scaling). **(e)** Calculated toroidal current density j^{ϕ} with a radial profile given **(f)**, also indicating that the integrated current density gives a value of $I_\phi \approx 3.5$ x 10^5 amps.

5.2 Model MSE polarization pitch angle map

Integrating all the methods explained results in accurate models of the pitch angle map of the polarized MSE emission from the neutral heating beam. The maps shown in this section are ideal as they correspond to a single vertical sheet through the centre of the neutral beam. A complete representation which incorporates line integration effect is given in the next section.

In order to calculate the pitch angle map, the viewing geometry must be described. The view obtained of the neutral beam by the instrument at TEXTOR is completely described by the following parameters:

Parameter	Value
Instrument view origin	(2.14, 0.99, 0)
Vertical viewing angle range (θ)	-5 to 5^o
Horizontal viewing angle range (χ)	145 to 160^o
Neutral beam vertical origin	(7.67, 1.65)
Neutral beam horizontal origin	(9.67, 1.65, 0)

where the origin values, (x,y,z), are given in metres. The values for the different origins of the neutral beam have been calculated using the position given for the neutral beam grids and the two characteristic focal lengths for the beam from these grids as given in [24].

Before the model MSE pitch angle maps are shown, an overview of the method used to calculate these figures is given by the flowchart in Fig 5.4.

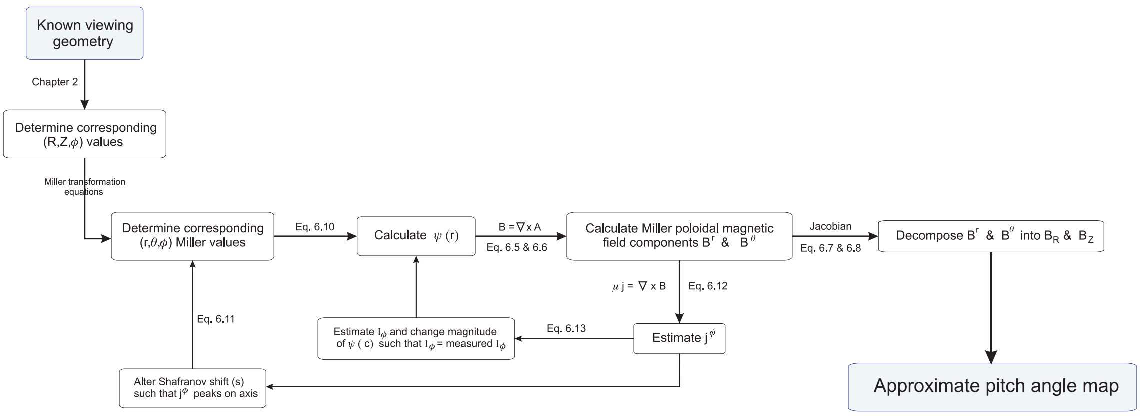

Figure 5.4: Flowchart of method used to determine the pitch angle map

The polarization pitch angle maps shown in this section have been calculate using the full pitch angle equation as derived in chapter 2, which is

$$\boxed{\begin{aligned} S &= \frac{a_1 B_R + a_2 B_Z - a_3 B_\phi}{\sin\xi(\sin\beta B_R + \cos\beta B_\phi) - \cos(\alpha+\beta)\cos\xi B_Z}, \qquad (5.15) \\ a_1 &= \cos\beta\sin\theta\sin\xi + \cos\alpha\cos\theta\cos\xi, \\ a_2 &= \sin(\alpha+\beta)\sin\theta\cos\xi, \\ a_3 &= \sin\beta\sin\theta\sin\xi - \sin\alpha\cos\theta\cos\xi. \end{aligned}}$$

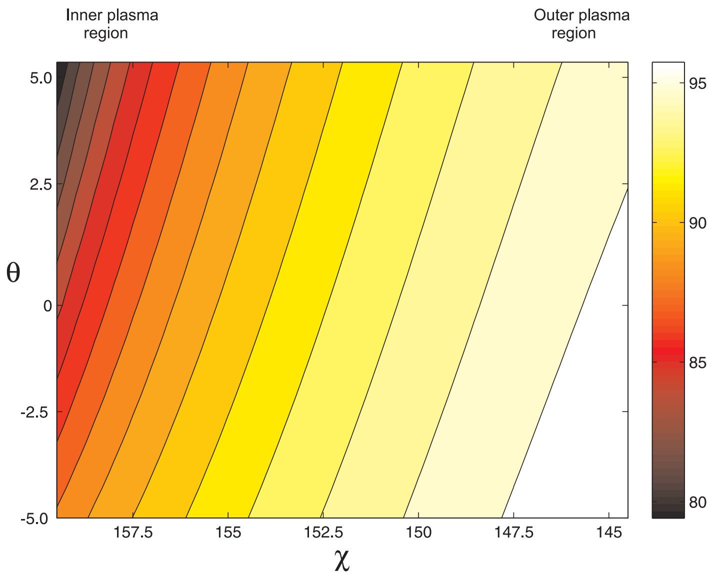

Figure 5.5: Calculated pitch angle map for the centre sheet of the neutral beam on TEXTOR. The parameters used for the prescribed flux function to determine the poloidal magnetic field strengths are ($\alpha = 2, c = 2.16, s = 0.038$). The horizontal angle χ is shown to decrease from left to right so the image as presented here is oriented the same as what is captured by the camera, that is inner region of the plasma to the left and outer to the right.

Figure 5.5 is the expected polarization pitch angle map for the ideal central vertical sheet of the TEXTOR neutral beam. Calculated with same plasma properties and view parameters which were achieved in the previous program. This pitch angle map has the same general form as the previously modelled pitch angle maps using the large aspect ratio assumption but with slightly different values (the previously modelled pitch angle maps can be found in [40]).

All the model pitch angle maps calculated in the rest of this thesis will be calculated from a poloidal flux function with the parameters ($\alpha = 2, c = 2.16, s = 0.038$).

In chapter 2 the importance of the neutral beam divergence was discussed. With the current model, the importance of the divergence can be illustrated by showing the change in the expected pitch angle map. Figure 5.6 is the pitch angle map calculated with no beam divergence, that is $\xi = 0$ in Eq. 3.26. As the map is changed by a significant amount, determining the velocity profile of the neutral beam is vital to understanding the polarization pitch angle maps produced by the instrument.

With a tool established to calculate the pitch angle map for an arbitrary sheet of the neutral beam, it is now possible to investigate the line of sight integration effects.

5.3 Line of sight integration effects

It is important to understand the effect that the non-zero width of the neutral beam has on the data captured. As the flux surfaces are toroidal in nature, any vantage point viewing the neutral beam will result in a loss of information as the nett polarization measured by the instrument will be the culmination of the emission along a sightline. This line of sight integration can be minimised by adopting a view which looks “along” the magnetic surfaces, as discussed in chapter 2. The view obtained at TEXTOR which is being considered is such a viewing geometry which satisfies this condition.

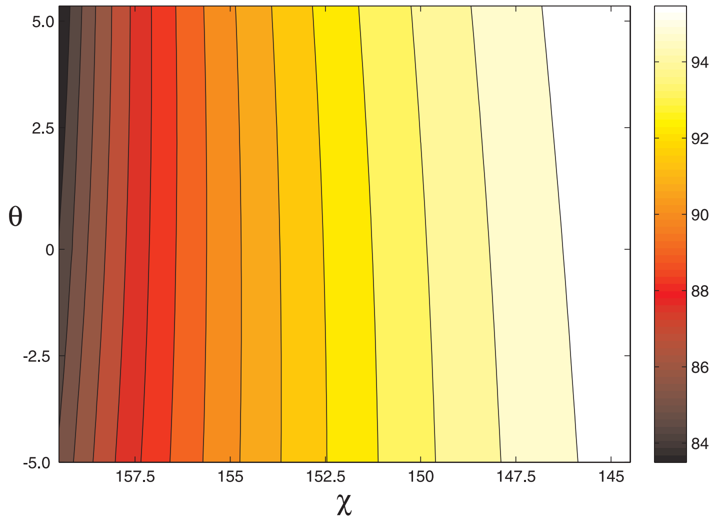

Figure 5.6: Calculated pitch angle map for the centre sheet of the neutral beam on TEXTOR for an ideal non-divergent neutral beam ($\xi = 0$). Identical ψ parameters used as Fig. 5.5.

As it is the polarization angle of the emission from the neutral beam which is being measured, it can be completely described by a Stokes vector. This allows the nett polarization angle to be calculated from the nett Stokes vector, which will be the weighted sum of the Stokes vectors that describes the emission at positions along a sightline. The beam's intensity profile will determine the weighting, meaning it must be known or prescribed.

For the neutral beams on TEXTOR, studies have been carried out which have determined the power distribution of the beam [24]. It has been determined that the profile of the beam can be well approximated by a 2D gaussian, with a vertical full width half maximum (FWHM) of 21-23 cm and horizontal FWHM of 18 cm. For this thesis it will be assumed that the power profile is a valid brightness profile for the beam. Furthermore the attenuation of the beam profile will be ignored resulting in the 2D gaussian being used to describe the entire neutral beam.

The Stokes parameters which describe the vector can be calculated by the electric field strengths of a fixed basis. As the pitch angle is calculated through the ratio of the electric field strengths in the two orthogonal directions of the viewing plane $(\mathbf{e}_j, \mathbf{e}_k)$, which is a fixed basis, the corresponding Stokes parameters can be easily calculated.

In the fixed basis $(\mathbf{e}_j, \mathbf{e}_k)$, the Stokes parameters are

$$s_0 = |E_j|^2 + |E_k|^2, \tag{5.16}$$

$$s_1 = |E_j|^2 - |E_k|^2, \tag{5.17}$$

$$s_2 = 2\mathrm{Re}(E_j E_k^*), \tag{5.18}$$

$$s_3 = 2\mathrm{Im}(E_j E_k^*). \tag{5.19}$$

As the emission is linearly polarized $s_3 = 0$, which agrees with the fact that the equations for E_j, E_k are purely real. Only two Stokes parameters are needed to determine the nett polarization angle, it has been chosen to use s_1 and s_2

When the neutral beam is split into n vertical sheets, the nett Stokes parameters for a pixel descried by the angles (χ_i, θ_i) is calculated by the addition of each parameter for

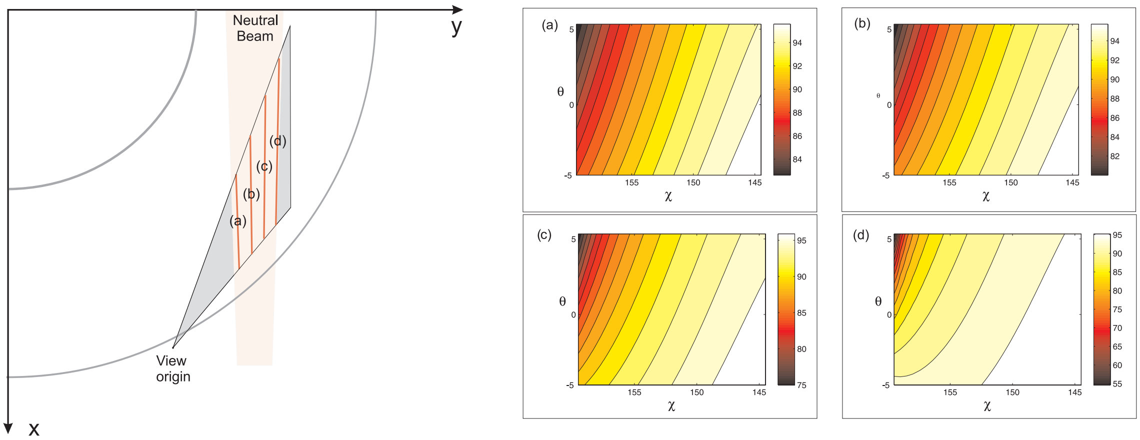

Figure 5.7: The left hand schematic shows the viewing geometry achieved at TEXTOR. The neutral beam is shown split into 4 sheets (in red). Each of the calculated pitch angle maps on the right correspond to the the 4 equally spaced sheets of the neutral beam.

each sheet at this position, weighted by the intensity profile of the beam at that position. This can be written as

$$s_{1_{nett}} = \sum_{1}^{n} w_i \; s_{1_i}, \tag{5.20}$$

$$s_{2_{nett}} = \sum_{1}^{n} w_i \; s_{2_i}, \tag{5.21}$$

$$\tag{5.22}$$

where w_i is the weighting factor and s_{1_i}, s_{2_i} are calculated from Eq. 5.17 & 5.18.

The weighting function that has been used in this model is the 2D gaussian beam profile as described in [24]. The neutral heating beam is best described using the cartesian coordinates (y, z), thus the weighting function is a function of position $w_i \equiv w_i(y, z)$. For each sheet of the beam these coordinates are known, as the view of the instrument has been related to the position within the tokamak in chapter 3. The weighting function used is

$$w_i(y, z) = \exp\left(-\frac{(y - y_c)^2}{2\sigma_h^2}\right) \exp\left(-\frac{z^2}{2\sigma_v^2}\right), \tag{5.23}$$

where $y_c = 1.65$ is the y-position of the centre of the beam, σ_h and σ_v are determined from the horizontal and vertical FWHM of the beam respectively.

To determine the overall pitch angle the nett electric field components $E_{j_{nett}}, E_{k_{nett}}$ must be calculated from the nett Stokes parameters, it can be shown that

$$E_{j_{nett}} = \sqrt{s_{1_{nett}} + \sqrt{s_{1_{nett}}^2 + s_{2_{nett}}^2}/2}, \tag{5.24}$$

$$E_{k_{nett}} = \frac{s_{2_{nett}}}{2E_{j_{nett}}}. \tag{5.25}$$

Figure 5.7 shows the pitch angle for 4 vertical sheets of the TEXTOR neutral beam,

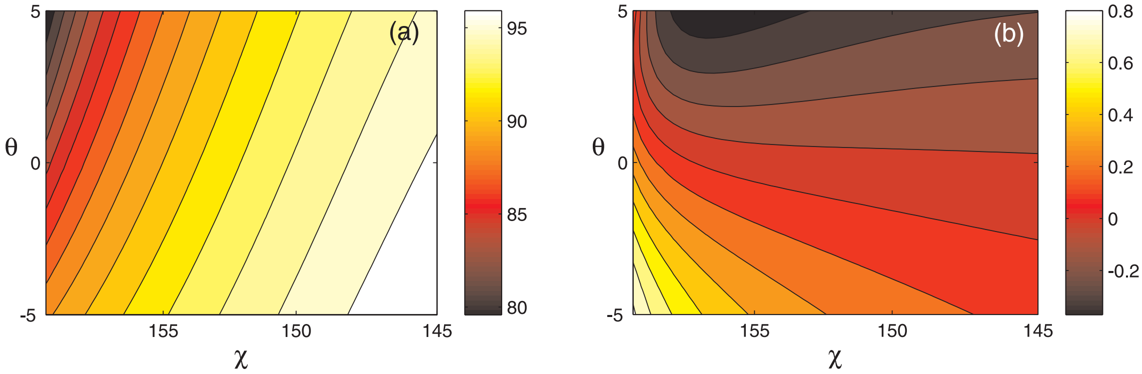

Figure 5.8: (a) The calculated pitch angle map with line integration effects accounted for by modelling the neutral beam with a 2D gaussian intensity profile (horizontal FHWM 18 cm and vertical FWHM 22 cm) split into 100 sheets and taking the beam divergence as 1^o. **(b)** Difference between line integrated pitch angle map (**a**) and the ideal pitch angle map corresponding to central sheet (Fig. 5.5).

with the corresponding positions of these sheets is also shown in the schematic of the viewing geometry for TEXTOR.

Figure 5.8 **(a)** is the line integrated pitch angle map for TEXTOR with the neutral beam split into 100 vertical sheets, **(b)** is the difference between the line of sight integrated pitch angle of **(a)** and the pitch angle for the central sheet of the neutral beam (Fig. 5.5).

The line of sight integration effects are minimal for this viewing geometry as it is looking "along" the magnetic flux surfaces. For the main region of interest in the image, the central area, the difference is in the order of the resolution of the instruments, 0.2^o. However, the 2D gaussian used for the brightness profile is currently constant for the entire beam. Due to the attenuation and the divergence of the beam, it is expected that this model profile will be over estimating the line of sight integration effects. A more accurate description of the beam profile can be determined by treating the beam as circularly symmetric and Abel inverting an image of the beam brightness, which can easily be produced from the data.

The work presented up to this point, provides a complete method to model a 2D MSE imaging system. This method is an extension of the previous simplistic technique which did not incorporate important aspects of the magnetics with a tokamak (toroidal bending of the current plasma current density, magnetic geometry which satisfies the equilibrium condition) and the horizontal divergence of the neutral heating beam.

5.4 Modelling MSE images with MHD instability

As the 2D MSE instrument is an imaging system, it has the inherent capability to capture information on magnetic field perturbations within a tokamak. The purpose of this section is to gain an understanding of the changes to the pitch angle map when an idealistic magnetic perturbation is considered, furthermore if information on the underlying perturbation can be extracted.

Previously, at the end of chapter 3, a method was outlined, where for a view along the neutral beam, the pitch angle equation reduces to an approximate form which allows the perturbed vertical magnetic field component to be extracted using a synchronous and DC image of the plasma. In this section, a heuristic model for the underlying kink mode of the sawtooth instability will be used in order to assess the validity of the approximate equation and illustrate the extraction of the perturbed field.

The view which shows the most promise for the internal magnetic structure to be extracted from the images is that which corresponds to the typical view for the conventional 1D systems, that is looking "along" the magnetic surfaces, and corresponds to the view achieved at TEXTOR in the previous program. The approximate form of the pitch angle equation for such a view is

$$S \approx \frac{\sin \alpha B_\phi}{\xi \cos \beta B_\phi - \cos(\alpha + \beta) B_Z}. \tag{5.26}$$

Figure 5.9 **(a)**-**(c)** shows model pitch angle maps calculated for the view at TEXTOR with the full pitch angle equation, the approximate equation above and the difference between the two respectively. It is clear that the majority of the field of view is well approximated by Eq. 5.26, as the difference in the pitch angle is less than 0.2^o except for the top left hand corner (the error in the best measurements is expected to be $\sim 0.2^o$). The next step is to check the validity of this equation when a perturbation is applied to the magnetic field. In order to complete this, a model which represents a realistic perturbation must be used.

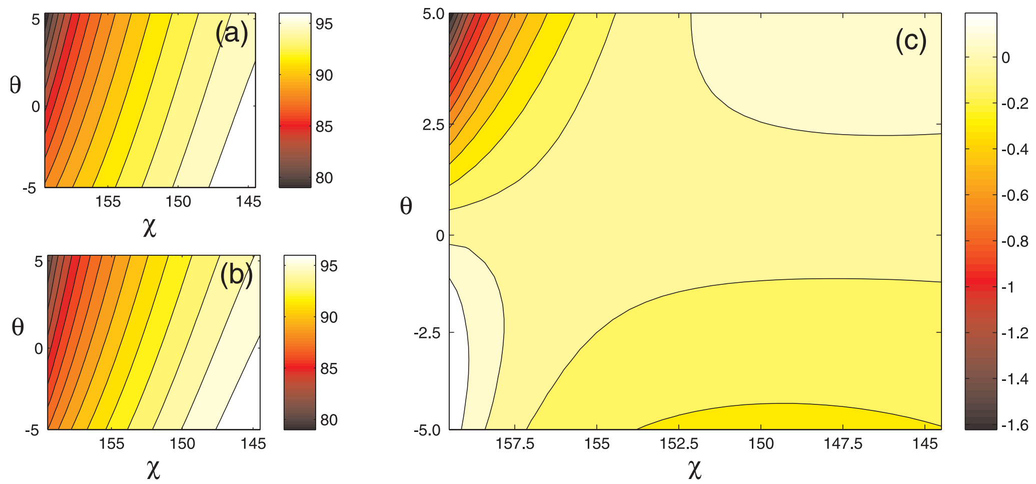

Figure 5.9: **(a)** Pitch angle map for the centre sheet calculated with the full pitch angle equation (Eq. 5.15). **(b)** Pitch angle map for the centre sheet calculated with the approximate form of the pitch angle equation (Eq. 5.26). **(c)** The difference between the calculated pitch angle maps of **(a)** & **(b)**, showing that for this view the pitch angle is well approximated by that of Eq. 5.26.

The instability which will be used to base a heuristic model on, is the sawtooth instability. This is due to the fact that the underlying magnetic perturbation of the sawtooth is an internal kink mode, which has a toroidal mode number $n = 1$ and dominant poloidal mode number $m = 1$. The kink mode leads to a helical displacement of the core magnetic surfaces. As this perturbation corresponds to a stationary instability in the rest frame of the plasma, if the mode not is quiescent, to first order the instability can be modelled as a simple perturbation to the poloidal flux function:

$$\tilde{\psi} = \psi + af(r)\cos(\theta + \phi + \delta), \tag{5.27}$$

where a is a constant which controls the magnitude of the perturbation, $f(r)$ is a function which controls the region of the perturbation , δ is a phase constant and ψ is the unperturbed/DC flux function.

In the method developed in this thesis to determine the poloidal magnetic field, the relation between ψ and A_ϕ is only valid for toroidally symmetric equilibria. As a first approximation this relation will be assumed to hold, allowing approximate forms of the poloidal magnetic field components to be estimated (using $\mathbf{B} = \nabla \times \mathbf{A}$).

The form of the function $f(r)$ has been taken to be a gaussian, such that the perturbation will be applied in a continuous manner, hence the form will be

$$f(r) = \exp\left(\frac{-(r - r_i)^2}{2\sigma}\right), \tag{5.28}$$

where r_i is the position where the peak perturbation occurs and σ_i is the width which controls the region of interest.

For the kink instability, the region of the plasma which is perturbed is that which has a safety factor of less than one ($q < 1$). Thus the appropriate values for r_i and σ_i can be found through finding the profile of the safety factor for the unperturbed flux function ψ. The safety factor can be estimated through the definition

$$q = \frac{d\psi_{tor}}{d\psi_{pol}} = \frac{\partial\psi_{tor}}{\partial r} \Big/ \frac{\partial\psi_{pol}}{\partial r}, \tag{5.29}$$

where ψ_{tor} is the toroidal magnetic flux and $\psi_{pol} \equiv \psi$ is the poloidal magnetic flux. As the toroidal magnetic field is well known, the derivative of the toroidal magnetic flux can be easily computed from it's definition, which is $\psi_{tor} = \int_S \mathbf{B} \cdot \mathbf{e}^\phi da$ [34]. In the Miller representation, the derivative of ψ_{tor} is

$$\frac{\partial\psi_{tor}}{\partial r} = \int_0^{2\pi} B^\phi \sqrt{g_{rr}g_{\theta\theta} - g_{r\theta}^2}\ d\theta. \tag{5.30}$$

For a poloidal flux function defined by the parameters ($\alpha = 2, c = 2.26, s = 0.038$), which corresponds to a parabolic current density profile, the constants for $f(r)$ have been determined to be $r_i = 0.08$ m and $\sigma_i = 0.0255$, which is easier represented as the FHWM of the gaussian is 0.6 m. This radial influence function is shown in Fig. 5.10, where the calculated safety factor has been overlayed illustrating that the perturbation is contained to the region of the plasma which has a safety factor $q < 1$.

The magnitude for the ideal perturbation, which will be used for the duration of the modelling, has been chosen such that the perturbed ψ resembles tomographically reconstructed images of ψ as seen in [41], the parameters used being $a = 0.0025$ which is equivalent to approximately 3% of the maximum value of ψ for this configuration. Figure 5.11 shows the perturbed structure of ψ, as well as the overall poloidal magnetic field

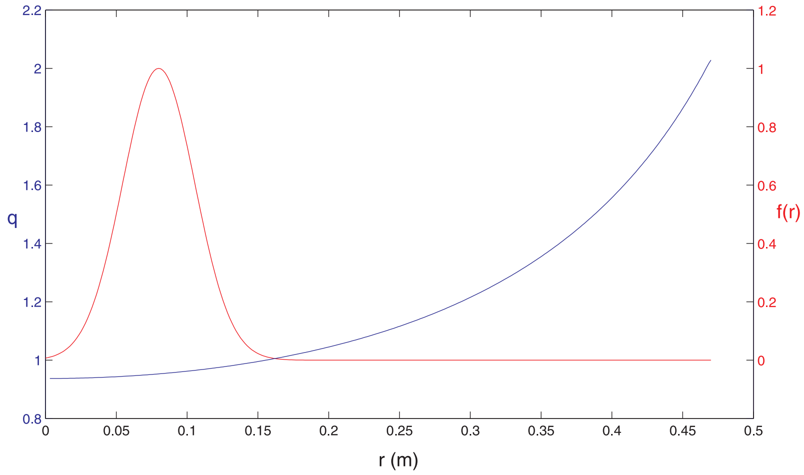

Figure 5.10: Radial profile of the safety factor q for a model plasma with toroidal magnetic field strength on axis of 2.2 T and model poloidal flux function which has $(\alpha = 2, c = 2.16, s = 0.038)$. Overlayed is the perturbation influence function $f(r)$ (with $r_i = 0.08, \sigma_i = 0.0255$) which has been chosen that it only adds a perturbation to the region of the plasma which has a safety factor of less than one, $q < 1$.

components associated with such a form of ψ, calculated using the assumed relationship between ψ and A_ϕ.

Now with this heuristic model for the perturbed poloidal flux function, the 2D MSE pitch angle map can be calculated for the first time. As the procedure to calculate the pitch angle involves relating the horizontal angle χ of the instrument to the toroidal angle ϕ, the helical nature of the kink mode and thus the perturbation can be incorporated.

Figure 5.12 shows the expected pitch angle map for the central sheet of the TEXTOR neutral beam as calculated with the full pitch angle equation. It is seen that compared to the previous pitch angle maps for un-perturbed magnetic fields, Fig. 5.5, that there is a large change to the structure of the image (an encouraging sign for the extraction of the perturbed magnetic field). For the extraction, the approximate form for the pitch angle equation, Eq. 5.26, must be valid across the field of view. Figure 5.15 shows the difference between the full and approximate equation, confirming the validity of the approximate equation, as the difference is less than 0.2^o for the vast majority of the field of view.

With the approximate equation for the pitch angle validated the manipulation of a synchronous and DC pitch angle image, can be implemented to extract the perturbed vertical component of the poloidal magnetic field $\tilde{B}_Z$. The equation derived to extract the perturbed vertical magnetic field is

$$\tilde{B}_Z = \frac{\sin\alpha\ B_\phi\ (\cot\gamma_0 - \cot\tilde{\gamma})}{\cos(\alpha+\beta)}. \tag{5.31}$$

where α, β are angles describing the viewing geometry (as given in chapter 3), γ_0 is the unperturbed/DC pitch angle image and $\tilde{\gamma}$ is the synchronous perturbed pitch angle image.

As a first estimate of the ability to extract the perturbed magnetic field using this equation, it will be applied to the simple case of the central sheet of the TEXTOR neutral heating beam. For this scenario the DC image of the pitch angle, γ_0, will be that given by Fig. 5.5 and the synchronous pitch angle image, $\tilde{\gamma}$, will be that of Fig. 5.12.

Figure 5.14 **(a)** shows the perturbed magnetic field component $\tilde{B}_Z$ extracted using the two images given above and Eq. 5.31, **(B)** is the analytic $\tilde{B}_Z$ used in the calculation. The

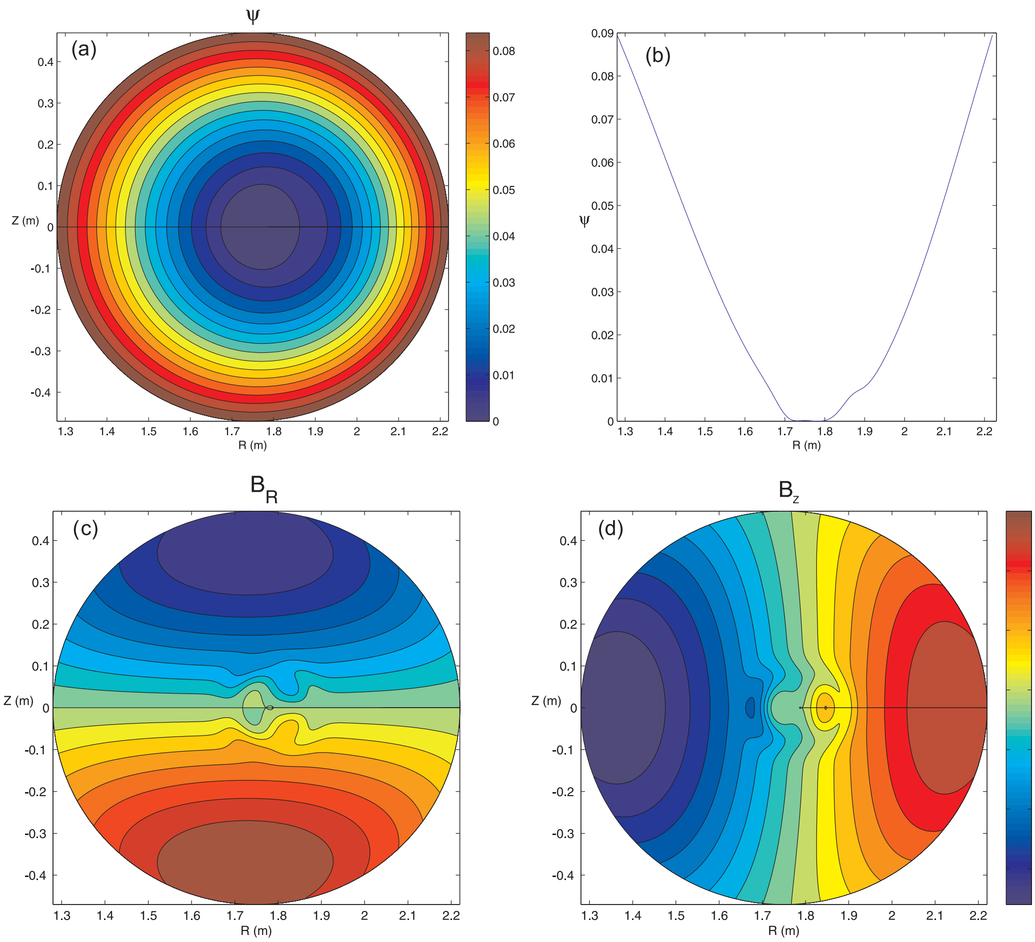

Figure 5.11: (a) Poloidal cross section showing the perturbed poloidal flux function, with perturbation parameters for Eq. 5.27 ($a = 0.0025, \delta = 0$) and $f(r)$ of Fig. 5.10. **(b)** is a cross section of ψ illustrating the form of the perturbation. **(b)** & **(c)** are the calculated B_R and $_Z$ poloidal magnetic components for this perturbed ψ.

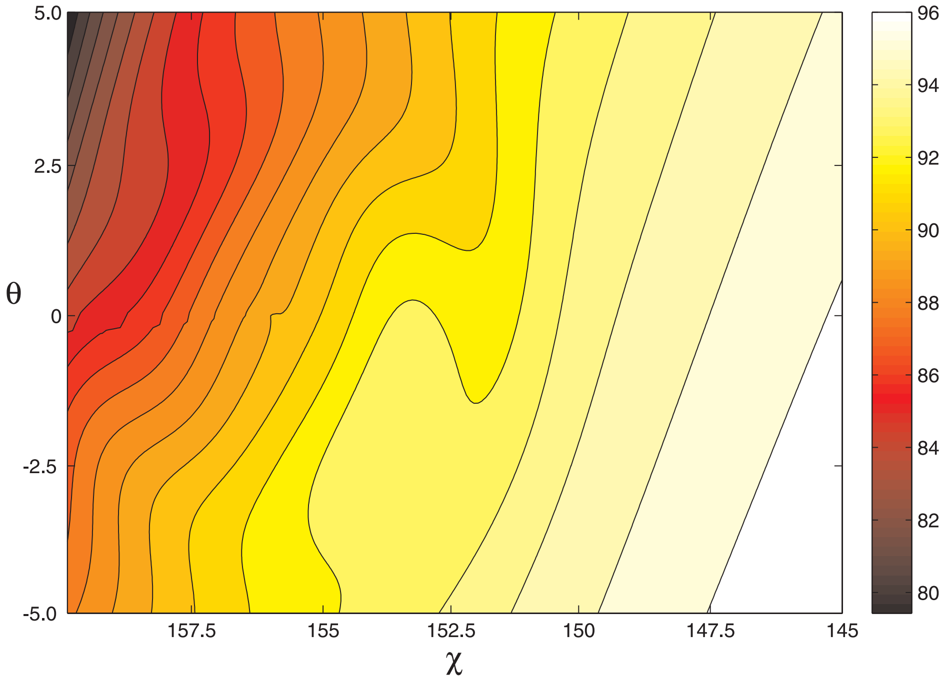

Figure 5.12: Pitch angle map for the centre neutral beam sheet calculated from the perturbed poloidal flux function of Fig. 5.11. Clear structure is observed compared to the unperturbed pitch angle map of Fig. 5.5 (note the cusps on some contours are due to numerical errors associated with the calculation).

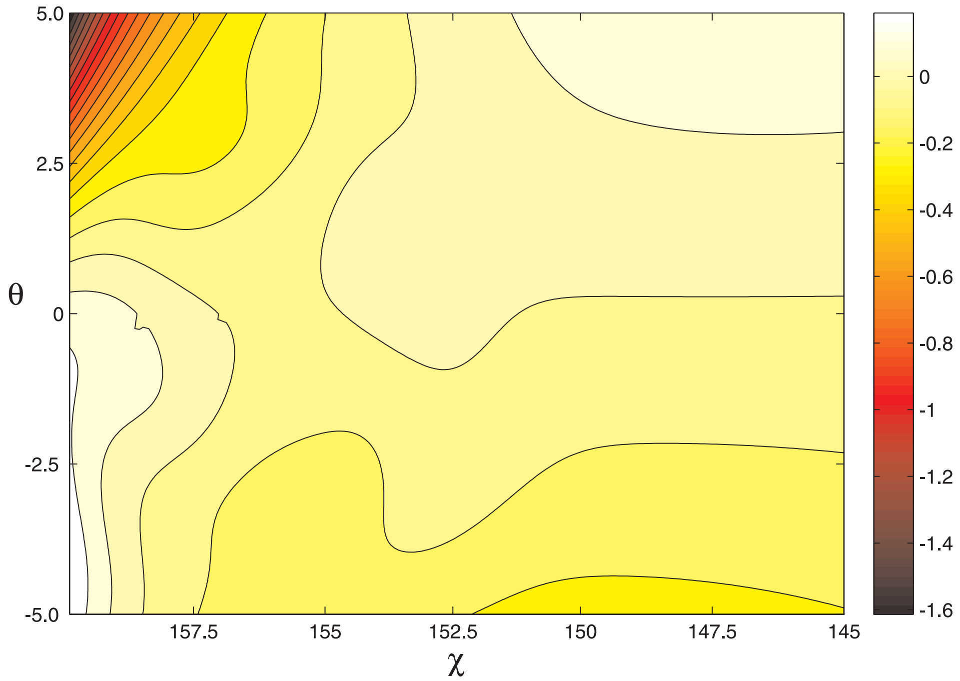

Figure 5.13: Difference between the pitch angle maps, for the perturbed poloidal flux function, calculated with the full and approximate pitch angle equation. It can be seen from the small differences ($< 0.2^o$) across the majority of the image that the pitch angle is well approximated by the approximate equation.

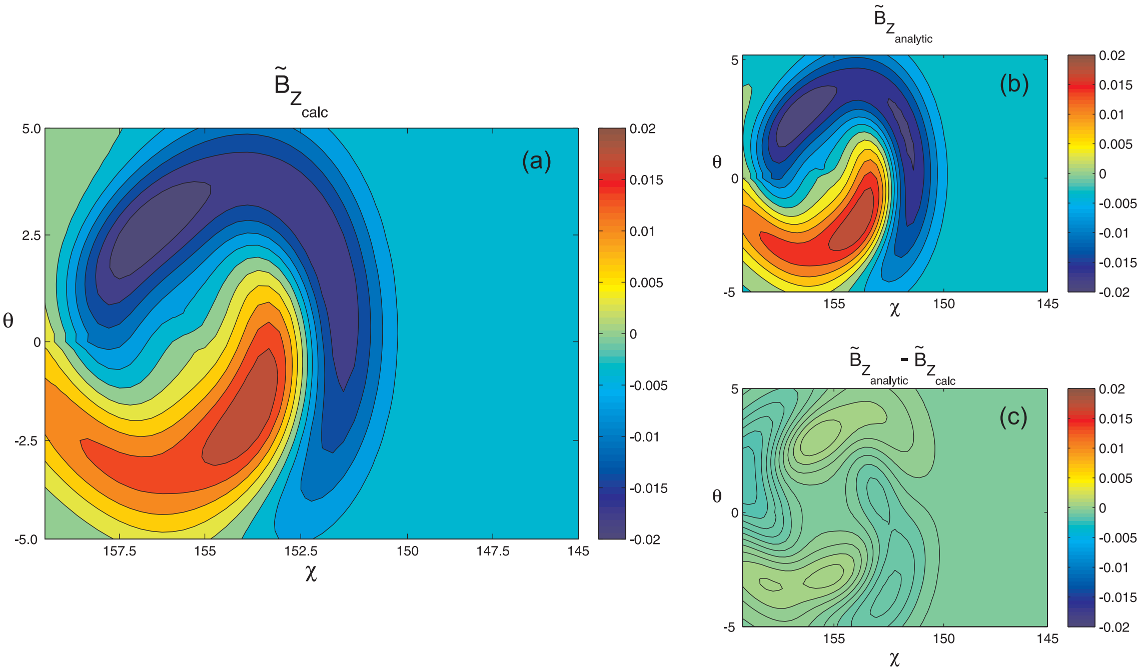

Figure 5.14: **(a)** Shows the determined perturbed vertical magnetic field, $\tilde{B}_Z$, from the two pitch angle images, one synchronised with the perturbation and the other the background DC, using Eq. 5.31. **(b)** A contour plot of the analytic $\tilde{B}_Z$ used in the calculations. **(c)** The difference between **(a)** & **(b)**. All plots have the same colour scaling, illustrating that the differences in **(c)** are very small (< 0.001 T).

difference between these images in given in **(c)**, the difference is small with the maximum being 0.001 T, further validating this procedure.

With the method developed in this thesis, the line of sight integrations effects can easily be modelled to gain an understanding of the effect the non-zero width of the neutral beam has on the extraction procedure. However, in order to extract the perturbed magnetic field through Eq. 5.31, the angles α and β must be known. It has been chosen to apply the calculated α and β from the central sheet of the neutral beam.

Figure 5.15 **(a)** shows the extracted perturbed magnetic field component as calculated with line integration effects. For comparison **(b)** is the analytic perturbed magnetic field for the central sheet and **(d)** is the difference between **(a)** and **(b)**. It can be seen from these figures that the form of the perturbation does not differ between the line integrated calculation and the central sheet calculation, but is reduced in size. The maximum difference is 0.007 T.

Having shown through this modelling that the approximate form of the pitch angle equation is valid for the majority of the field of view, the extraction procedure can be applied to the appropriate images to produce the perturbed magnetic fields (which agree with the analytic form used). The two main questions now are: is it technically feasible to capture the necessary synchronous image? What can we make of this perturbed magnetic field image?

5.4.1 Technical feasibility of determining the perturbed magnetic field

With the method to extract a magnetic perturbation verified by a heuristic model of an instability, the technical feasibility must be established. In order to ascertain this

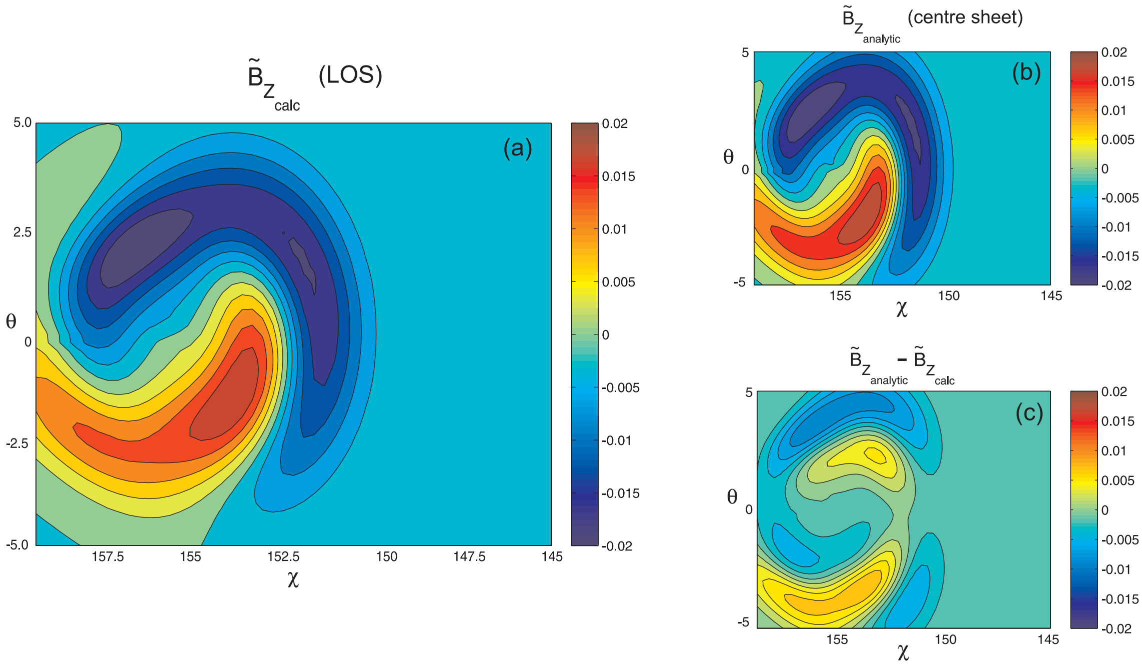

Figure 5.15: (a) Shows the determined perturbed vertical magnetic field, $\tilde{B}_Z$, from the two pitch angle images, which have been calculated with line of sight integration effects, using Eq. 5.31. **(b)** A contour plot of the model $\tilde{B}_Z$ used in the calculations for the centre sheet of the neutral beam. **(c)** The difference between the calculated perturbed $\tilde{B}_Z$ with line integration and the analytic values of the perturbation used for the central sheet of the neutral beam. It can be seen that the line of sight integration effects have decreased the observed height of the perturbation.

the change in intensity measured by the instrument due to the perturbation must be greater than the noise of the measurement. Here the instrument which will be considered is the switching heterodyne system and the CCD camera used at TEXTOR in the last experimental program. The equation which describes the intensity for one of the states of this instrument (taken from chapter 2, Eq. 2.18) is

$$S = \frac{I_0}{2}[1 - \zeta \cos(\phi - 2\theta)], \tag{5.32}$$

where I_0 is the intensity of the incident radiation, ζ is the fringe contrast and will be set to 1 (i.e. an ideal fringe pattern), ϕ is the phase of the fringe pattern and will be taken to be 90^o for simplicity and θ is the polarization/pitch angle.

For this calculation it will be assumed that the only sources of change in the measurement will be due to noise and a change in pitch angle, the result of a magnetic perturbation. As the noise of a CCD is Poissonian, for large photoelectron counts the noise is proportional to the square root of the intensity/counts. Therefore a change in the measured signal S will be given by

$$dS = \frac{\partial S}{\partial I_0}\Delta I_0 + \frac{\partial S}{\partial \theta}\Delta\theta. \tag{5.33}$$

To detect a change due to the magnetic perturbation the condition

$$\left|\frac{\partial S}{\partial \theta}\Delta\theta\right| > \left|\frac{\partial S}{\partial I_0}\Delta I_0\right|, \tag{5.34}$$

hence

$$I_0 \cos 2\theta \Delta\theta > \frac{I_0}{2}(1 - \sin 2\theta), \tag{5.35}$$

must be met.

As the pitch angle θ is determined by the the orientation of the polarimeter and the magnetic fields with the plasma, it can be chosen to be 0 for simplicity. Using the relation Poissonian relation between the noise and intensity $\Delta I_0 = \sqrt{I_0} = \sqrt{\alpha N}$, where α is the camera gain and N is the number of detected photoelectrons per cell, Eq. 5.35 can be rearranged to give

$$\alpha N > \frac{1}{4(\Delta\theta)^2}. \tag{5.36}$$

This equation gives, for the ideal scenario, the number of photoelectrons needed to be detected to resolve the pitch angle perturbation. For the perturbation calculated and shown in Fig. 5.12, the change in pitch angle at maximum is $\Delta\theta = 1.5^o$. In order to determine the magnetic structure the system must be able to resolve perturbation of $\Delta \sim 1^o$, this results in the number of photoelectron counts per pixel to be $N \gtrsim 850/\alpha$.

Typical images captured at TEXTOR where with a Sensicam CCD camera, which had a gain $\alpha \approx 1$, had an image resolution of 688 x 520 with $N \approx 1000$ to 1500 per pixel for a 2 ms exposure.

As this method is dependent on capturing an image which is synchronised with the sawtooth cycle, the exposure time must be a fraction of the sawtooth cycle to obtain adequate resolution of the magnetic perturbation. The sawtooth period measured on TEXTOR with 100 % counter neutral beam injection is $\sim$ 40 ms [42] and the collapse times observed are 40-80 μs [41]. Thus with an exposure time of 2 ms it is possible to image stages of the sawtooth growth phase with sufficient photon flux to resolve the magnetic perturbation in the ideal case with the existing setup. However, if the crash phase is to be measured an intensified gated camera must be used, as the exposure time needed to resolve would require a gate time of $\sim$ 1-5 μs. For a camera with the same sensitivity and resolution as the Sensicam $\sim$ 500 sawtooth cycles must be imaged to gain the required signal to noise ratio, this is equivalent to $\sim$ 12 seconds of continuous "sawtoothing", but the longest plasma discharge produced lasts for 10 seconds and the typical for 5 seconds. However, as this resolution is high, the CCD camera can bin giving an image of 172 x 130 with 16 times the photoelectrons, reducing the number of cycles needed to a possible number.

5.4.2 Linking $\tilde{B}_Z$ to $\tilde{\psi}$

If such images of the perturbed vertical magnetic field component can be extracted from real data, it will be an enormous step forward. However, there are some considerations which must be accounted for, these will only be listed here and not discussed.

Firstly, the image which is captured is a slice of the magnetic perturbation in a direction defined by the neutral beam. Ideally the image of most use is a poloidal cross section of the perturbation allowing the perturbed magnetic field ($\tilde{B}_Z$) to be related to the perturbation of ψ. Thus a method to "straighten" these images must be developed.

The underlying perturbation of the flux function is the quantity which is of most use. As it is only the vertical component of the poloidal magnetic field which is measured, only half the information required to reconstruct $\tilde{\psi}$ is obtained. As the sawtooth instability is a 3D structure, a 2D analysis, as given here, is not adequate to relate $\tilde{B}_Z$ & $\tilde{B}_R$ to $\tilde{\psi}$.

Notwithstanding these, the vertical perturbed image can shed light on the region of the plasma which the instability is confined to. For example the kink instability is confined to the $q < 1$ region, through the perturbed image the $q = 1$ surface should be defined by the edge of the perturbation. Also the poloidal mode number of the perturbation can be extracted.

Chapter 6

Experimental Data

The experimental component of this thesis involved helping construct, implement, operate and analyze data from two MSE systems on the DIII-D tokamak in San Diego, USA. The purpose of this program was to undertake proof of principle experiments, in the sense that the instruments were deployed on the tokamak but the plasmas produced were designed for other experiments. The aim of the experiments was to confirm the feasibility of the system in order to have a basis from which to seek a dedicated run day to help lock down and sort out minor problems with the instrument.

6.1 DIII-D (USA)

The experimental program at DIII-D lasted 2 weeks during which time a number of experiments were undertaken using various imaging systems. Two days were allocated for the MSE instrument. The MSE instruments were based on a system that had been used at TEXTOR, with some success, 6 months earlier.

Double and switching spectro-polarimeter systems were designed and constructed at the ANU for operation on the DIII-D tokamak. The DIII-D tokamak is the largest operating tokamak in the USA with a major radius $R_{major} = 1.67$ m, a minor radius $a = 0.67$ m, toroidal magnetic field on axis $B_\phi = 2.2$ T and maximum toroidal plasma current $I_\phi = 6$ MA. Up to eight neutral heating beams can be used for heating the plasma and plasma control characterization, each delivering up to ~ 2.5 MW to the plasma [25]. The neutral heating which was used throughout the experiments was the left 30^o (30L) beam , shown in Fig. 6.1. This heating beam is also the primary diagnostic beam and as such the beam power is routinely modulated at 100 Hz for diagnostic purposes.

Due to the extensive diagnostics demands required by this tokamak, the optimum ports for viewing the neutral beam for MSE measurements were not available. The free ports allocated for the heterodyne trials were the 90^o and 120^o ports, both situated on the horizontal midplane and oriented such that they viewed the 30L neutral heating beam. Figure 6.1 shows the position of the these ports relative the neutral beam, also indicated is the approximate view of the neutral beam from these ports.

The double and switching polarimeters were constructed using a flexible mounting system, where each optical component is mounted in a holder and the system constructed by stacking the required elements on an optical rail. This type of assembly was chosen because: the two MSE systems as well as the other imaging systems used at DIII-D (not discussed here) have the major optical components in common, thus a wide variety of systems can be constructed at relatively low cost. A flexible system was needed as it could have been mounted on either the 90^o or 120^o port, where either view of the neutral beam requires a different optical setup for the optimum measurements. Figure 6.2 **(a)**

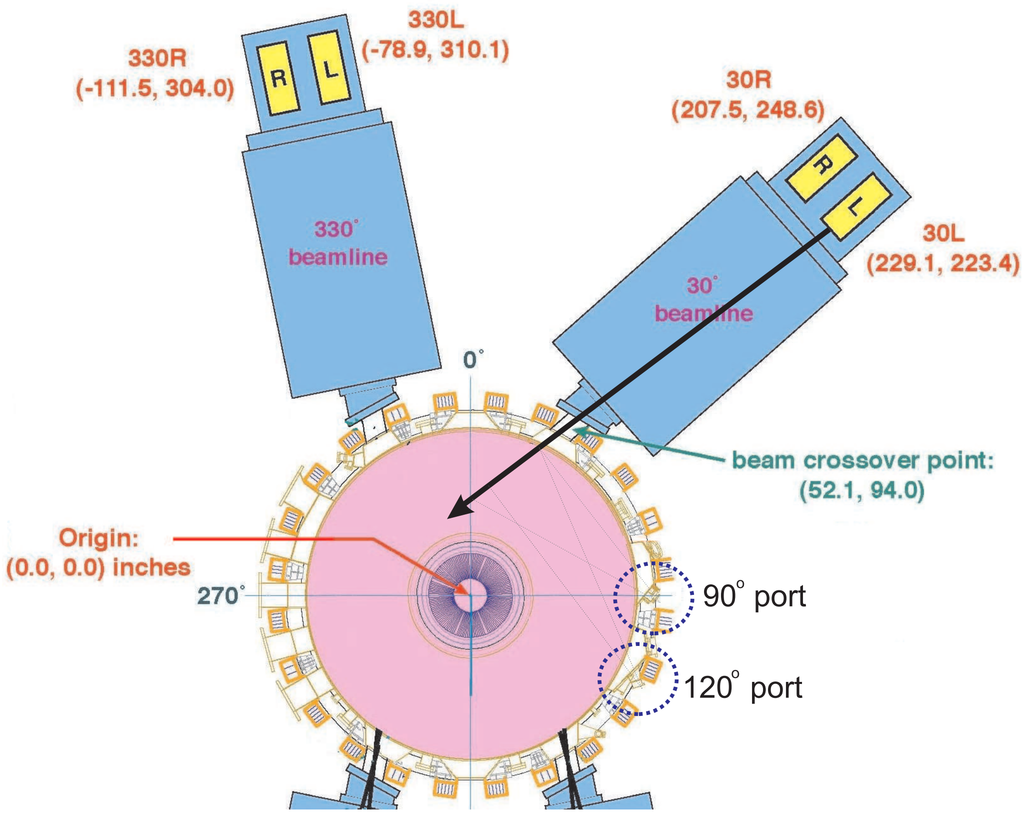

Figure 6.1: Geometry of the neutral heating beam injection system for DIID-D, showing only the 330^o and 30^o beamlines for clarity. The left 30^o neutral beam used for the MSE experiments is shown. The 90^o and 120^o ports used for the experiments have been highlighted with the approximate view of the neutral beam shown for both. The coordinates here are given in inches. (*Courtesy of the DIII-D program and General Atomics.*)

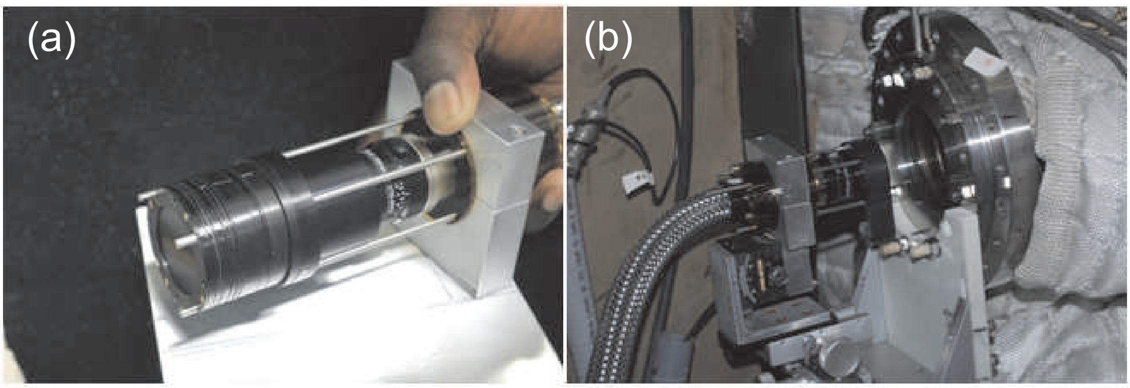

Figure 6.2: **(a)** A picture of the double spatial heterodyne spectro-polarimeter optical head. In this picture the individual optic components can be seen “stacked” on the optic rail. **(b)** The double heterodyne system mounted on the 90^o port of DIII-D. The coherent optical fibre bundle used to transmit the data can be seen leading off to the camera.

is a picture of the optical head for the double heterodyne spectro-polarimeter, where the individual optical elements and the rail which they are mounted on can be seen. Each optic element is circular with a diameter of 30 mm.

Due to the high neutron flux and limited space at the ports, the light from the instrument (the optical head) is focused onto a coherent fibre bundle which transmits the image to the CCD camera. The field of view of the instrument is defined by the primary lens between the optical head and the fibre bundle. The primary lens used for both the double and switchings system was a Schneider 35 mm focal length lens, which produced a field of view of $\sim 11^o$. In order to protect the CCD camera, which was a 12 bit Sensicam, it was placed approximately 2 m from the vacuum vessel of the tokamak inside a shielding box, which consisted of lead plate and neutron absorbing polyethelene beads.

As the view from these port looks upon the beam at $\sim 90^o$ to the direction of its velocity, negligible Doppler shift of the Stark split emission occurs, resulting in an observed MSE multiplet which has approximately the same central wavelength as the H_α/D_α source line, at 656.2 nm, and also the large neutral D background emission. As the inner surface of DIII-D consists of graphite shielding, bright carbon-II emission at 658 nm is produced which is a sufficiently close wavelength to leak through the wide band filter used to accept the Stark multiplet (see Fig. 3.38).

Since the MSE instruments developed are not affected by background unpolarized emission, this lack of separation does not render the instruments unusable at such ports. However, under some circumstances the instrument is susceptible to contamination from background polarized emission. The two major contaminants which may affect the image is background $H_\alpha \& D_\alpha$ as well as carbon-II emission at 658 nm. In general background $H_\alpha \& D_\alpha$ is generally unpolarized but polarization can occur from reflections from the internal surfaces of the tokamak.

6.1.1 Double heterodyne system

The view of the 30L neutral beam obtained at the 90^o port is such that the Doppler shift for the varying energy component Stark multiplets (full, half and third) do not completely separate across the field of view. Figure 6.3 **(a)** is a model spectrum[1] of these components for the beam versus the radius (R), showing that for the outer region of the plasma (large R) the Doppler shift is small resulting in the components to "bunch" and for the inner region the components separate due to the larger Doppler shift. The modelled nett contrast for this view versus optical delay is shown in **(b)**. Based on this modelling the optical delay of the primary wave-plate was chosen to be ~ 600 waves (shown by the line), such that a reasonable fringe contrast was achieved across the field of view.

The double heterodyne system was calibrated and mounted on the 90^o degree port of the tokamak. A picture of the optical head and mounting on the 90^o port is shown in Fig. 6.2 **(b)**, the coherent fibre bundle can be seen leading off to the camera.

As the instrument was constructed by individually mounting each optical element, it also proved difficult in the time available to align the elements perfectly. This resulted in the fringe pattern and contrast not to be ideal. Figure 6.4 **(a)** and **(b)** are two calibration shots illustrating the fringe pattern when the system is illuminated by a polarized source. It can be seen from these images that the fringe contrast is low when compared with previously obtained images with this system of the zinc calibration lamp (Fig. 2.8).

[1] These simulations were completed by my supervisor, Prof. John Howard

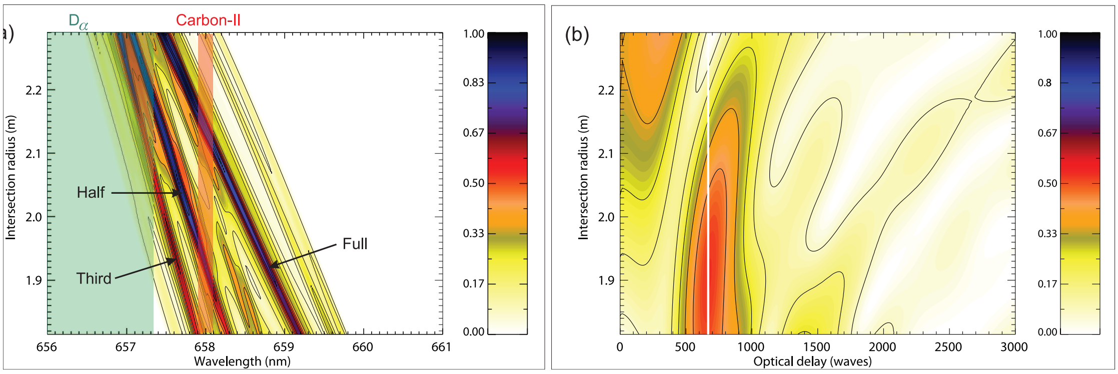

Figure 6.3: **(a)** Modelled spectrum of the complete Stark multiplets of the 30L neutral beam as viewed from the 90^o port as a function of radius. The full, half and third energy components have each been labeled as they coincide due to the perpendicular view of the beam. As a result they are unshifted from the background D_α emission, this thermal background emission is shown by the green transparent region. **(b)** the nett fringe contrast for this spectral scene versus optical delay of the primary wave plate for these spectrums. The white line indicates the optical delay of the primary wave-plate chosen.

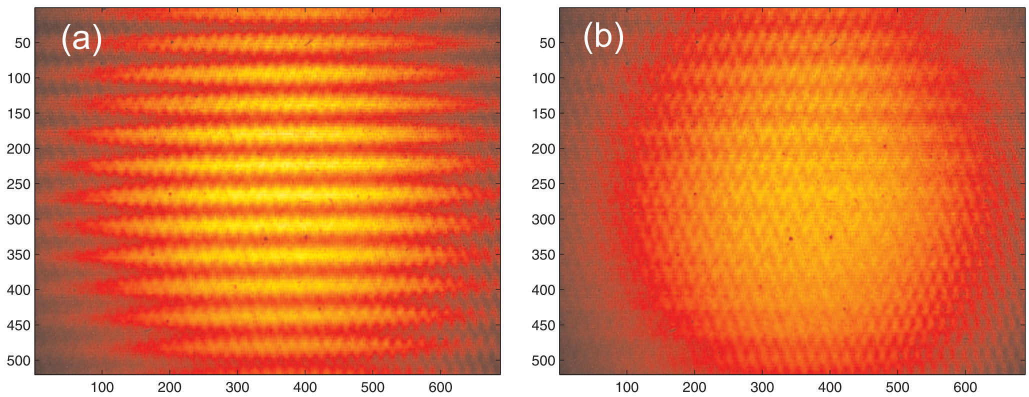

Figure 6.4: Raw calibration images for the double spatial heterodyne spectro-polarimeter illuminated by a polarized source, with **(a)** and **(b)** having two different polarization angles, illustrating the modulation of the fringe pattern and the poor fringe contrast. Figure **(c)** is an enlarged section of **(a)** illustrating the individual fibres of the coherent fibre bundle.

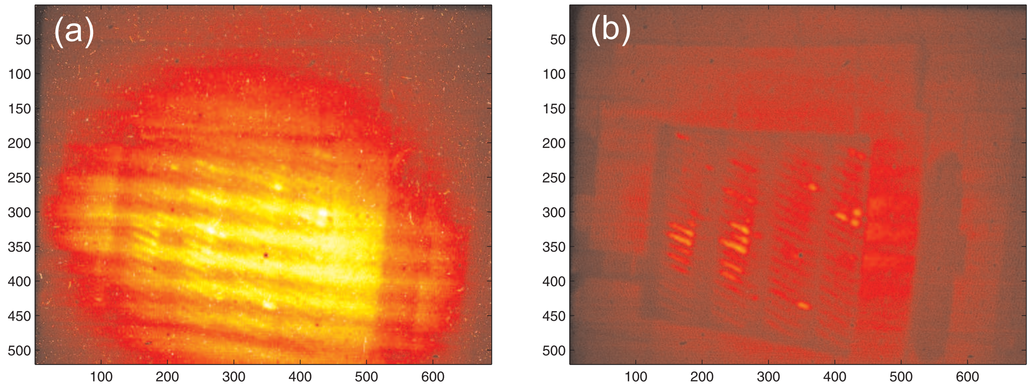

Figure 6.5: Raw images of shot 138353 captured with the double spatial heterodyne spectro-polarimeter illustrating the heating grill in the background of the view from the 90^o port on DIII-D.**(a)** is with the neutral heating beam on, note the saturated pixels are due to neutrons, and **(b)** with no neutral beam.

The view that was obtained by the instrument includes the image of a radio frequency (RF) heating antenna that was situated on the outer wall of the tokamak and in the middle of the image. Figure 6.5 **(a)** is a raw image of the neutral beam obtained by the instrument. The fringe pattern caused due to the polarized Stark emission can be seen as well as the RF heating antenna in the background. **(b)** is a raw image of the view when the neutral beam was off, which clearly reveals the RF heating antenna. This is the critical area in which the emission of the neutral beam is the highest intensity, thus the area of interest. The RF antenna has a configuration such that when it is illuminated with background radiation the coils of the antenna produce a pattern which is very similar to the fringe pattern produced by the instrument, for encoding the desired polarization information. The main reason for the heating antenna being visible is that it is lit up by the background bright carbon-II emission, the available view angle was such that the Doppler shift of the Stark multiplet was not sufficient to shift away from the 658 nm emission.

For these reasons, many unavoidable due to the non-ideal viewing angle, attempting to demodulate the images captured by the double heterodyne system, failed to extract satisfactorily the secondary fringe pattern which is needed to determine the polarization of the captured emission. Hence due to these unforeseen complications, the data gathered with this system was not useful.

6.1.2 Switching heterodyne system

For the second day of the MSE experiment it was decided to change systems to the switching spatial heterodyne spectro-polarimeter and to mount this system on the 120^o port. The decision to change the system was due to the fact that the switching system uses a simpler differential fringe pattern method, hence if the RF antenna is a constant in the background there should be a smaller contribution to the final image.

The modelled spectrum for the view of the 30L beam from the 120^o port is shown in Fig. 6.6 **(a)**. As this view is virtually perpendicular to the beam, very little separation of the energy components occur. As a result the nett contrast is increased due to the σ & π components of each Stark multiplet sitting on top of each other. The modelled nett contrast is shown in **(b)**. The same primary wave-plate (optical delay of $\sim$ 600 waves) was used with this system as the nett fringe contrast is a maximum across the field of vie at the same optical delay as the 90^o port.

As a result of this move the Stark multiplet was effectively unshifted from the background D_α emission. However, through discussions with other scientists present at DIII-D, it was advised that at the 120^o port the intensity of the D_α background emission was comparable with the beam induced Stark emission. Based on the results of modelling for this new configuration the wide band 658 nm filter which was used in the previous instrument was replaced with a narrower band H_α filter, in an attempt to minimize the leakage from background sources, such as carbon-II.

The images captured of the neutral beam with the switching system from the 120^o port were found to contain a large component of background partially polarized H_α. This partial polarization of the background light can be seen via the fringes observed with this system in areas of the captured image which do not contain the neutral beam emission (as the fringes only occur for this instrument when the light is polarized), an example of this is shown in the area of the white box in Fig. 6.7 **(a)**. The large unpolarized portion of the background emission can be seen in the line section shown in **(b)**. **(c)** is a calibration image of a polarized light source taken with the switching system, before it was mounted on the tokamak, and **(d)** is a line segment illustrating the excellent observed fringe visibility.

The partially polarized background light was confirmed to be H_α, as the fringes across the image were still observed when the filter in the system was replaced with a narrow band (1 nm) 655.5 nm filter for the last shots of the day. The maximum transmission was 40% at 655.5 nm, the transmission for background H_α at 656.2 nm was $\sim$ 10% and for carbon II at 658 nm was negligible.

The first stage of the data analysis is to assess the system through the calibration shots taken with the system. Before the system was mounted on the port, the system was illuminated by a polarized H_α source where a series of images were taken with known variations of the polarizer angle. Through fourier demodulation techniques, the phase of the fringe pattern can be extracted for successive frames, for the FLC switched on and off, which then allow the polarization angle of the incident light to be found through the

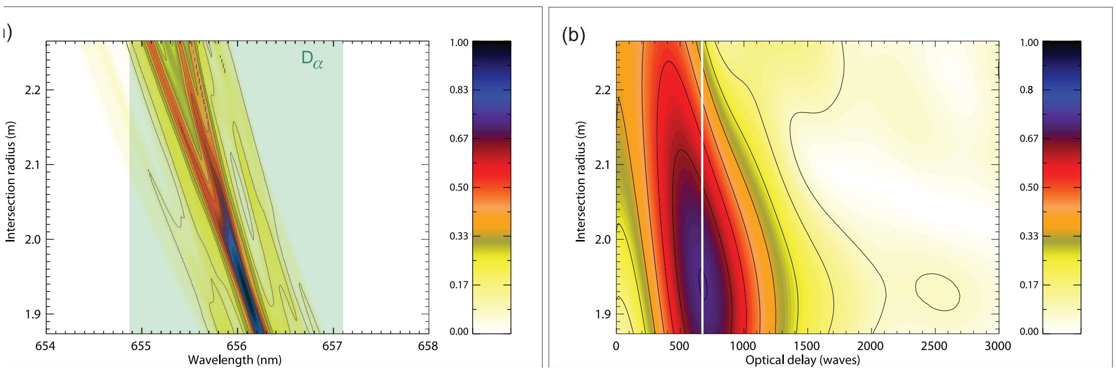

Figure 6.6: (a) Modelled spectrum of the complete Stark multiplets of the 30L neutral beam as viewed from the 120^o port as a function of radius. The full, half and third energy components have not been labeled as they coincide due to the perpendicular view of the beam. As a result they are unshifted from the background D_α emission, this thermal background emission is shown by the green transparent region. **(b)** the nett fringe contrast for this spectral scene versus optical delay of the primary wave plate for these spectrums. The white line indicates the optical delay of the primary wave-plate chosen.

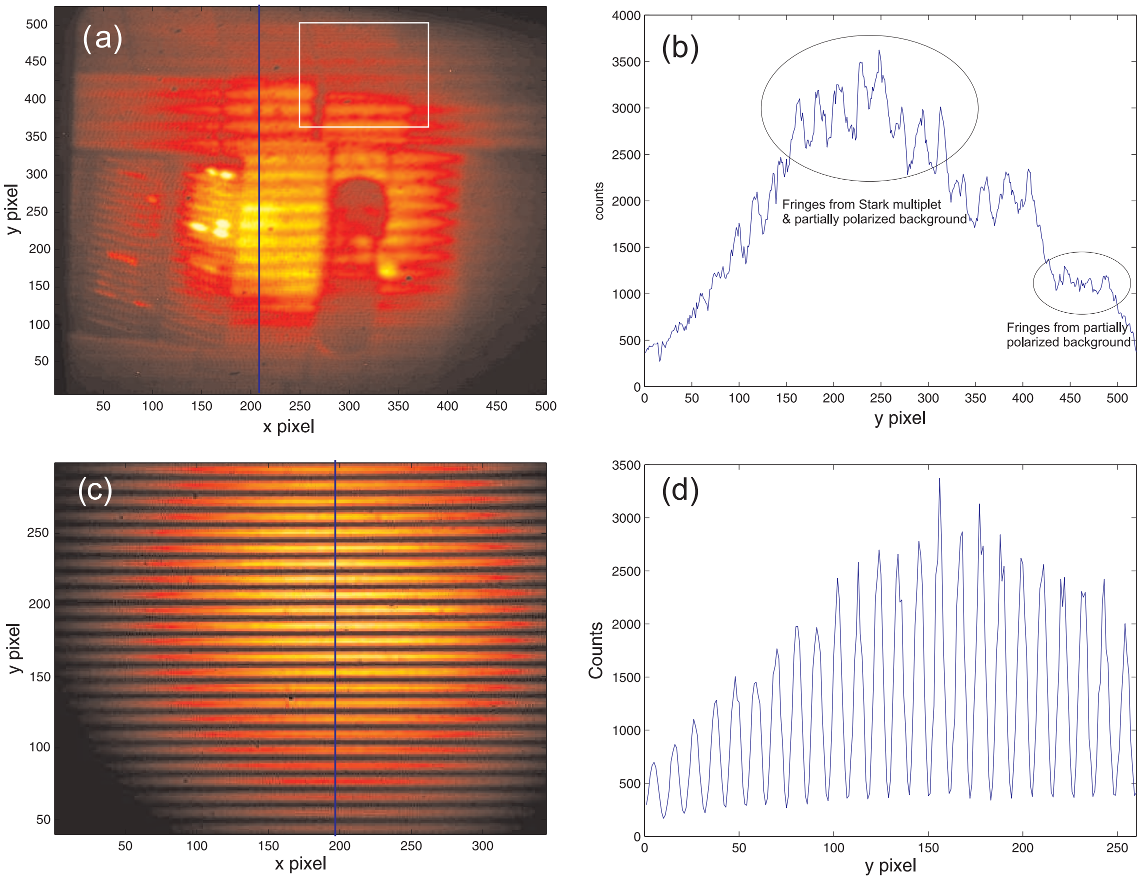

Figure 6.7: Raw images and line segment illustrating the difference in fringe visibility between the calibration images and plasma shots on DIII-D. **(a)** is a calibration image of a polarized source taken with the switching spatial heterodyne system before it was mounted on to the 120^o port on DIII-D. **(b)** is a plot of the line segment, shown by the vertical white line in **(a)**, which illustrates the fringe visibility. **(c)** is a raw image of shot 138385 captured with the switching spatial heterodyne spectro-polarimeter. The bright area of the image is due to the emission from the neutral heating beam. **d** is a line segment plot through the neutral heating beam which shows the poor fringe contrast, which is observed throughout the data captured with the switching system.

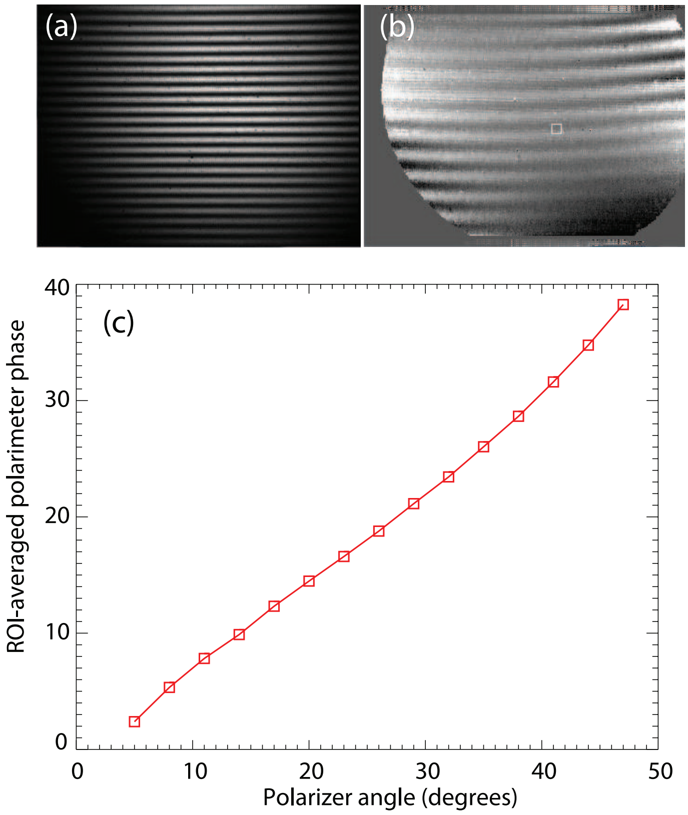

Figure 6.8: **(a)** is a raw calibration image of the switching heterodyne system illuminated with a polarized H_α source. **(b)** is an image of the demodulated phase difference between two successive frames which gives the measure of the polarization angle. **(c)** is a calibration curve for the system, by taking a region of interest (shown by the small box in **(b)**) and plotting the average measured polarization versus the true polarization angle of the source. The secondary fringe pattern observed in **(b)** is not expected, indicating a misalignment of optical components somewhere in the system.

difference between the frames. Figure 6.8 shows the raw image for one calibration frame in **(a)** and then the difference between the demodulated phase for successive frames in **(b)**. The sinusoidal pattern observed in **(b)** is not expected in an ideal system which suggests that there is a misalignment of optical components somewhere in the system, also a hyperbolic distortion pattern can be seen due to the non-ideal optical components. A calibration curve has been created for the system by taking a region of interest (ROI) of the phase images to find the average calculated polarization angle versus the angle of the polarizer used, this is shown in **(c)**. It can be seen that this curve is deviates slightly from a perfect linear fit. Meaning that due to the misalignment of the optical components, which introduces a systematic error to the calculated the polarization angle, the calculated polarization from the images must be corrected. This involves creating a "look-up-table" for every position of the image which gives the correction needed to adjust the calculated polarization angle to the true polarization angle.

Unfortunately, the data captured by the switching system has also not been useable, as the 30L neutral heating beam was modulated throughout the run day which was not synchronised with the FLC. The modulation of the beam occurred at 100 Hz for charge exchange recombination spectroscopy (CXRS) and the acquisition of the images occurred at $\sim$ 20 Hz. This meant that no two successive images of either the beam-off or beam-on were captured, which are needed if the effects of the partially polarized background emission is to be removed.

Chapter 7

Outcomes and Recommendations

The determination of the poloidal flux function ψ through numerical equilibrium reconstruction methods is vital for the understanding and control of the physics at play within a tokamak. Key internal magnetic measurements are currently provided by discrete channel 1D MSE polarimetry arrays. These measurements determine the accuracy of the solution of ψ and thus the understanding of the toroidal plasma current density, which largely determines the performance of the tokamak.

A successful 2D imaging MSE system has the unprecedented advantage that it captures all the information of the existing 1D systems and more, in an instrument which is compact and a fraction of the cost. It also has the ascendancy that it measures the polarization of the entire Stark multiplet simultaneously using a spatially varying filter, rather than measuring the polarization of a single spectrally isolated components by expensive tunable narrow band filters. As a result the 2D imaging measurement is not sensitive to fluctuations in the neutral beam energy, which can degrade the quality of the measurement of conventional systems through small fluctuations in the Doppler shift of the Stark multiplet.

The analysis of the 2D MSE imaging instrument presented in this thesis has revealed that for neutral beams injected toroidally along the horizontal midplane, the optimum viewing geometry for an instrument situated in the horizontal midplane is one which looks "along" the neutral beam. Such a viewing geometry can be achieved by looking in the direction of the velocity of the neutral beam from the "inboard" side or by looking in the opposite to the beams velocity from the "outboard" side. Such geometries are equivalent to the standard view adopted by existing MSE systems.

The additional information captured by the 2D system is the spatial variation of the vertical magnetic field component (B_Z) and the velocity profile of the neutral beam. If a more accurate solution of the poloidal flux function ψ is to be obtained through this new 2D capability, the velocity profile of the neutral heating beam must be measured, unlike conventional 1D systems where the typical viewing geometry reasonably allows the assumption that the velocity of the beam is well known.

However, it is clear that a number of advantages accrue in adopting a 2D system over a 1D system. An exciting capability which the 2D system provides is imaging of the magnetic structure associated with MHD instabilities.

By exploring the properties of the pitch angle equation it has been found that the optimal viewing position has an approximate form which allows an image of a vertical magnetic field perturbation ($\tilde{B}_Z$) to be extracted. The method for determining the perturbed vertical magnetic field component ($\tilde{B}_Z$) associated with MHD plasma instabilities based on synchronous polarization imaging of the Stark multiplet has been developed in this thesis. The first order approximations to the pitch angle equation, which is required for the extraction, have been validated by developing an analytic model accompanied by an accurate numerical implementation of the 2D MSE measurement. Within this model a method to determine the poloidal magnetic field strengths, which automatically satisfy the MHD equilibrium condition, has been developed using a prescribed parameterized poloidal magnetic flux in a general curvilinear flux surface coordinate system. This model has not only provided a means to validate the approximate form of the pitch angle equation but also gives an accurate generalized model which can be used in future forward modelling of the MSE system on any tokamak.

A result of the development of the analytical model in this thesis has also been the discovery of incorrect material relating to the Miller equilibrium flux surface model given in numerous papers published by W. Stacey.

The technical feasibility of capturing the required images needed for the extraction of the perturbed magnetic field is high. Gated intensified high speed cameras, now available, provide the necessary hardware to capture synchronised images of MHD activity within tokamaks. Also, as the perturbed magnetic field is extracted by a differences procedure, many of the systematic errors native to the imaging system are removed. More importantly this method does not require the velocity profile of the neutral beam to be known.

Limited results have been obtained from the experimental data gathered at the DIII-D tokamak. This is due to unforeseen and unavoidable complications with the views obtained from the ports available, as described in chapter 6.

The following recommendations for future work associated with that presented here are:

- For the work to be undertaken at TEXTOR in 2010; time permitting there should be a study of the neutral beam profile as well as a first attempt to synchronously image MHD activity.

- As the instabilities within a tokamak are 3D in nature, the next step in the forward modelling of these magnetic perturbations and their effect on the pitch angle images should be undertaken using a 3D model of the MHD perturbation, rather than a first approximation with the 2D equilibrium model as done in this thesis. Complete numerical models for the sawtooth instability exist. Incorporating the calculated poloidal magnetic field strengths from these models into the determination of the pitch angle images will provide a more accurate "prior model" against which the experimental data can be compared.

- A product of this work is the challenge to determine a method to relate the observed perturbed vertical magnetic field to the underlying toroidal plasma current density. This determination is difficult in nature as only the vertical component of the poloidal magnetic field is resolved.

- If the extraction of an image of a perturbed magnetic field proves to be successful, numerous opportunities for the applications of the 2D imaging system arise. Simultaneously measuring different neutral heating beams can allow further studies into the spatial nature of the sawtooth collapse (does it occur simultaneously or is it triggered in one position and then propagate?). Alternatively if multiple viewing positions of one neutral beam can be adopted, it may be possible to tomographically construct a 3D image of the magnetic structure associated with MHD instabilities.

Appendices

Appendix A: Relationship between the poloidal flux function ψ and the vector potential A in the Miller representation

For axisymmetric equilibrium, that is equilibria which is independent of the toroidal angle ϕ, there are nested magnetic surfaces [2]. The poloidal magnetic flux ψ is the poloidal flux lying within each magnetic surface, hence it is constant on a surface. Thus ψ satisfies

$$\nabla\psi \cdot \mathbf{B} = 0. \tag{8.1}$$

Within the Miller representation the gradient of the flux function is

$$\nabla\psi = \partial_r\psi\mathbf{e}^r + \partial_\theta\psi\mathbf{e}^\theta + \partial_\phi\psi\mathbf{e}^\phi. \tag{8.2}$$

Defining the magnetic field as $\mathbf{B} = B^r\mathbf{e}_r + B^\theta\mathbf{e}_\theta + B^\phi\mathbf{e}_\phi$, Eq. 8.1 becomes

$$\nabla\psi \cdot \mathbf{B} = \partial_r\psi B^r + \partial_\theta\psi B^\theta + \partial_\phi\psi B^\phi. \tag{8.3}$$

As it is an axially-symmetric equilibrium considered $\partial_\phi = 0$. Since the magnetic field must be divergence free ($\nabla \cdot \mathbf{B} = 0$) it can be written in terms of a vector potential ($\mathbf{B} = \nabla \times \mathbf{A}$). The curl of the vector potential $\mathbf{A}$ in Miller coordinates is given by

$$\nabla \times \mathbf{A} = \frac{1}{\sqrt{G}}[(\partial_\theta A_\phi - \partial_\phi A_\theta)\mathbf{e}_r + (\partial_\phi A_r - \partial_r A_\phi)\mathbf{e}_\theta + (\partial_r A_\theta - \partial_\theta A_r)\mathbf{e}_\phi], \tag{8.4}$$

where $G = det(g_{ij})$. The components of the magnetic field in the axially-symmetric case are

$$B^r = \frac{\partial_\theta A_\phi}{\sqrt{G}}, \tag{8.5}$$

$$B^\theta = -\frac{\partial_r A_\phi}{\sqrt{G}}, \tag{8.6}$$

$$B^\phi = \frac{\partial_r A_\theta - \partial_\theta A_r}{\sqrt{G}}. \tag{8.7}$$

Expanding the Eq. 8.1 for the flux function and using the relation $\mathbf{e}_i \cdot \mathbf{e}^j = \delta_i^j$, it is found

$$\nabla\psi \cdot \mathbf{B} = \partial_r\psi B^r + \partial_\theta\psi B^\theta = 0, \tag{8.8}$$

substituting the forms of B^r and B^θ from Eq. 8.5 and 8.6, it is found

$$\partial_r\psi\frac{\partial_\theta A_\phi}{\sqrt{G}} - \partial_\theta\psi\frac{\partial_r A_\phi}{\sqrt{G}} = 0, \tag{8.9}$$

which is satisfied when

$$\psi = A_\phi \tag{8.10}$$

Appendix B: Determining B_R and B_Z from Miller magnetic field components B^r and B^θ

Using the identification that the poloidal flux function ψ is equivalent to the toroidal vector potential A_ϕ, the radial B^r and poloidal B^θ magnetic components of the Miller representation can be found by taking the appropriate derivatives of ψ.

In order to calculate the MSE pitch angle map, B^r and B^θ must be resolved into the cylindrical basis components B^R and B^Z [1]. In general B^r is zero as ψ is poloidally symmetric, the most general form of B^R, B^Z will be derived here for when perturbations to the magnetic field are considered.

The Miller basis vectors $\mathbf{e}_r, \mathbf{e}_\theta$ used to describe B^r, B^θ can be resolved into the cylindrical basis vectors $\hat{\mathbf{e}}_R, \hat{\mathbf{e}}_Z$ using the Jacobian which describes the transformation (this is an alternate representation of the definition of the tangent-basis vectors).

Through the definition of the Jacobian, the Miller unit basis vectors can be written in terms of the cylindrical unit basis vectors

$$\begin{pmatrix} \mathbf{e}_r \\ \mathbf{e}_\theta \\ \mathbf{e}_\phi \end{pmatrix} = J\left[\frac{R, Z, \phi}{r, \theta, \phi}\right] \begin{pmatrix} \mathbf{e}_R \\ \mathbf{e}_Z \\ \mathbf{e}_\phi \end{pmatrix}, \tag{8.11}$$

where

$$J\left[\frac{R, Z, \phi}{r, \theta, \phi}\right] = \begin{pmatrix} \partial_r R & \partial_r Z & 0 \\ \partial_\theta R & \partial_\theta Z & 0 \\ 0 & 0 & \partial_\phi \phi \end{pmatrix}, \tag{8.12}$$

and R, Z, ϕ are the transformation equations between Miller and cylindrical coordinates.

Thus the radial and poloidal basis vectors can be written as

$$\begin{aligned} \mathbf{e}_r &= \partial_r R\ \mathbf{e}_R + \partial_r Z\ \mathbf{e}_Z, & (8.13) \\ \mathbf{e}_\theta &= \partial_\theta R\ \mathbf{e}_R + \partial_\theta Z\ \mathbf{e}_Z. & (8.14) \end{aligned}$$

Substituting these basis vectors into the general representation for the magnetic field in Miller coordinates, $\mathbf{B} = B^r\mathbf{e}_r + B^\theta\mathbf{e}_\theta + B^\phi\mathbf{e}_\phi$, and taking the dot product with the unit vectors for R and Z the components are

$$\begin{aligned} B_R &= \mathbf{B}\cdot\hat{\mathbf{e}}_R = \partial_r R B^r + \partial_\theta R B^\theta, & (8.15) \\ B_Z &= \mathbf{B}\cdot\hat{\mathbf{e}}_Z = \partial_r Z B^r + \partial_\theta Z B^\theta, & (8.16) \end{aligned}$$

[1] As the cylindrical basis is an orthogonal curvilinear coordinate system $B^R \equiv B_R$ and $B^Z \equiv B_Z$

Appendix C: Form of ψ for large aspect ratio plasma with parabolic current density

The current lines for a plasma in equilibrium lie in the magnetic surfaces, resulting in the current density being a flux surface quantity. The basic form for the toroidal plasma current can be well approximated by a parameterized parabolic form with its maximum occurring at the centre of the plasma. In the Miller flux surface equilibrium model the toroidal component of the current density, may be written in the general parameterised form

$$j_\phi = j_0 \left(1 - \left(\frac{r}{a}\right)^\alpha\right)^\beta, \tag{8.17}$$

where j_0 is determined by the magnitude of the total toroidal current, measured by external magnetic measurements. The parameter β is set to one ($\beta = 1$) for ease of calculations and as α is the dominant parameter which controls the general shape of the current profile.

For large aspect ratios R_0/a the toroidal bending of the current distribution can be ignored, hence the poloidal magnetic field is only a function of r. Applying Ampère's law for the poloidal magnetic field

$$\oint \mathbf{B} \cdot d\mathbf{l}(\theta) = \mu_0 \int_S \mathbf{j} \cdot \mathbf{e}_\phi \; da, \tag{8.18}$$

in the case for concentric circular flux surfaces, that is ignoring Shafranov shift and taking $\kappa = 1$ and $\delta = 0$. The area element $da = \sqrt{g_{rr} g_{\theta\theta} - g_{r\theta}^2} \; dr \; d\theta = r \; dr \; d\theta$ hence Eq. 8.18 becomes

$$\int_0^{2\pi} B_\theta(r) \; r d\theta = \mu_0 j_0 \int_0^{2\pi} \int_0^r \left(r' - \frac{r'^{\alpha+1}}{a^\alpha}\right) \; dr' d\theta, \tag{8.19}$$

$$2\pi r B_\theta(r) = 2\pi \mu_0 j_0 \left(\frac{r^2}{2} - \frac{r^{\alpha+2}}{(\alpha+2)a^\alpha}\right). \tag{8.20}$$

The poloidal magnetic flux is defined as [34]

$$\psi \equiv \int_{S_{pol}} \mathbf{B} \cdot d\mathbf{S}, \tag{8.21}$$

which in the Miller representation becomes

$$\psi = \int_0^{2\pi} \int_0^r B_\theta R \; dr d\phi. \tag{8.22}$$

In the large aspect ratio approximation, the dependence in the radius R on r can be neglected. Substituting the form of B_θ from Eq. 8.20 and integrating it is found that

$$\psi = 2\pi R \mu_0 j_0 \left(\frac{r^2}{4} - \frac{r^{\alpha+2}}{(\alpha+2)^2 a^\alpha}\right). \tag{8.23}$$

It is chosen to parameterise the poloidal function as

$$\psi = c \left(\frac{r^2}{4} - \frac{r^{\alpha+2}}{(\alpha+2)^2 a^\alpha}\right), \tag{8.24}$$

where α will vary around 2.

Appendix D: Toroidal current density

The toroidal current density can be estimated from the determined poloidal magnetic fields using $\mu_0 \mathbf{j} = \nabla \times \mathbf{B}$. The curl of the magnetic field in the Miller representation is

$$\nabla \times \mathbf{B} = \frac{1}{\sqrt{G}} \left[\left(\frac{\partial B_\theta}{\partial r} - \frac{\partial B_r}{\partial \theta} \right) \mathbf{e}_\phi + \left(\frac{\partial B_r}{\partial \phi} - \frac{\partial B_\phi}{\partial r} \right) \mathbf{e}_\theta + \left(\frac{\partial B_\phi}{\partial \theta} - \frac{\partial B_\theta}{\partial \phi} \right) \mathbf{e}_r \right], \qquad (8.25)$$

The toroidal plasma current is thus given by

$$\mathbf{j} \cdot \mathbf{e}^\phi = \frac{1}{\mu_0 \sqrt{G}} \left(\frac{\partial B_\theta}{\partial r} - \frac{\partial B_r}{\partial \theta} \right). \qquad (8.26)$$

In order to calculate the toroidal current, the covariant components of the magnetic field must be used. The contravariant components which are calculated from ψ can be converted to covariant component using $B_i = g_{ij} B^j$. The covariant components are thus

$$B_r = g_{rr} B^r + g_{r\theta} B^\theta, \qquad (8.27)$$

$$B_\theta = g_{\theta r} B^r + g_{\theta\theta} B^\theta. \qquad (8.28)$$

It is the physical quantity that is of interest, which is given by $j^\phi = \mathbf{j} \cdot \hat{\mathbf{e}}^\phi = \sqrt{g_{\phi\phi}} \mathbf{j} \cdot \mathbf{e}^\phi$. Hence substituting the covariant components into Eq. 8.26 the toroidal current is given by

$$j^\phi = \frac{\sqrt{g_{\phi\phi}}}{\mu_0 \sqrt{G}} \left[\frac{\partial}{\partial r} \left(g_{\theta r} B^r + g_{\theta\theta} B^\theta \right) - \frac{\partial}{\partial \theta} \left(g_{rr} B^r + g_{r\theta} B^\theta \right) \right]. \qquad (8.29)$$

Bibliography

[1] J. Howard, "Snapshot-imaging motional stark effect polarimetry," *Plasma Physics and Controlled Fusion*, vol. 50, no. 125003, 2008.

[2] J. Wesson, *Tokamaks*. Clarendon Press, 3rd ed., 2004.

[3] R. White, *The Theory of Toroidally Confined Plasmas*. London: Imperial College Press, 2nd ed., 2001.

[4] F. Levinton, M. Zarnstorff, S. Batha, M. Bell, R. Bell, R. Budny, C. Bush, Z. Chang, E. Fredrickson, A. Janos, J. Manickam, A. Ramsey, S. Sabbagh, G. Schmidt, E. Synakowski, and G. Taylor, "Improved Confinement With Reversed Magnetic Shear in Tftr," *Physical Review Letters*, vol. 75, no. 24, pp. 4417–4420, 1995.

[5] R. Dendy, *Plasma Physics*. Cambridge University Press, 1996.

[6] J. Blum, C. Boulbe, and B. Faugeras, "Real-time equilibrium reconstruction in a Tokamak," in *Burning Plasma Diagnostics* (Orsitto, FP and Gorini, G and Sindoni, E and Tardocchi, M, ed.), vol. 988 of *AIP Conference Proceedings*, pp. 420–429, 2008.

[7] V. Pustovitov, "Magnetic diagnostics: General principles and the problem of reconstruction of plasma current and pressure profiles in toroidal systems," *Nuclear Fusion*, vol. 41, no. 6, 2001.

[8] R. Hastie, "Sawtooth instability in tokamak plasmas," *Astrophysics and Space Science*, vol. 256, no. 1-2, pp. 177–204, 1998.

[9] J. Wesson, "Sawtooth oscillations," *Plasma Physics and Controlled Fusion*, vol. 28, no. 1A, pp. 243–248, 1986.

[10] F. Porcelli, D. Boucher, and M. Rosenbluth, "Model for the sawtooth period and amplitude," *PLASMA PHYSICS AND CONTROLLED FUSION*, vol. 38, no. 12, pp. 2163–2186, 1996.

[11] S. Mirnov, I. Semenov, A. Belov, and E. Azizov, "The positive magnetic island concept and its application to T-11M experiments," *Nuclear Fusion*, vol. 40, pp. 727–730, 2000.

[12] F. Levinton, "The motional stark effect: Overview and future development," *Review of Scientific Instruments*, vol. 70, no. 1, pp. 810–814, 1999.

[13] E. S. H. Bethe, *Quantum Mechanics of One- and Two-Electron Atoms*. Springer, 1957.

[14] F. L. et al., "Magnetic field pitch-angle measurements in the pbx-m tokamak using motional stark effect," *Physical Review Letters*, vol. 63, no. 19, 1989.

[15] F. Levinton, “Magnetic field pitch angle diagnostic using motional stark effect (invited),” *Review of Scientific Instruments*, vol. 61, no. 10, 1990.

[16] D. Wroblewski and L. Lao, “Polarimetry of motional starl effect and determination of current profiles in diii-d (invited),” *Review of Scientific Instruments*, vol. 63, no. 10, 1992.

[17] B. Rice, “Motional stark effect upgrades on diii-d,” *Review of Scientific Instruments*, vol. 66, no. 1, 1994.

[18] C. Holcomb, “Overview of equilibrium reconstruction on diii-d using new measurments from an expanded motional stark effect diagnostic,” *Review of Scientific Instruments*, vol. 79, 2008.

[19] E. Foley and F. Levinton, “Devolopment of the motional stark effect with laser-induced fluoressence diagnostic,” *Review of Scientific Instruments*, vol. 75, no. 10, 2004.

[20] N. A. Pablant, K. H. Burrell, R. J. Groebner, D. H. Kaplan, and C. T. Holcomb, “Measurements of the internal magnetic field on DIII-D using intensity and spacing of the motional Stark multiplet,” *Review of Scientific Instruments*, vol. 79, no. 10, 2008.

[21] W. Steel, *Interferometry*. London: Cambridge University Press, 1967.

[22] M. Francon and S. Mallick, *Polarization Interferometry*. London: Wiley-Interscience, 1971.

[23] E. Hect, *Optics*. Reading, Massachusetts: Addison-Wesley Publishing Company, 2nd ed., 1987.

[24] R. Uhlemann and J. Ongena, “Variation of injected neutral beam power at constant particle energy by changing the beam target aperture of the textor neutral beam injectors,” *Fusion Technology*, vol. 35, no. 1, pp. 42–53, 1999.

[25] H. Chiu, “Measurement of neutral beam profiles at diii-d.” General Atomics Project 3466, 1998.

[26] B. Rice, “Effect of plasma radial electric field on motional stark effect measurements and equilibrium reconstruction,” *Nuclear Fusion*, vol. 37, no. 4, pp. 517–521, 1997.

[27] M. Murakami, J. M. Park, C. C. Petty, T. C. Luce, W. W. Heidbrink, T. H. Osborne, R. Prater, M. R. Wade, P. M. Anderson, M. E. Austin, N. H. Brooks, R. V. Budny, C. D. Challis, J. C. DeBoo, J. S. deGrassie, J. R. Ferron, P. Gohil, J. Hobirk, C. T. Holcomb, E. M. Hollmann, R. M. Hong, A. W. Hyatt, J. Lohr, M. J. Lanctot, M. A. Makowski, D. C. McCune, P. A. Politzer, J. T. Scoville, H. E. St John, T. Suzuki, T. S. Taylor, W. P. West, E. A. Unterberg, M. A. Van Zeeland, and J. H. Yu, “Off-axis neutral beam current drive for advanced scenario development in DIII-D,” *Nuclear Fusion*, vol. 49, no. 6, 2009.

[28] R. Miller, “Noncircular, finite aspect ratio, local equilibrium model,” *Physics of Plasmas*, vol. 5, no. 4, 1998.

[29] R. Waltz and R. Miller, “Ion temperature gradient turbulence simulations and plasma flux surface shape,” *Physics of Plasmas*, vol. 6, no. 11, pp. 4265–4271, 1999.

[30] E. A. Belli, G. W. Hammett, and W. Dorland, “Effects of plasma shaping on nonlinear gyrokinetic turbulence,” *Physics of Plasmas*, vol. 15, no. 9, 2008.

[31] W. M. Stacey, “Rotation velocities in the plasma edge driven viscously by scrape-off layer flows,” *Physics of Plasmas*, vol. 16, no. 6, 2009.

[32] W. M. Stacey, “Representation of the plasma eluid equations in ”Miller equilibrium” analytical flux surface geometry,” *Physics of Plasmas*, vol. 16, no. 8, 2009.

[33] A. Borisenko and I. Tarapov, *Vector and Tensor Analysis, with Applications*. New York: Dover Publications, Inc., 1979.

[34] W. D’haeseleer, W. Hitchon, J. Callen, and J. Shohet, *Flux Coordinates and Magnetic Field Structure*. Berlin: Springer-Verlag, 1991.

[35] I. Sokolnikoff, *Tensor Analysis*. New York: John Wiley & Sons, Inc., 1951.

[36] W. M. Stacey, “Applications of the Miller equilibrium to extend tokamak computational models,” *Physics of Plasmas*, vol. 15, no. 12, 2008.

[37] W. M. Stacey, “Effect on the divertor and scrape-off layer plasma properties of the distribution of power and particle influxes from the core,” *Physics of Plasmas*, vol. 16, no. 3, 2009.

[38] K. Miyamoto, *Plasma physics for nuclear fusion*. MIT Press, 1989.

[39] L. Lao, S. Hirshman, and R. Wieland, “Variational moment solutions to the grad-shafranov equation,” *Physics of Fluids*, vol. 24, no. 8, pp. 1431–1441, 1981.

[40] J. Howard, “Spatial heterodyne spectro-polarimetry systems for imaging key plasma parameters in fusion devices,” *Proceedings of ITC18*, 2008.

[41] V. Udintsev, M. Ottaviani, P. Maget, G. Giruzzi, J. Segui, T. Aniel, J. Artaud, F. Clairet, M. Goniche, G. Hoang, G. Huysmans, F. Imbeaux, E. Joffrin, D. Mazon, A. Pecquet, R. Sabot, A. Sirinelli, L. Vermare, T. Team, A. Kramer-Flecken, H. Koslowski, A. Donne, F. Schuller, C. Domier, N. Luhmann, S. Mirnov, and Textor Team, “Experimental observation of m/n=1/1 mode behaviour during sawtooth activity and its manifestations in tokamak plasmas,” *Plasma Physics and Controlled Fusion*, vol. 47, no. 8, pp. 1111–1136, 2005.

[42] I. T. Chapman, S. D. Pinches, H. R. Koslowski, Y. Liang, A. Kraemer-Flecken, M. de Bock, and TEXTOR Team, “Sawtooth stability in neutral beam heated plasmas in TEXTOR,” *Nuclear Fusion*, vol. 48, no. 3, 2008.